



UNIVERSITÀ DEGLI STUDI
DI TRENTO

DEPARTMENT OF INFORMATION ENGINEERING AND COMPUTER SCIENCE
ICT International Doctoral School

ADVANCED METHODS FOR CHANGE DETECTION IN LIDAR DATA AND HYPERSPETRAL IMAGES

Daniele Marinelli

Advisor

Prof. Lorenzo Bruzzone
University of Trento

Co-Advisors

Dr. Claudia Paris
University of Trento

Dr. Francesca Bovolo
Fondazione Bruno Kessler

September 2019

Ai miei genitori

Abstract

In the last years Remote Sensing technology has significantly improved and new sensors capable of acquiring data with high spatial and spectral resolution have been developed. Light Detection And Ranging (LiDAR) and Hyperspectral (HS) sensors acquire data that accurately characterize the 3-D structure and the spectral signature of the area of interest, respectively. With the upcoming generation of small sensors designed for Unmanned Aerial Vehicle (UAVs) and new spaceborne missions such data will be acquired more and more often increasing the availability of multitemporal datasets. This requires the development of methods capable of considering the time variable in the analysis of LiDAR point clouds and HS images. In this context, this thesis provides three main contributions related to: i) Change Detection (CD) in LiDAR data, ii) multiple CD in HS images and iii) fusion of bitemporal LiDAR point clouds.

The first novel contribution presents a method for the detection of 3-D changes at the individual tree level in conifer forests using bitemporal LiDAR data. Unlike most of the literature techniques, the method performs an object-based CD to estimate both the vertical and horizontal growth of the individual tree-crown working directly in the point cloud domain to fully exploit the information content of the LiDAR data. Multiple CD in HS images is addressed in the second contribution. Differently from most of the existing methods in the literature, we focus on the information content of each spectral channel to define a novel efficient representation of the change information. This representation is used to automatically discriminate between the different kinds of change. The third contribution presents two methods for the fusion of bitemporal LiDAR point clouds aimed at improving the modeling of the individual tree-crown. One is a compound approach used to improve the detection of tree-tops of conifers by reducing false detections and recovering missed detections. It exploits the temporal correlation between the two LiDAR point clouds by modeling the different probabilities of transition from one date to the other and using the Bayes rule for minimum error to perform the decision process. The other fusion method exploits the richer information content of high density point clouds to improve the parameters estimation of individual conifers in low density data. For each tree, it uses a 3-D model to reconstruct the shape of the crown using the parameters estimated on the high density data to drive the estimation on the low density point cloud.

The proposed methods have been tested on LiDAR point clouds and on simulated and real bitemporal HS datasets. Quantitative and qualitative experimental results confirm the effectiveness of the proposed automatic and unsupervised techniques, which show equal or better results compared to existing unsupervised and supervised techniques.

Acknowledgements

Now that I'm nearing the end, I can look back and take a look at this bumpy journey that has changed me more than I can grasp. All the invaluable research and life experiences and much more were made possible by the people that accompanied me during these years and for this, I would like to thank them.

Thank you Lorenzo for being an exceptional advisor guiding and motivating me throughout all these years. Your lessons and advices have been of great importance to me not only for my research but also for my personal growth. I owe a lot of this journey to you. I would like to thank my two co-advisors Claudia and Francesca. Claudia, you have guided me in the forest of the point cloud since my master thesis and you were always available to talk and support me. Beside this, you have been also a friend with whom I shared some great Texas and west US moments. Thank you Francesca for your invaluable guidance in the multi dimensional world of Hyperspectral data and for your kind words that were always a source of motivation to overcome the obstacles I encountered.

Moving to Vancouver, I would like to thank professor Nicholas C Coops and its team for my research period at the Forestry department of the University of British Columbia. You showed me a different perspective to Remote Sensing and taught me that my name can be pronounced in many different ways. I would like to thank Ignacio and Giona for guiding me through the nature of British Columbia. I'm really glad to have found you two in the Canadian mountains.

Coming back to Italy, I would like to thank the RSLab and University of Trento fellows. Thank you Andrea and Leonardo for the countless lunches, the nonsense talks and for keeping my morale high. Thank you Massimo for being always an happy spirit, the precious technical suggestions and the long discussions about Hyperspectral cameras and drones.

I would like to thank Mirko, Nicola, Fabio, Matteo and Paolo. We met almost 10 years ago, gone through quite a bit of stuff together, some of us are even married and even though we do not see each other as much as in the past, you are and will always be an important part of my life. Luca, even though we met at the beginning of the PhD, we had to randomly meet in Canada to really know each other, and I'm happy we could share that experience together. Thank you for the adventures in the British Columbia wilderness and for your precious friendship.

Alessandra, you came into my life just before I started writing this thesis and you made everything easier. Thank you for having been always by my side, cheering me up whenever I needed it and for standing my numerous grumpy moments. I feel so lucky I have met you and I hope we will build lots of beautiful memories together.

Infine, un enorme grazie va a tutti i membri della mia famiglia. In particolare, ringrazio i miei genitori. È difficile per me esprimere a parole l'affetto e la gratitudine che provo nei vostri confronti ma faccio un tentativo. Grazie per il vostro affetto incondizionato, per essere stati sempre al mio fianco, per i preziosi insegnamenti e per avermi sempre supportato e sopportato. Devo molto di ciò che sono oggi a voi.

Daniele

Contents

List of Tables	iii
List of Figures	v
List of Abbreviations	vii
List of Symbols	ix
Introduction	1
1 Fundamentals and Background: Change Detection in Multitemporal LiDAR Point Clouds	9
1.1 Airborne LiDAR Sensors	9
1.2 Change Detection in LiDAR Data for Forestry	13
1.2.1 Previous Works on Change Detection in LiDAR Data	15
2 Fundamentals and Background: Change Detection in Multitemporal Hyperspectral Images	21
2.1 Hyperspectral Sensors	21
2.2 Change Detection in Hyperspectral Images	26
2.2.1 Challenges of Change Detection in HS Images	28
2.2.2 Previous Works on Change Detection in Hyperspectral Data	28
3 A Hierarchical Method for Individual Tree 3-D Change Detection in LiDAR Data	37
3.1 Introduction	37
3.2 Proposed Hierarchical 3-D Change Detection Method	38
3.2.1 Problem definition	39
3.2.2 Pre-processing	40
3.2.3 Detection of Large Changes	41
3.2.4 Single-Tree Change Detection	42
3.3 Experimental Results	48
3.3.1 Experimental Setup	48
3.3.2 Results	51
3.4 Conclusion	59

4	A Method based on Binary CVA for Multiple Change Detection in Hyperspectral Images	61
4.1	Introduction	61
4.2	Proposed Method for Unsupervised Change Detection in Hyperspectral Data	63
4.2.1	Binary Change Detection	64
4.2.2	Hyperspectral Change Vectors Binary Coding	64
4.2.3	Compressed Binary Hyperspectral Change Vectors Analysis	68
4.3	Experimental Results	70
4.3.1	Experimental Setup	70
4.3.2	Results	75
4.4	Conclusion	80
5	Methods for the Fusion of Multitemporal LiDAR Data for Individual Tree Characterization	85
5.1	Introduction	85
5.2	Proposed Method for Compound Tree Detection	87
5.2.1	Bayesian Framework to Compound Tree Detection	88
5.2.2	Rule-Based Approach to the Estimation of Statistical Terms	89
5.2.3	Iterative Compound Tree Detection Algorithm	91
5.2.4	Experimental Results	92
5.3	Proposed Method for the Estimation of Crown Parameters on Low Density Data	95
5.3.1	Crown Parameters Estimation on High Density Data	96
5.3.2	Crown Parameters Estimation on Low Density Data	97
5.3.3	Experimental Results	99
5.4	Conclusion	102
	Conclusion	105
	List of Publications	111
	Bibliography	113

List of Tables

1.1	Summary of the techniques showing the densities of the datasets at each date.	16
2.1	Main parameters of some future spaceborne HS missions.	26
2.2	Summary of the techniques showing the resolution of the HS datasets used in each work.	29
3.1	Parameters values defined for the proposed method.	50
3.2	Confusion matrices of the detection of large negative changes	54
3.3	Numerical results of the tree detection.	54
3.4	Statistics of the individual tree parameters.	58
4.1	Compression of the codewords of five pixels.	68
4.2	Quantitative results comparison among the proposed method, the S ² CVA and the BS-SVM for the simulated and BentonRM datasets.	76
4.3	Confusion matrix for the multiple CD results of the BentonRM dataset. . .	77
5.1	Numerical results of the compound tree detection.	94
5.2	Error matrix related to class transitions obtained by the proposed compound approach.	94
5.3	RMSE results on the 10 trials obtained by the single-date estimation and the proposed the method.	101

List of Figures

1.1	Acquisition principles of airborne LiDAR.	11
1.2	1-D visual representation of the relationship between the footprint and the pulse spacing.	12
1.3	Types of scanning patterns.	13
2.1	Across track scanning acquisition geometries.	22
2.2	Simplified representation of dispersion of radiation in the visible wavelength range.	23
2.3	Topology of the CD problem in HS data.	27
3.1	Architecture of the proposed method for the detection of large changes and single-tree changes.	39
3.2	Hierarchical tree structure of the considered CD problem in forest areas.	39
3.3	Example of the first phase of the segmentation.	44
3.4	3-D models fitted on the segmented point clouds.	45
3.5	CHMs of the 4 stand plots at times t_1 and t_2	49
3.6	Plots showing the residual registration error (on the GCPs) versus the amount of artificially introduced shift.	52
3.7	Plots showing the residual registration error (on the GCPs) versus the amount of artificially introduced rotation for different shifts.	53
3.8	Example of the detection of large changes for stand S3.	54
3.9	True versus estimated crown radius (cr) for all the stands at the two dates.	55
3.10	Qualitative examples of delineated tree-canopies obtained by the proposed crown following approach.	55
3.11	True versus estimated base height (bh) for all the stands	56
3.12	Maps representing the different kinds of change identified in the considered stands.	57
3.13	Real example of CD at the individual tree level.	57
4.1	Block scheme of the proposed method for unsupervised multiple CD.	63
4.2	Qualitative illustration of the quantization step of the proposed technique.	65
4.3	Example of a dendrogram.	71
4.4	Simulated dataset.	71
4.5	Benton County agricultural area dataset.	72
4.6	Reference map of the 6 classes of change.	72
4.7	Albacete province agricultural area dataset.	73

4.8	Sensitivity analysis results.	75
4.9	CD results for the BentonRM dataset.	76
4.10	CD results for the Benton dataset.	79
4.11	Details of the CD maps of the Benton dataset.	80
4.12	CD results for the Albacete dataset.	81
4.13	Details of the CD maps of the Albacete dataset.	82
5.1	Block scheme of the proposed compound method for tree-top detection. . .	87
5.2	Example of features extraction.	90
5.3	Example of compound tree detection maps in 4 plots.	93
5.4	Block scheme of the proposed fusion method for crown parameters estimation.	95
5.5	Block scheme of the experimental setup.	100
5.6	Difference between the average RMSE obtained by the single-date approach and by the proposed method.	102

List of Abbreviations

1-D	One-Dimensional
2-D	Two-dimensional
3-D	Three-dimensional
ABA	Area Based Analysis
ACD	Anomalous Change Detection
AGB	Above Ground Biomass
ATREM	ATmospheric REMoval
BHCV	Binary Hyperspectral Change Vector
BS	Band Selection
CBHCV	Compressed Binary Hyperspectral Change Vector
CD	Change Detection
CE	Commission Errors
CEQ	Covariance Equalization
CHM	Canopy Height Model
CKRX	Cluster Kernel Reed-Xiaoli
CNN	Convolutional Neural Network
CVA	Change Vector Analysis
DBH	Diameter Breast Height
DE	Differential Evolution
DMC	Direct Multidate Classification
DTM	Digital Terrain Model
DSM	Digital Surface Model
EHR	Extremely High spatial Resolution
EM	Expectation Maximization
FLAASH	Fast Line-of-sight Atmospheric Analysis of Spectral Hypercubes
GCP	Ground Control Point
GIFOV	Ground Instantaneous Field Of View
GPS	Global Positioning System
HCV	Hyperspectral Change Vectors
HS	Hyperspectral
HSCD	Hyperspectral Change Detection
ICA	Independent Component Analysis
ICP	Iterative Closest Point
Ifov	Instantaneous Field of View
IMU	Inertial Measurement Unit

IR-MAD	Iterative Reweighted Multivariate Alteration Detection
KDE	Kernel Density Estimator
LAI	Leaf Area Index
LiDAR	Light Detection And Ranging
LMF	Local Maxima Filtering
LSM	Level Set Method
MAD	Multivariate Alteration Detection
MAE	Mean Absolute Error
MAF	Maximum Autocorrelation Factor
MNF	Minimum Noise Fraction
MS	Multispectral
MSCD	Multispectral Change Detection
MSU	Multitemporal Spectral Unmixing
NN	Neural Network
NRMSE	Normalized Mean Square Error
OA	Overall Accuracy
OE	Omission Errors
PDF	Probability Density Function
PCC	Post Comparison Classification
PRF	Pulse Repetition Frequency
QCEQ	Class-Conditional Covariance-Equalization
RADAR	RAdio Detection And Ranging
RF	Random Forest
RMSE	Root Mean Square Error
RS	Remote Sensing
RX	Reed-Xiaoli
S ² CVA	Sequential Change Vector Analysis
SAM	Spectral Angle Mapper
SAR	Synthetic Aperture Radar
SFA	Slow Feature Analysis
SID	Spectral Information Divergence
SNR	Signal to Noise Ratio
STICA	Spatio-Temporal Independent Component Analysis
SVM	Support Vector Machine
T-PCA	Temporal Principal Component Analysis
UAV	Unmanned Aerial Vehicle
UPGMA	Unweighted Pair Group Method with Arithmetic Mean
VNIR	Visible Spectrum and Near Infrared
WDS	Wavelength Dependent Segmentation

List of Symbols

LiDAR

P_e	Transmitted power
P_r	Reflected power
d_e	Directivity of transmitting laser
A_r	Receiving lens aperture
A_e	Transmitting lens aperture
σ	Target laser cross section
O	Combined optical efficiency of the transmitter/receiver
l_w	Laser beam width
λ	Wavelength
τ	Pulse Duration
R_T	Target distance
R_R	Range resolution
R_{un}	Maximum unambiguous range
c	Light speed
\mathcal{P}^1	Point cloud acquired at time t_1
\mathcal{P}^2	Point cloud acquired at time t_2
$\mathbf{p} = (x, y, z)$	LiDAR point in the 3-D space (x, y, z)
$\Upsilon = \{\Upsilon_l, \Upsilon_c, v_n\}$	Set of all classes
Υ_l	Class of areas affected by large changes
Υ_c	Class of areas with forest canopy cover present at both dates
v_n	Class of areas of no interest for forest change studies
v_{ln}	Class of large negative changes
v_{lp}	Class of large positive changes
v_{ng}	Class of trees with no significant growth between the two dates
v_g	Class of trees that have changed between the two dates
dH	Vertical growth
dV	Volume growth
$T = [R t]$	Rigid transformation
R	Rotation matrix
t	Translation vector
$\{\mathbf{p}_q^1, \mathbf{p}_q^2\}_{q=1}^Q$	Set of Q matched LiDAR points between the two dates

$\mathbf{p}_q^1, \mathbf{p}_q^2$	qth matched point at times t_1 and t_2
d	Euclidean distance between two LiDAR points
\mathcal{E}	Residual registration error
D	Set of Euclidean distances
ψ_q	Binary variable for the selection of matched pairs of points
PCT	Percentile
$CHM_D(x, y)$	Difference image of $CHM^2(x, y)$ and $CHM^1(x, y)$
$CHM_{D,lp}(x, y)$	Map of large positive changes
$CHM_{D,ln}(x, y)$	Map of large negative changes
T_{lp}	Minimum height variation of large positive changes
T_{ln}	Minimum height variation of large negative changes
T_A	Minimum area of large changes
$CHM_{D,l}(x, y)$	Map of large changes
$\{\mathbf{s}_{k^1}^1\}_{k^1=1}^{K^1}$	Set of K^1 candidate tree-tops at time t_1
$\{\mathbf{s}_{k^2}^2\}_{k^2=1}^{K^2}$	Set of K^2 candidate tree-tops at time t_2
T_s	Maximum distance between two matched candidate tree-tops
$\mathcal{S}^1 = \{\mathbf{s}_k^1\}_{k=1}^K, \mathcal{S}^2 = \{\mathbf{s}_k^2\}_{k=1}^K$	Sets of K matched tree-tops at times t_1 and t_2
$\mathbf{s}_k^1, \mathbf{s}_k^2$	k th tree-top at times t_1 and t_2
$\{\mathbf{s}_j^1\}_{j=1}^J$	Set of J neighbouring tree-tops of \mathbf{s}_k^1
T_r	Search radius of neighbouring tree-tops
$\ell_{k,j}$	2-D line connecting \mathbf{s}_k^1 and \mathbf{s}_j^1
$\Upsilon_{k,j}^1$	Values of CHM^1 along $\ell_{k,j}$
R_k^1, R_k^2	Segmentation regions of the k th tree at times t_1 and t_2
C_k^1, C_k^2	Segmented point clouds of the k th tree at times t_1 and t_2
zh_k^1, zh_k^2	Top heights of the k th tree at times t_1 and t_2
$(xh_k^1, yh_k^1), (xh_k^2, yh_k^2)$	Tree-top positions of the k th tree at times t_1 and t_2
bh_k	Base heights of the k th tree
ch_k^1, ch_k^2	Crown heights of the k th tree at times t_1 and t_2
cr_k^1, cr_k^2	Crown radii of the k th tree at times t_1 and t_2
cc_k	Crown curvatures of the k th tree
Ξ_k^1, Ξ_k^2	Areas of 2-D convex hull at of the select points in C_k^1 and C_k^2
r	Residual of the fitting of the 3-D model on the point cloud
E_k^1, E_k^2	3-D models fitted on C_k^1 and C_k^2
T_{dH}	Minimum vertical growth
T_{dv}	Minimum horizontal growth
dH_k, dV_k	Vertical and crown volume growths of the k th tree
R^2	Coefficient of determination
$\Phi = \{\phi_0^t, \phi_1^t\}, (t \in \{1, 2\})$	Set of all classes
ϕ_0^1, ϕ_0^2	Tree-top class at times t_1 and t_2
ϕ_1^1, ϕ_1^2	Non tree-top class at times t_1 and t_2
$(\mathbf{f}_k^1, \mathbf{f}_k^2)$	Sets of features of the candidate tree-tops $(\mathbf{s}_k^1, \mathbf{s}_k^2)$

$P(\phi_i^1, \phi_j^2 \mathbf{f}_k^1, \mathbf{f}_k^2)$	Joint conditional posterior probability of the pair of classes (ϕ_i^1, ϕ_j^2) given the feature vectors of the candidate tree-tops $(\mathbf{f}_k^1, \mathbf{f}_k^2)$
$p(\mathbf{f}_k^1, \mathbf{f}_k^2 \phi_i^1, \phi_j^2)$	Joint class conditional PDF of the sets of features $(\mathbf{f}_k^1, \mathbf{f}_k^2)$ given the classes (ϕ_i^1, ϕ_j^2)
$P(\phi_i^1, \phi_j^2)$	Joint prior probability of having ϕ_i^1 at time t_1 and ϕ_j^2 at t_2
$p(\mathbf{f}_k^1, \mathbf{f}_k^2)$	Joint PDF of the sets of features $(\mathbf{f}_k^1, \mathbf{f}_k^2)$
$p(\mathbf{f}_k^1 \phi_i^1)$	Single-date class-conditional PDF of \mathbf{f}_k^1 given class ϕ_i^1
$p(\mathbf{f}_k^2 \phi_j^2)$	Single-date class-conditional PDF of \mathbf{f}_k^2 given class ϕ_j^2
$P(\phi_j^2 \phi_i^1)$	Probability of class ϕ_j^2 at time t_2 given class ϕ_i^1 at time t_1 (i.e., probability of transition)
$P(\phi_i^1), P(\phi_j^2)$	Prior probabilities of classes ϕ_i^1 and ϕ_j^2
$p(\mathbf{f}_k^1), p(\mathbf{f}_k^2)$	PDFs of \mathbf{f}_k^1 and \mathbf{f}_k^2
$P(\phi_i^1 \mathbf{f}_k^1)$	Posterior probability of class ϕ_i^1 given the feature vector \mathbf{f}_k^1
$P(\phi_j^2 \mathbf{f}_k^2)$	Posterior probability of class ϕ_j^2 given the feature vector \mathbf{f}_k^2
$\{\beta_{k,l}^1\}_{l=1}^4, \{\beta_{k,l}^2\}_{l=1}^4$	Feature vectors of distances of the k th candidate tree-tops at times t_1 and t_2
T_β	Threshold on the distances in $\{\beta_{k,l}^t\}_{l=1}^4, (t = 1, 2)$
$\gamma_k^t, (t = 1, 2)$	Measure of the likelihood of candidate tree-top $\mathbf{s}_k^t, (t = 1, 2)$ being an actual tree-top
T_γ	Threshold on the likelihood $\gamma_k^t, (t = 1, 2)$
M^n	Matrix of probabilities of transitions at iteration n
m_{ij}^n	Probability of transition $P(\phi_j^2 \phi_i^1)$ at iteration n
ϵ	Threshold on convergence of the iterative algorithm
$\mathcal{S}_C^1, \mathcal{S}_C^2$	Sets of classified candidate tree-tops at times t_1 and t_2
\mathcal{P}^H	High density point cloud
\mathcal{P}^L	Low density point cloud
\mathcal{S}^H	Set of tree-tops detected in \mathcal{P}^H
$\mathcal{R}^H = \{R_k^H\}_{k=1}^K$	Set of segmentation regions for \mathcal{P}^H
$\{C_k^H\}_{k=1}^K$	Set of segmented point clouds of \mathcal{P}^H
$\{C_k^L\}_{k=1}^K$	Set of segmented point clouds of \mathcal{P}^L
$(zh_k^H, ch_k^H, cr_k^H, cc_k^H)$	Crown parameters of the k th tree in \mathcal{P}^H
$(zh_k^L, ch_k^L, cr_k^L, cc_k^L)$	Crown parameters of the k th tree in \mathcal{P}^L
$(zh_k^V, ch_k^V, cr_k^V, cc_k^V)$	Validation crown parameters of the k th tree
bh_k^H, bh_k^L	Base heights of the k th tree in \mathcal{P}^H and \mathcal{P}^L
Ξ_k^L	Areas of the 2-D convex hull of the selected points in C_k^L
κ	Regularization term
ζ	Weight of the regularization term
$r\kappa$	Residual of the fitting of the 3-D model on the point cloud with the regularization term

Hyperspectral

w	Detector width
f	Focal length
h	Platform altitude
v	Platform equivalent ground speed
ΔT	Line scanning time
n	Refractive index
θ	Angle of incidence/refraction/diffraction of a radiation
d_l	Distance between the lines of a diffraction grating
x	Order of the diffracted spectrum
I^1	Hyperspectral image at time t_1
I^2	Hyperspectral image at time t_2
B	Number of spectral channels
I_b^1, I_b^2	Images of the b th band at times t_1 and t_2
I_D	Difference (or HCV) image of I^2 and I_1
I_ρ	Magnitude image of I_D
$\Omega = \{\omega_u, \Omega_C\}$	Set of all classes
ω_u	Class of unchanged pixels
Ω_C	Class of changed pixels
ω_v	Class of the v th type of change
$\{\mathbf{h}_n\}_{n=1}^N$	Set of N Hyperspectral Change Vectors
\mathbf{h}_n	n th HCV
$h_{n,b}$	Spectral value of the band b for the n th HCV
$\mathbf{h}_b = \{h_{n,b}\}_{n=1}^N$	Set of values of the b th component of the N HCVs
$p_{\mathbf{h}_b}(\mathbf{h}_b)$	Probability density function of \mathbf{h}_b
M_b	Number of modes of $p_{\mathbf{h}_b}(\mathbf{h}_b)$
$\{\mathbf{h}_b^m\}_{m=1}^{M_b}$	Group of M_b sets of quantized HCVs
\mathbf{h}_b^m	m th set of quantized HCVs
Q_b	Number of bits required to code the quantized HCVs of band b
$\{\mathbf{w}_n\}_{n=1}^N$	Set of N BHCVs
$\mathbf{w}_n = \{w_{n,i}\}_{i=1}^I$	n th BHCVs
$w_{n,i}$	Value of the i th bit of \mathbf{w}_n
I	Number of bits of the BHCVs
\mathbf{w}'_n	Sorted BHCV
η	Sum of N Hamming distances between adjacent pair of bits
T_η	Threshold on bit redundancy
$\{\mathbf{c}\mathbf{w}_n\}_{n=1}^N$	Set of N CBHCVs
$\mathbf{c}\mathbf{w}_n = \{cw_{n,j}\}_{j=1}^J$	n th CBHCVs
$cw_{n,j}$	Value of the j th bit of $\mathbf{c}\mathbf{w}_n$
J	Number of bits of the CBHCVs
$\{\mathbf{u}\mathbf{c}\mathbf{w}_u\}_{u=1}^U$	Set of U unique CBHCVs

P_u	Prior probability of the u th unique CBHCVs
T_P	Threshold on the prior probability P_u
δ	UPGMA distance between clusters of unique CBHCVs
T_δ	Parameter related to the sensitivity to the different changes
\mathcal{K}_c	Cohen's Kappa Coefficient

Introduction

This Chapter provides an introduction to the PhD thesis. In the first part the main motivations of the thesis are provided. We briefly analyze the importance of monitoring the dynamics of the environment and how remote sensing can provide a significant contribution to such activity. The second part presents the objectives of the thesis and describes each proposed novel contribution. Finally the thesis structure is reported.

Motivations

Planet Earth is characterized by natural and anthropogenic processes and thus is continuously changing. In order to monitor both the natural environment and the areas characterized by the human presence, it is important to track, model and understand these changes. Indeed, understanding the dynamics of such changes is critical to better study their causes and consequences. This allows for an improved knowledge of the environment which can then be used to mitigate the effects of negative changes in view of the preservation of the multiple and diverse natural environments (e.g., forests and glaciers). When dealing with forests, modeling the dynamics of these areas, such as the growth rate of trees, is important for forest management applications both at local and national scale. Indeed, detailed information about the state of a forest can be employed not only for evaluating its health status but also to define efficient and sustainable strategies for the management of the forest both from the environmental and economic points of view. This information can be used also in several contexts at the global level such as the United Nations Framework Convention on Climate Change (UNFCCC) and the related programs for reporting human induced emissions and removal of carbon dioxide considering also forest areas and land use [1]. Land use should be monitored not only to study the effect of anthropogenic processes on the environment but also to manage in a more time and cost effective way a wide variety of human activities (e.g., agriculture). In the context of agriculture, the always increasing request of agricultural products, and thus of cultivable lands, requires an improvement in the management of the limited resources such as water both to increase production and reduce the environmental impact. Regardless of the type of process to be monitored, a common requirement is the availability of quantitative and accurate data that characterize one or more characteristics of the given surface or area. Such data can be obtained via field observations which however are expensive and time consuming to acquire, especially when dealing with large areas or very rough terrain such as a mountainous scenario where lack of access is common. All these factors becomes even more relevant in the case of multitemporal applications since field measurements

have to be acquired at multiple dates thus significantly increasing the required effort. In this framework, Remote Sensing (RS) offers significant advantages with respect to the analysis based on field observations. Indeed, RS sensors, due to their ability to measure quantitatively multiple properties of an object or surface without requiring to be in direct physical contact with it, can be mounted on board aircrafts and spacecrafts that fly over a given area or orbit around the planet thus acquiring data over large areas in a short time period. This is a key advantage with respect to field measurements which in contrast are spot observations representing a limited portion of the analyzed area. Moving to the multitemporal framework, due to the possibility of flying the aircraft multiple times over the same area and to the repeat pass nature of satellites, multiple acquisitions of RS data can be performed in the same geographical area at a relatively low cost compared to field measurements campaigns. For all these reasons, the data acquired by RS sensors are an important information source for the monitoring of Earth's surface. Regarding the specific topic of multitemporal analysis, Change Detection (CD) has been one of the most important research topics in the RS community. CD in RS is the process that aims at detecting changes of the area of interest by analyzing two or a series of RS data (e.g., optical images) acquired at different times over the same geographical area [2].

Currently there are many sensors capable of acquiring data with enhanced resolution. Among them we recall LiDAR and HS sensors. LiDAR scanners have the capability of accurately characterizing the 3-D structure of the analyzed scene. Due to this unique capability among RS sensors, LiDAR data have been widely used for forestry applications. Indeed, the point cloud representing the structure of the forest canopy can be used for an accurate forest parameters estimation both at stand and single-tree level. Area Based Analysis (ABA) has been widely used for the analysis of large forest such as the large wooded areas of the northern European countries that have been scanned in a nation wide effort. When dealing with a full scale analysis of very large forests, ABA methods show favorable characteristics both from methodological and practical points of view. These characteristics are related to the computational cost, the irregular sampling of the sensor and the density of the point cloud. In greater detail, when compared with single-tree methods, ABA methods are less computationally demanding since they work on unit areas (e.g., grid cells) larger than the individual tree crown thus requiring the processing of a smaller number elementary units. Furthermore, ABA methods do not require the detection and delineation of individual trees which are both high computational cost operations. Working on large unit areas decreases the sensitivity to the irregular sampling of the sensor since it is unlikely that large portions of the unit area are not hit by the LiDAR. Therefore, it is reasonable to assume that, for each grid cell, a sufficient number of LiDAR points is available to carry out the analysis of interest. This is not the case for individual trees especially when the pulse density is low, increasing the possibility that a given tree is hit by too few or no pulses. In contrast, ABA methods perform well even with very low pulse density data showing stable results with densities as low as 0.1 pulses/m²[3, 4]. This factor allows for high altitude (with respect to the ground) acquisitions thus decreasing acquisition time and costs. Due to these properties, these approaches are being used for the definition of forest management policies at the regional and national level [5-7] and also in the framework of the United Nations Programme on Reducing

Emissions from Deforestation and Forest Degradation (UN REDD) [8]. However, ABA methods have also important limitations that should be considered. First, large amount of reference data, which are expensive and time consuming to acquire, are required in order to obtain reliable estimates [9]. Most importantly, ABA methods work best when applied to homogeneous forests. This is not always the case. For example, in complex mountain forests one stand may contain different tree species or trees with significantly different ages and different growing behavior [10] related to the highly variable terrain morphology of mountainous areas. Therefore, using one model to represent an entire stand may lead to inaccurate results. Moreover, in such areas there is also an high variability of environmental conditions between different stands due terrain properties such as fertility and position (e.g., elevation) [11], which in turn implies a high variability between stands. Beside these problems, it is important to underline that single tree information is highly valuable [12] for characterizing both the vertical and horizontal structure of each tree [13]. This detailed information can be used in the framework of precision forestry to provide added value and cost savings in the forest management process [14]. As an example, the information regarding individual trees can be used for managing harvesting operations [10] or for defining growth models [15]. Moreover, the single-tree analysis output can also be aggregated at different levels such as groups of adjacent trees with similar properties providing results not only at the single-tree level but also at the area level. Therefore, the more detailed information extracted by the single-tree analysis can be used to provide more accurate results at the area level considering also additional metrics with respect to the ones extracted by ABA methods. It is worth noting that area and single-tree level methods are not mutually exclusive. Indeed, they could be used to improve parameters estimation [16] or to provide training data for area based approaches by working at the individual tree level [17]. Another very interesting aspect of the synergistic use of ABA and single-tree results is the possibility of providing results at different scales. In [14] the authors hypothesize a future for precision forestry in Finland where the base product will be forest attributes maps at a medium spatial resolution (i.e., 10-20 m). Single-tree information will be provided using LiDAR data in the areas where more detailed information is required.

Moving to the multitemporal framework, the rich information content of high density LiDAR point clouds can be used to accurately model the changes of the individual trees. To this date, their use in CD has been limited mainly to ABA methods due to both a lack of high density multitemporal datasets and methodological challenges that have still to be addressed to properly detect changes at the single-tree level. However, the number of new acquisitions carried out on areas already scanned in the past is increasing with new large areas acquisitions that are being carried out also at high density (e.g., in countries such as Norway [18], Finland [19] and Denmark [20]) thus significantly widening the availability of bitemporal or multitemporal point clouds. This require the development of ad-hoc methods capable of exploiting the current and future multitemporal datasets. These methods have to address multiple challenges. In particular, the trees not only have to be detected and delineated at both dates but there should be an automatic tree to tree matching in order to perform the CD. The single-tree CD should be able to characterize the growth both in terms of vertical, horizontal and volume variation. Such analysis

requires methods capable of comparing points clouds taking into account the problems related to irregular sampling of LiDAR data and the complex structure of the forest canopy. It is worth noting that older data have been likely acquired at a lower pulse density with respect to recent ones. Therefore, this should be taken into account to avoid wrong growth estimates due to the difference in density. Moreover, the possibility of using the richer information content of the high density data on the low density point cloud to improve the crown characterization should be evaluated. Finally, in order to be used effectively over large areas, such methods should not require the availability of field measurements and thus be unsupervised.

HS sensors can accurately characterize the spectral signature of the analyzed area. Therefore, since distinct objects have different spectral signatures, HS images can be used to discriminate between them and thus to automatically classify the land cover or to detect specific objects. Moreover, since the spectral signature is also influenced by the status of a given object (e.g., the health status of the vegetation), HS images are used to monitor multiple characteristics of the analyzed area. If the time variable is considered, HS data can be used to monitor the evolution and the changes of a given surface from the spectral point of view. Indeed, the accurate characterization of the spectrum can be used in CD applications not only to detect changes (i.e. binary CD) but most importantly to discriminate between different kinds of change (i.e., multiple CD). Regarding passive optical sensors, multiple CD has been carried out using mainly Multispectral (MS) data due to several reasons [21]: i) the increasing number of satellites mounting on board MS sensors and the decreasing revisit time allowing for frequent bitemporal datasets, and ii) the policies for free distribution of large data archives (e.g., Landsat Thematic Mapper [22] and Sentinel-2A and 2B [23]). It is important to underline that MS images sample the spectrum in few and wide, in terms of wavelength, bands thus providing only a partial representation of the spectral signature of the surface of interest. In terms of CD, this implies that Multispectral CD (MSCD) can be used only to detect changes related to significant spectral variations across a wide portion of the spectrum. These are changes corresponding to abrupt land-cover transitions (e.g, vegetation to urban area). However, changes related to spectral variations in a narrow portion of the spectrum (such as water content change in crops or different growth rates) can not be detected using the limited spectral sampling of MS data [24]. In contrast, HS sensors perform a dense spectral sampling of the spectrum with narrow bands providing a detailed representation of the spectral signatures of the analyzed objects. This higher level of detail in the representation of the spectral signature can be used for the discrimination of changes that are not spectrally visible in MS images. To this date, the availability of multitemporal HS datasets is still quite limited since most of the existing HS sensors are airborne and a few spaceborne HS sensors are operative today. However, several spaceborne HS missions are planned for the next years (see Chapter 2) with some of them already launched, such as the “PRecursores IperSpettrale della Missione Applicativa” (PRISMA) mission. This will lead to an increase of the number of images acquired in the same area at different dates. Therefore, ad-hoc methods capable of exploiting the richer information content of HS images are required since methods developed for MS data are not capable of effectively using the dense sampling of the spectrum. The poor availability of dataset

has led to a scarcity of HSCD methods and thus several challenges related to the analysis of multitemporal HS images are still open. In addition to the problems present also in MSCD, when using HS images a new set of critical issues should be considered. These issues are mainly related to the high dimensionality of HS images which has both technical and methodological implications. From the technical point of view, HS images require large storage and their processing is characterized by a relatively high computation load. Regarding the methodological problems, these are mainly related to data redundancy and to the fact that some of the changes could have a spectral signature only slightly different with respect to other changes. Indeed, for a given change there may be other changes with spectral signatures differing only in a small portion of the spectrum. Therefore, effort should be devoted to understand how the change information is represented in order to extract only the part relevant to the CD problem. Moreover, the new methods should take into account the concept of change that may vary depending on the application of interest thus requiring an adaptive approach in the discrimination of the changes. Note that such methods should be unsupervised since multitemporal reference data are seldom available.

Objectives

The literature shows significant gaps regarding the use of multitemporal LiDAR and HS data (Chapters 1 and 2). In particular, most of the CD methods for LiDAR point clouds work at area level and require ground measurements, whereas little research has been done regarding the analysis of the growth of individual trees. Regarding HS multitemporal analysis, most of the existing methods address the binary and anomaly CD, while multiple CD has been seldom addressed. In this thesis, we aim to exploit the rich and detailed information content of bitemporal LiDAR point clouds and HS images. In greater detail, the main objectives of the thesis are:

- The design of a method for CD at the individual tree level in LiDAR point clouds to detect both large changes (e.g., tree cut) and small changes (e.g., tree growth).
- The definition of an efficient representation of the change information in each spectral channel of HS images and a technique using this novel representation to perform multiple CD.
- The design of methods that fuse the information of bitemporal point clouds to improve tree-crown characterization at the single-date.

Novel Contributions

According to these objectives, in this thesis we focused our attention on the development of CD methods for LiDAR point clouds and HS images and bitemporal fusion methods for LiDAR data. All the methods have been developed to be unsupervised and automatic. The main contributions of the thesis are:

1. A method for individual tree CD in LiDAR data by working directly in the point cloud domain.
2. An unsupervised multiple CD method for HS images.
3. Two methods for the fusion of bitemporal LiDAR data for individual tree-crown characterization.

In the following, a brief description of the three contributions is presented.

A Hierarchical Method for Individual Tree 3-D Change Detection in LiDAR Data

The analysis of LiDAR data allows for an accurate characterization of the tree-canopy. In this work, two point clouds acquired at different times over the same area are used to detect changes at the individual tree level. The comparison of two point clouds is a challenging problem due to the irregular nature of the data that is typically addressed by working in a regularized 2-D domain. However, such an approach does not allow one to exploit the rich information content of the LiDAR data. Therefore, to better use these data, the proposed method performs the comparison directly in the point cloud domain. To this end, first the two point clouds are co-registered using an Iterative Closest Point (ICP) algorithm to avoid false alarms due to registration errors. Then, after the Digital Terrain Model (DTM) subtraction, the Canopy Height Models (CHMs) of the two dates are compared to automatically detect large changes. The bitemporal analysis of the individual trees is carried out following an object-based approach. In greater detail, the individual trees are first separately detected at both dates. For each tree at one date the corresponding one is identified at the second date. Then, the tree-crowns are delineated. The growth of each tree is then estimated using a 3-D model to reconstruct the shape of the tree. Differently from most of the existing methods, the proposed approach estimates both the vertical and horizontal growth to characterize also the growth of canopy volume. Note that thanks to the use of the 3-D model, the method can compare point clouds with significantly different pulse densities. The effectiveness of the method has been tested on two bitemporal datasets acquired in the Trentino province with pulse densities ranging from 10 to 50 pulses/m². Results confirmed that the proposed method can effectively detect both large changes and the growth of individual trees.

A Method based on Binary CVA for Multiple Change Detection in Hyperspectral Images

The dense sampling of the spectrum provided by HS sensors is widely used to automatically classify the land cover. Multitemporal HS datasets can be therefore used to detect and discriminate between multiple spectral changes. To this date, due to the limited availability of multitemporal datasets and the challenges that have to be addressed to perform multiple HSCD, few methods addressed this problem. This thesis presents a method for unsupervised multiple HSCD. After the computation of the difference image, the method focuses on the individual spectral channels to define an efficient representation that highlights the change information. This is done by analyzing the radiometric

information of each band to define, in an adaptive way, a quantized and discrete representation of the relevant change information. This is different with respect to most of the methods of the literature that use band selection or band reduction techniques to simplify the representation of the change information. Indeed, such techniques work better with changes with significantly different spectral signatures. Changes that show small differences in their spectral signatures (and are detectable in a small number of bands) could be lost after the application of such techniques. In contrast, the individual analysis of all spectral channels and their combination after focusing on the change information helps in preserving its informative content. The quantized information of each band is then coded using binary codewords thus obtaining a binary representation of the change information. This binary representation is used in an hierarchical clustering to define a dendrogram (i.e., a tree structure) that allows us to discriminate between the different kinds of change. The tree structure allows us to tune the method for different levels of sensitivity in the change discrimination, thus allowing for different levels of details in the resulting CD map. The method has been tested on simulated and real bitemporal HS images acquired by ground based and spaceborne sensors. Both quantitative and qualitative results showed that the proposed method is capable of detecting and discriminating between the different kinds of change.

Methods for the Fusion of Multitemporal LiDAR Data for Individual Tree Characterization

Multitemporal LiDAR data are an important information source not only for CD applications but also for an accurate estimation of tree parameters. Indeed, the information contained in the two point clouds can be fused to improve the parameters estimation at single-date. In particular, the characterization of the individual trees can gain from the fusion since missing (or poor) information content at one date can be integrated with the information contained in the LiDAR data acquired at the other date. It is worth noting that the fusion has to be carried out without losing the different information content of the two point clouds in order to preserve the bitemporal information. In this thesis, two methods for the estimation of crown parameters based on the fusion of bitemporal LiDAR data are presented.

The first method is a compound approach to the detection of tree-tops in coniferous forests. It aims also at the detection of large changes such as cut or new planted trees. The method first detects the tree-tops separately at the two dates and then models the different probabilities of transition from the first to the second date (e.g., "tree to tree", "tree to not tree", etc). To this end, each tree-top is characterized by geometrical features at both dates that are used to estimate the probability of a candidate tree-top of actually being a tree at a given date. These probabilities are used iteratively to estimate a matrix of probabilities of transition taking into account the temporal dependence between the two LiDAR point clouds. The individual probabilities and the transition matrix are then used considering a Bayes rule for minimum error to decide if a candidate tree-top is an actual tree-top or if it is a false alarm.

The second method exploits the information content of high density data to improve the estimation of crown parameters on low density point clouds. It first detects and de-

lineates the individual tree-crown independently at the two dates. It then reconstructs their shapes using a 3-D parametric model, which allows us to estimate the main crown parameters. The model is first fitted on the high density point cloud using an optimization approach. Then, the method focuses on the low density point cloud and uses the crowns positions and boundaries extracted from the high density data to delineate the trees in order to avoid the use of an automatic segmentation algorithm on low density data. Finally, the crown shape is reconstructed using the same parametric model and optimization algorithm used for the high density point cloud. However, the parameters extracted in the high density data are now considered to improve the estimation. To this end, the method uses boundary conditions for the parameters to be estimated considering the natural dynamics of the tree. Moreover, a regularization term is used in the cost function of the optimization algorithm to model the assumption that the tree-crown changes slowly in time.

Experimental results obtained by applying both the developed methods to bitemporal LiDAR data confirmed that the point clouds acquired at different times over the same area can be effectively used to improve the crown characterization at each single-date.

Structure of the Thesis

This Chapter provided a brief introduction to the use of bitemporal LiDAR and HS data and described both the objectives and the main contributions of this thesis. The rest of the thesis is organized in five chapters. Chapter 1 describes the main characteristics of airborne LiDAR to provide a basic knowledge of how the point clouds are acquired and how the acquisition settings influence the LiDAR data. This is to help in understanding the challenges related to the analysis of single-date LiDAR data and the comparison of two point clouds. Then, it provides an overview of the existing works for CD in multitemporal LiDAR data for forestry applications. Chapter 2 describes the optical imager focusing on HS sensors providing an overall view of the peculiar characteristics of HS sensors useful for later defining the CD problem in HS data. It also reports a state-of-the-art review of HSCD methods.

The first contribution is presented in Chapter 3, which describes the proposed method for individual tree CD using LiDAR data. Chapter 4 describes the method for unsupervised multiple CD in HS images. Chapter 5 illustrates the accurate characterization of individual tree-crowns based on the fusion of bitemporal LiDAR point clouds.

Finally, the last Chapter draws the conclusions of this thesis and analyzes possible future developments of the considered works.

Chapter 1

Fundamentals and Background: Change Detection in Multitemporal LiDAR Point Clouds

This Chapter¹ presents a review of the fundamentals of LiDAR remote sensing and of the literature on Change Detection in multitemporal LiDAR data. The first part provides an overview on the main characteristics of LiDAR sensors to help in identifying and understanding the challenges related to the comparison of two point clouds. The second part analyzes the challenges that have to be addressed when developing CD methods in multitemporal point clouds for forest analysis. Finally, a state-of-the-art analysis of the existing works for CD in LiDAR data for forestry applications is provided.

1.1 Airborne LiDAR Sensors

Remote sensing sensors can be split into two main categories, passive and active [25]. Active sensors use an internal source of illumination to irradiate the scene of interest and measure the reflected signal. The emitted signal varies significantly from sensor to sensor ranging from radio waves for RAdio Detection And Ranging (RADAR) to optical waves for LiDAR sensors. The LiDAR sensor uses a laser to measure the distance between the sensor and the object. Moreover, also the intensity of the backscattered signal is measured. Compared to RADAR sensors, LiDAR can achieve higher spatial resolution due to the high directivity of the laser pulse. LiDAR sensors have been mounted on spacecraft, aircraft and ground support. Spacecraft LiDAR is typically used for atmospheric studies whereas airborne and ground-based LiDAR sensors have proven to be an important tool for a precise analysis of the forest thanks to their capability of producing point clouds that accurately represent the canopy structure. In this thesis we will focus only on small laser footprint airborne LiDAR which is the most common set-up for forestry applications.

¹Part of this Chapter appears in:

[J1] D. Marinelli, C. Paris, L. Bruzzone, "A Novel Approach to 3-D Change Detection in Multitemporal LiDAR Data Acquired in Forest Areas," in *IEEE Transactions on Geoscience and Remote Sensing*, vol. 56, no. 6, pp. 3030-3046, June 2018.

As pointed out previously, LiDAR works by measuring the distance between the sensor and the object of interest. This is done by measuring the time passed between the emission of the pulse by the transmitter and the detection of the reflected pulse by the receiver (which is in the same position of the transmitter). Typically, airborne LiDAR sensors use a single laser beam in the near infrared range (e.g., 1064 nm). However, nowadays the first multispectral LiDAR instruments are becoming available such as the Titan LiDAR [26] which emits three laser beams at 532, 1064 and 1550 nm.

Similarly to the RADAR, the reflected power P_r measured at the sensor can be expressed as a function of the emitted power P_e and others variables depending on the instrument and the target. The main factors affecting the received power are the: i) target distance R_T , ii) directivity of the transmitting lenses d_e , iii) receiving lens aperture A_r , (iv) target laser cross section σ and (v) combined optical efficiency O of the transmitter and receiver. In this formulation we assume the laser transmitter as an isotropic point source. Accordingly, the power density at the target is:

$$\frac{P_e d_e}{4\pi R_T^2}. \quad (1.1)$$

The directivity d_e can be expressed as a function of the laser beam width l_w as $d_e = 16/l_w^2$. Since the laser beam width can be computed as a function of the transmitting lens aperture A_e and of the laser wavelength λ as:

$$l_w = \lambda \sqrt{\frac{\pi}{4A_e}}, \quad (1.2)$$

it is possible to rewrite d_e as $d_e = 64A_e/(\lambda^2\pi)$. If the target is smaller than the laser beam width, the reflected power is distributed over an hemisphere [27]:

$$\frac{1}{2\pi R_T^2}. \quad (1.3)$$

Considering all the other factors P_r can be computed as:

$$P_r = \frac{P_e}{8(\pi R_T^2)^2} \frac{64A_e}{\lambda^2\pi} \sigma A_r O. \quad (1.4)$$

Assuming that the lenses of transmitter and receiver have the same aperture (i.e., $A_e = A_r = A$), it is possible to simplify the equation as:

$$P_r = \frac{8P_e A^2 \sigma O}{\pi^3 R_T^4 \lambda^2}. \quad (1.5)$$

Depending on the type of LiDAR, the emission of the laser can be continuous wave or pulse based. Continuous wave LiDAR emits a continuous waveform whereas pulse LiDAR emits discrete pulses. Continuous wave LiDAR typically transmits a sinusoidal waveform and analyzes the frequency spectrum and polarization of the reflected signal. In contrast, pulse LiDAR measures the time passed between the emission and the detection of the

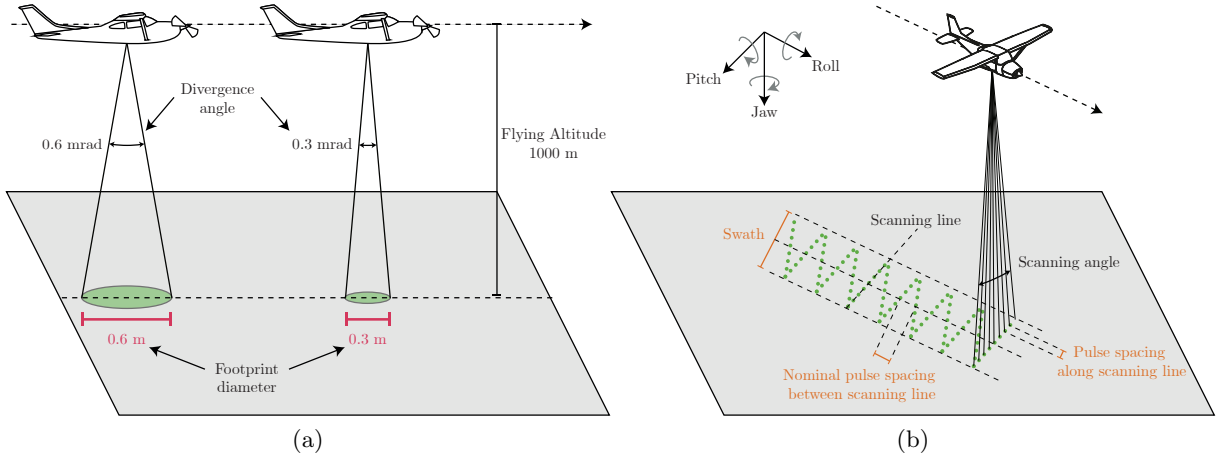


Figure 1.1: Acquisition principles of airborne LiDAR²: (a) relationship between divergence angle and footprint, (b) acquisition geometry of airborne LiDAR.

reflected signal and its intensity. In this thesis we focus on pulse LiDAR since it allows us to obtain distance measurements and thus an accurate representation of the 3-D structure. As for pulse RADAR systems, pulse LiDAR is regulated by two main parameters which are the duration of the pulse τ and the interval rate of emission of the pulses (Pulse Repetition Frequency (PRF)). The same equations of the RADAR case can be used to compute the range resolution R_R and the maximum unambiguous range R_{un} which is half the maximum distance that a pulse can travel between two consecutive pulses. Assuming an ideal laser pulse with a rectangular waveform in time, the two quantities are computed as:

$$R_R = \frac{c\tau}{2}, \quad R_{un} = \frac{c}{2PRF}, \quad (1.6)$$

where c is the speed of light. The reflected signal can be measured in a discrete way by recording individual returns (e.g., single return or multiple returns) or by measuring the full reflected signal (full waveform LiDAR). Full waveform LiDAR have proved to be effective for forestry applications [28, 29] even though to this date these data are seldom available. All the data used in this thesis have been acquired by small footprint discrete return pulse LiDAR sensors.

The spatial resolution of the LiDAR sensors is strongly correlated with the laser footprint which indicates the area illuminated by a single laser pulse. The footprint is typically much larger than the one that could be obtained with an ideal laser since in real conditions the signal disperses while propagating in space. The signal dispersion can be modelled with a cone shape and it is defined by the divergence angle (or beam divergence). Due to this assumption the footprint is typically estimated as the diameter of the base of the cone (Figure 1.1a) which can be computed given the flying height above the ground. Therefore, the same LiDAR sensor will have different footprints depending on the flying altitude. The footprint size strongly affects the type of signal that will be measured. In the case of forestry applications, a large footprint increases the possibility of penetration in the lower

²Images reproduced from [30].

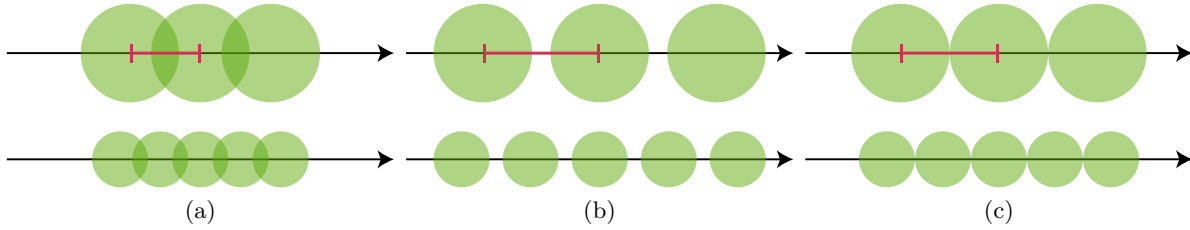


Figure 1.2: 1-D visual representation of the relationship between the footprint (green circles) and the pulse spacing (red line) for three cases³: (a) footprint larger than the pulse spacing, (b) footprint smaller than the pulse spacing, (c) footprint equal to the pulse spacing.

portion of the canopy and of having multiple returns. With a smaller footprint it is more likely that the pulse illuminates only a homogeneous surface which means that multiple returns are less likely. However, a smaller footprint allows for a higher level of detail. Note that since the energy of a pulse is constant, the increase of the footprint leads to a spread of the energy over a larger area thus decreasing the signal to noise ratio.

Given the footprint, the pulse spacing on the ground (i.e., the pulse density) has to be defined accurately in order to have a proper acquisition. Note that in this thesis we will refer to pulse density and not to point density. The pulse density is affected by numerous parameters such as the PRF, scan angle and scan speed, platform velocity and altitude. The pulse spacing has to be consistent with the footprint of the sensors. If the distance between two adjacent points is smaller than the footprint (Figure 1.2a), the two footprints overlap and a single object may be registered as a return in different pulses. If the pulse distance is larger than the footprint (Figure 1.2b), there will be gaps between the points leading to portions of the scene not being scanned. The optimal case is having the footprint diameter equal or similar to the nominal pulse spacing (Figure 1.2c).

LiDAR, by measuring the round trip time of the laser pulse, estimates the distance between the sensor and the target. In order to reconstruct the absolute geographic coordinates, the platform position and orientation have to be considered. The position of the platform is measured using a differential Global Positioning System (GPS) while a Inertial Measurement Unit (IMU) is used to measure the orientation (pitch, roll and yaw for the airborne case). To produce the point cloud, the LiDAR sensor changes the orientation of the laser emitter and exploit the platform (e.g., airplane) movement to scan the area of interests. Different scanning patterns exists depending on the way the laser pulses orientation is changed to scan the area. All of the patterns are characterized by an oscillatory movement of the direction of emission of the pulse in a direction perpendicular to the flying direction. The oscillation is typically achieved by having the laser emitter fixed and by moving (e.g., rotating) a mirror that reflect the laser. One of the most common scanning pattern for forestry applications is the z-shaped pattern [30] (Figure 1.3c). An important parameter of each scanning pattern is the maximum scan angle which is the maximum angle from the nadir direction at which the sensor work. The scan angle and the flying height above ground are used to compute the scanning swath (Figure

³Images reproduced from [31].

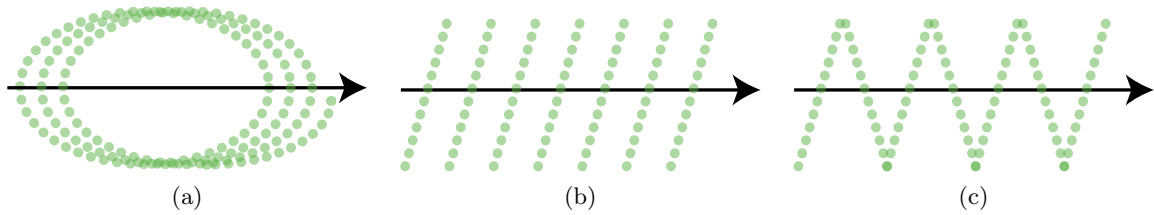


Figure 1.3: Types of scanning patterns⁴. The green dots represent single laser pulses.

1.1b). This parameter strongly influences the acquisition costs since a small scanning swath requires more flights to scan the same area with respect to a larger one. However, the maximum scan angle can not be increased too much since as the scan angle increases the penetration capability decreases. Moreover, when the angle becomes too large the accuracy of the estimates of forest structure metrics decreases [32, 33].

1.2 Change Detection in LiDAR Data for Forestry

Change Detection in LiDAR data for forestry is an important application since it allows for an extensive and objective analysis of forest dynamics over large areas. However, to this date, the analysis of LiDAR data for forestry applications is mainly focused on single-date analysis both at area [34–36] and single-tree level [37–39]. The limited availability of multitemporal techniques for LiDAR data is due to several factors, both technical and methodological. Technical factors are mainly related to the small number of multitemporal point clouds. Indeed, in the past few LiDAR acquisitions have been performed with a very small number of repeated flights. However, in the last years systematic LiDAR acquisitions are being performed more commonly and thus nowadays planning new acquisitions over areas scanned in the past is becoming more and more interesting since the time interval between two acquisitions would be large enough to allow for a detectable growth of the forest structure. Moreover, an increased availability of data will be achieved in the next years thanks to the Unmanned Aerial Vehicles (UAVs). Indeed, due to their relatively low cost and their automatic nature, it will be possible to program them to fly over a certain area multiple times with little human interaction. This significant increase of datasets availability could be used to analyze multiple acquisitions at different time intervals. This is very important since it will allow us to study the dynamics of forest areas over different periods of time. In this framework, several manufacturer of LiDAR sensors such as Riegl are producing compact sensors specifically designed for UAVs [40]. The first results showed that UAV LiDAR can be effectively used for forestry applications [41, 42] since they have proved to produce point clouds similar to ones acquired by traditional airborne LiDAR data [41]. In contrast, spaceborne LiDAR probably will not be a data source for precision forestry applications. Indeed, due to the high altitude of satellites, spaceborne LiDAR sensors have a very large footprint (e.g. 65 m for the Geoscience Laser Altimeter System [43]). Therefore, such sensors have been used mainly for atmospheric studies [44] while

⁴Images reproduced from [30].

their use for forestry applications is limited only to very coarse analysis [45, 46]. New spaceborne LiDAR will have a smaller footprint (i.e., smaller than 50 m for the ICESat-2 Laser Altimetry Mission [43]) but in the near future small footprint acquisitions will be achieved only with ground and airborne LiDAR.

From the methodological point of view, the comparison of two point clouds is a challenging problem due to two main factors:

- the pulse density of the two point clouds can be significantly different.
- The irregular sampling of the LiDAR pulses results in measures that are not uniformly distributed.

These factors makes a point-to-point comparison of the two data unfeasible. Indeed, it would require to have, for each point at one date, a corresponding point at the second date in order to analyze the change in position of a given object or structure. Such a condition could be possible only with very high density data in a highly regular scenario such as urban areas. This is not the case of forest areas. Indeed, the irregular nature of trees amplifies the problems introduced by the irregular sampling of the LiDAR sensor since pulses emitted in the same direction and from the same platform position at multiple dates are likely to hit different parts of the canopy structure even if it has not changed.

It is worth noting that, regardless of the method used to compare the two point clouds, the LiDAR data have to be properly pre-processed in order to minimize the effects errors during the acquisition phase. In particular, to obtain satisfactory results the two point clouds have to be registered. The problem of 3-D point cloud registration has been extensively analyzed in the literature. The Iterative Closest Point (ICP) [47] algorithm is one of the most common solutions adopted in a large variety of datasets and contexts. ICP allows a fine registration of overlapping 3-D point clouds by iteratively estimating the transformation parameters. The errors are distributed among all the points of the sets to limit distortion while preserving the geometry of the entire scene [48, 49]. However, since it is an iterative descent algorithm, a good a priori alignment should be provided to reach the global minimum. Moreover, a major bottleneck is the rate of convergence. To refine the registration results and reduce the computational burden, local features can be employed considering object-based approaches [50] or using local features [51, 52].

In order to detect changes at the individual tree level, the individual tree crowns have to be identified and delineated. Many methods have been presented in the literature to perform the segmentation both in the CHM and point cloud domains [10, 53–56]. A typical approach is the search for the maxima in the CHM, which are then used as seeds in a region growing approach [53]. In [54], the authors perform the segmentation by working both in the regularized domain of the CHM (to delineate the crowns) and in the point cloud domain (to distinguish between understory and overstory vegetation). In [55], the point cloud is seen as a 3-D multimodal distribution where each mode represents a possible tree crown. A mean-shift algorithm is used to identify the considered modes. Other methods are based on a directional analysis of the crown profile in the point cloud domain [56] and in the regularized domain [10].

1.2.1 Previous Works on Change Detection in LiDAR Data

Due to the challenges previously described and the limited availability of multitemporal data, to this date the research activity regarding CD in LiDAR data is still quite limited, especially when compared with other RS data such as MS images. In the following, a review of existing methods is provided. The existing works for CD in LiDAR data for forestry applications can be categorized either from an applicative or a methodological point of view. In this thesis we provide an analysis of existing papers grouped according to the three methodological categories used in [7, Chapter 15], which discriminates the methods according to the considered level of spatial detail: i) ABA methods, ii) methods for the analysis of canopy gaps and ii) methods working at individual tree level. Table 1.1 shows a summary of the cited techniques together with the pulse density of the used datasets. Note that the manuscripts do not always report how the density was estimated (e.g., considering all returns or only the first one) and therefore the reported densities may not be fully comparable.

ABA Methods

Let us first focus on methods that perform the CD at area (i.e., an area characterized by trees with homogeneous characteristics) level or by working in coarse resolution spatial grids. These methods are typically used when the available data are characterized by low pulse density. Indeed, when dealing with low density data single-tree level methods perform poorly since each tree-crown is hit by few or even no LiDAR pulses. ABA methods are often applied to dataset representing very large areas. This is due to several factors such as the very high computational power that would be required to apply single-tree level methods to large datasets. Most importantly, when dealing with very large areas, forest services are typically more interested in large scale maps than information about changes of the individual trees since the former results allow for a more efficient management of large forests.

Instead of directly comparing the point clouds, the multitemporal analysis is performed on the parameters estimated from the LiDAR data at stand level or on a larger scale. One of the most common parameter used to measure change is the Above Ground Biomass (AGB) variation. The AGB variation can be estimated in a direct or indirect way [57]. In the indirect estimation the AGB is estimated separately at the two dates and the variation is computed as the difference of the two estimates. In the direct estimation the AGB variation is directly estimated on a measure of change derived from the difference of LiDAR metrics. In [58, 59], the authors proposed both direct and indirect approaches for AGB variation estimates. In the direct case, the AGB variation is estimated using as variables the difference of LiDAR metrics such as height percentiles or canopy density. In the indirect estimation, linear models are fitted to the reference data separately at the different dates and the AGB variation is computed as the difference of the estimates. In [59], the authors analyze the accuracy of the estimates for different categories of changes such as deforestation and degradation (i.e., partial biomass loss). In [60] two approaches for AGB variation are proposed and compared to the three approaches proposed in [58]. The results of [60] showed that the best approach for AGB change estimation is the indirect

Table 1.1: Summary of the techniques showing the densities of the datasets at each date. Methods that fall into two categories are shown twice.

Category	Reference	Density [pulses/m ²]	
		t_1	t_2
ABA	Meyer et al. [57]	LF	5.6
	Bollandsås et al. [58]	3.4	4.7
	Næsset et al. [59]	1.2	7.3
	Økseter et al. [60]	1.2	6.9
	Andersen et al. [61]	25	14
	Réjou-Méchain et al. [62]	4	20
	Huang et al. [63]	LF	LF
	McRoberts et al. [64]	1.2	7.3
	Bollandsås et al. [65]	8	9
	Solberg et al. [66]	$t_1: 4.6, t_2: 4.9, t_3: 4.4$	
	Næsset and Gobakken [67]	1.2	0.9
	Hopkinson et al. [68]	$t_1: 2.5, t_2: 3.6, t_3: 2.8, t_4: 3.2$	
	Socha et al. [69]	4	6
Noordermeer et al. [70]	0.9	11.8	
Canopy Gaps	St-Onge and Vepakomma [71]	0.3	3
	Vepakomma et al. [72]	0.3	3
	Vepakomma et al. [73]	0.3	3
	Yu et al. [74]	10	10
	Vastaranta et al. [75]	Fused (7, 9.8)	11.9
Single-Tree	St-Onge and Vepakomma [71]	0.3	3
	Yu et al. [74]	10	10
	Yu et al. [76]	10	10
	Yu et al. [77]	10	10
	Vepakomma et al. [78]	0.3	3
	Srinivasan et al. [79]	GB	GB
	Xiao et al. [80]	$t_1: 10-15, t_2: 30-50, t_3: 30-50$	

*LF = Large Footprint, GB = Ground-Based

one. This conclusion is in contrast with the results of [58] where the direct method proved to be the best approach. Contrasting results were obtained also for the other approaches. The authors concluded that the type and characteristics of the forest influence the accuracy of the results and thus should be taken into account when selecting the most appropriate model. In [61], the authors independently estimate the AGB at the two considered dates by calculating the AGB in areas where reference data are available using an allometric equation. Then a regression based on LiDAR metrics is used to estimate the AGB over the entire area at a resolution of 50 m thus obtaining two AGB rasters. The difference between the two raster is then used to analyze areas with selective logging. Similar approaches are proposed in [62, 63] considering different spatial resolutions (0.25 and 1 ha). In [63], the AGB variation is used to analyze areas with and without forest disturbances. In [57], a comparison between direct and indirect estimation of the AGB variation is presented. The direct method showed to be accurate with a spatial resolution no higher than 10 ha whereas the indirect one showed accurate estimates of the AGB at single-date at a scale of 1 ha. However, change estimates showed to be accurate with an error similar to the one of the ground estimates only if the resolution is lowered to 10 ha. Other comparisons between indirect and direct methods for AGB change estimation are proposed in [64, 65]. In both works, the authors concluded that the indirect method is more accurate with respect to the direct one. Moreover, [65] pointed out that only the direct method requires to have field measurements at both dates in the same stand in order to define the AGB change model.

Note that AGB is not the only variable that can be used to measure change in forests. In [66], the variation of the Leaf Area Index (LAI) is estimated indirectly to analyze the effects of an insect attack on Scots pines using three LiDAR acquisitions. The LAI is related with the gap fraction which is an inverse measure of the canopy density. Ground reference data are used to estimate via regression the one parameter of the model. The LAI is then estimated at the three dates at 10 m resolution with the variation computed as the difference between the rasters. In [67], the authors consider the difference of both metrics extracted directly from the two LiDAR data and metrics estimated using a model defined by regression (indirect approach) to detect growth. In the indirect approach, the model, used for both dates, is defined considering only the first date in order to avoid that different models impact on the growth estimation. The results show that both the types of metrics used to detect growth can be effectively used even though the change in biophysical parameters estimated using the model shows a noticeable difference with respect to the reference data. In [68], growth is estimated considering only metrics extracted directly from the LiDAR data and the height values of local maxima in the CHM in order to understand which is the most suitable approach. The results showed that the uncertainty of the growth estimates can be considered acceptable if the time interval between the two acquisitions is no shorter than 3 years.

Research effort has been devoted also to the estimation of site productivity [69, 70]. Forest productivity is typically represented by Site Index (SI) models defined as a growth trajectory relating tree age and height. SI is typically estimated using the stand age and height [81, 82]. If multitemporal LiDAR data are available, the growth estimate computed from the point clouds can be used to search for a growth trajectory consistent

with the dynamics of the stand. In [69] the estimated growth is used with the age of the individual stands to fit five different functions for the growth trajectory modeling. Using reference models, the best growth trajectory is selected considering both fit statistics and the number of parameters. In [70], the SI is estimated following a direct and an indirect approach. The direct approach uses LiDAR derived metrics computed at the first date and the difference of such metrics between the two dates together with ground measurements of age and height to fit the growth trajectory. In the indirect method, ground reference dominant height values are used in a regression to define a model for its estimation using LiDAR derived metrics. The model is then used to estimate the dominant height at both dates and the difference of the two estimates together with the time interval is used in an exhaustive search for the SI.

Almost all the described methods require to have reference data to select the best model for the estimation of the forest metrics of interest (e.g., by regression or exhaustive search). Since the reference data have to be acquired in multiple areas in order to model the diversity of the environment, a significant amount of effort has to be dedicated to this step. All these factors make the reference data acquisition a costly and time consuming operation.

Canopy Gaps Analysis Methods

Another type of approach that overcomes the problem of comparing two point clouds is the comparison of the CHMs computed at the two dates. The regularization step allows for a comparison of the data in a regularized domain which is not affected by the non uniform laser sampling and the irregular structure of the crown. These methods can be used to detect changes such as canopy gaps, fallen or cut tree or individual tree growth. Focusing on on the former, in [71], the authors search only for new canopy gaps by looking for areas with high elevation in the first date CHM and small elevation at the second date. To this end, two different thresholds are applied to the two CHMs and new gaps are identified in a binary map as the areas that satisfy the criteria at both dates. To reduce noise, the resulting binary image is analyzed to remove patches smaller than 5 pulses/m². Moreover, since the first date is characterized by a low point density, only the detected gaps containing at least 3 pulses are considered. In [72], gaps are separately detected at the two dates searching for areas with small values of CHM. The gap shape is approximated as an ellipse to compute area and perimeter. The two binary images representing the gaps are then compared to detect gap opening, expansion and closing. The authors propose also an analysis of different interpolation algorithms to generate the CHM and analyze the selection of the best spatial resolution for the rasterization considering the pulse density. In [73] the authors use an approach similar to the one proposed in [73] to separately detect the gaps at the two dates. The comparison is used to analyze other types of gaps dynamics such as merging of two adjacent gaps or splitting of a gap. Moreover, several statics such as gap frequency per hectare and mean gap size are computed at both dates and compared to better study the gaps dynamics. In [74], the authors apply a threshold to the difference image of the CHMs to identify new canopy gaps. Then, after a morphological opening to reduce noise the image is segmented to identify the location of the cut trees. In [75], the difference of the CHM is used to study

the damages caused by snow. A threshold is applied to the difference image followed by multiple steps to reduce noise producing a binary map which is then analyzed considering the positions of the individual trees to search for crowns damaged by snow.

Single-Tree Level Methods

The analysis of individual tree growth requires to detect and delineate all the trees at both dates and then match them in order to compare the tree at the first date with the same tree at the second date. This introduces an additional challenge with respect to ABA methods, including an increased sensibility to the accuracy of the registration between the two point clouds. After these steps, the information have to be extracted from the segmented data and then compared to detect changes in the 3-D structure of the crown. As previously pointed out, the change information at the individual tree level can be used for precision forestry applications providing more detailed data with respect to ABA methods.

In [71], the tree growth is computed considering the statistic over clusters of trees grouped according to spatial or species criteria. In the case of spatial grouping, percentile of height is used to estimate growth, whereas in the case of species classification for each tree species the average height is used. In [74, 76], the vertical growth of a tree is computed as the difference between the highest LiDAR points of the considered tree at the two dates. This estimate is computed under the hypothesis that there is at least one laser pulse that hits the tree-top at both dates. This hypothesis can be considered valid if the pulse densities of the two point clouds are relatively high (i.e., greater than 5 pulses/m²). If this condition is not satisfied, it is possible to evaluate not only the difference of the highest LiDAR points of the tree at the two dates but also the difference between the mean and median of the values of the Digital Surface Models (DSM) representing the analyzed tree [77]. In [76] no automatic tree detection is proposed while the crown delineation is performed considering a simple cylindrical model. In [78], the authors analyze the relationship between the canopy gaps and the growth of individual trees by comparing the growth of the individual trees on the edge of canopy gaps (i.e., with large part of the canopy not covered by other trees) with the growth of the trees surrounded by other crowns. Regarding the horizontal growth of the canopy, in [74] an estimate is computed by measuring the difference between the areas of the segmentation regions associated to the same tree at the two dates. It is worth noting that these methods works in the point cloud domain by computing height metrics of each tree. However, these methods do not exploit the rich information content of the 3-D tree crown structure present in the point cloud since they consider mainly the vertical information of the LiDAR data. Working in the CHM domain allows for only a partial use of the information content of LiDAR data. Indeed, CHMs represent the upper "surface" of the forest, whereas the information of the lower portion of the canopy structure is lost in the regularization process. Moreover, the horizontal information content of the tree canopy is also negatively affected by the regularization. Therefore, in order to fully model the growth of individual trees, one should work directly in the point cloud domain to extract both the vertical and horizontal information regarding the tree structure.

In [79, 80], the change detection is performed at individual tree level in the point cloud

space exploiting in a more exhaustive way the information content of the LiDAR data. In [79], the authors analyze bitemporal terrestrial LiDAR data to assess AGB changes. For each detected tree, the AGB is estimated using the two LiDAR point clouds separately. Then, the estimates are compared to identify the biomass change per tree. Note that typically terrestrial LiDAR data are characterized by a much higher density with respect to airborne LiDAR point clouds. Moreover, since they scan the trees from the ground they provide a much more detailed representation of the lower portion of the canopy. However, they have to be moved manually through thus requiring a significant amount of time to scan the area of interest. In [80], the authors present a method to detect tree changes in urban areas using bitemporal high density airborne LiDAR data. The parameters of the tree crown are estimated separately on the two LiDAR point clouds and then compared to identify the tree changes. However, the urban environment is typically less challenging with respect to forest areas. This is because trees are well separated or intersect only marginally and therefore they can be identified more easily.

This literature review points out that research regarding the analysis of multitemporal LiDAR data has been devoted mostly to CD at the stand level and to the analysis of canopy gaps. Indeed, due to favorable properties previously described, ABA methods have been already applied, especially for single-date applications, to full scale operational scenarios. Regarding multitemporal applications, ABA methods are being used by countries part of the UNFCCC for reporting greenhouse gas emissions reductions and removals by sinks by estimating change in AGB [83]. In contrast, the detection of the growth of individual trees has been seldom addressed with most of the existing works focused only on the vertical variation of the tree canopy. To this date, there is little research regarding the analysis of the variation of the other crown characteristics such as horizontal and crown volume growth. Such an analysis at the level of individual trees can be performed only by working directly in the point cloud domain in order to fully exploit the 3-D data to characterize the canopy structure. Therefore, significant effort should be devoted to such analysis addressing all the problems related to the CD in the point cloud domain considering also pre-processing steps such as co-registration. These novel methods should also take into account the likely possibility of having point clouds with significantly different pulse densities. This requires methods capable of exploiting the richer information content of the high density data to improve the characterization of the individual trees in the low density data.

Chapter 2

Fundamentals and Background: Change Detection in Multitemporal Hyperspectral Images

In this Chapter¹ a review of the fundamentals of Hyperspectral remote sensing and related works is presented. In the first part the principle of optical images acquisition are described focusing on Hyperspectral sensors to provide information useful for understanding Change Detection in these images and the related challenges that have to be addressed to effectively extract the multitemporal information. In the second part we define the Change Detection problem in HS images and discuss the related challenges. Finally a review of the state-of-the-art of Change Detection in HS images is provided.

2.1 Hyperspectral Sensors

Passive sensors exploit an external source that illuminates the analyzed scene and measure the reflected signal. The reflected radiance is measured in a specific wavelength range such as the Visible Spectrum and Near Infrared (VNIR). It can be measured at a single spectral channel (e.g., pancromatic images) or it can be split into multiple bands to better analyze the spectral behavior of the object of interest. This is the case of sensors that analyze the reflected spectrum at few (Multispectral (MS)) or up to hundreds of bands (HS).

The most common source of illumination is the sun which has the peak of emission at about 500 nm. The passive optical sensors measure the solar radiation reflected by the analyzed surface. However, especially in the spaceborne case, the atmosphere influences the measured signal due to the interaction between the solar radiation and the gas molecules. The atmospheric influence is due to two main factors: (i) solar radiation reflected by the top of the atmosphere and measured by the sensor, (ii) solar radiation passing through the atmosphere being affected by the atmospheric transmittance. The atmospheric transmittance indicates how much of the solar radiation passing through is absorbed by the

¹Part of this Chapter appears in:

[J3] S. Liu, D. Marinelli, F. Bovolo, L. Bruzzone, "A Review on Change Detection in Multitemporal Hyperspectral Images," in *IEEE Geoscience and Remote Sensing Magazine*, vol. 7, no. 2, pp. 140-158, June 2019.

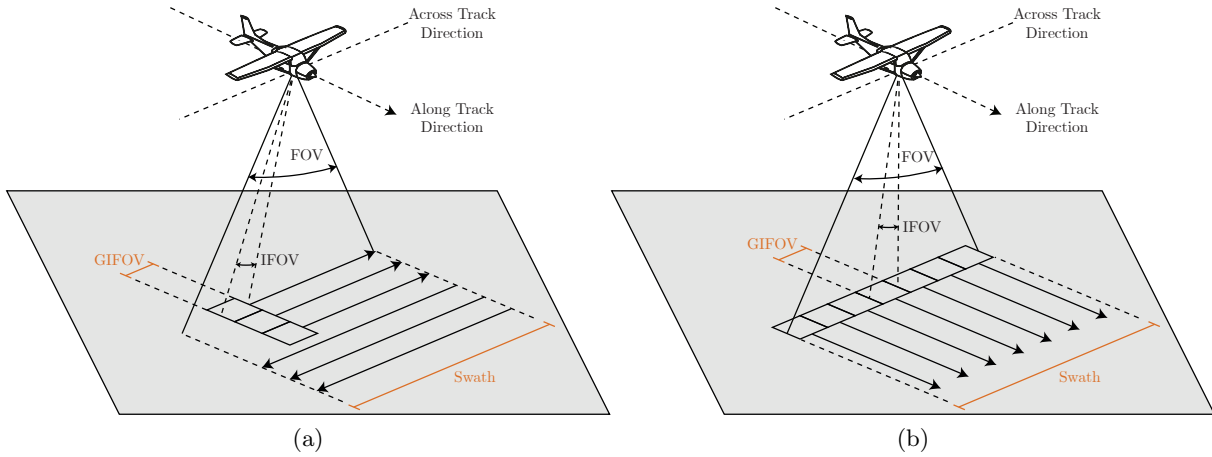


Figure 2.1: Across track scanning acquisition geometries²: (a) whiskbroom scanner, (b) pushbroom scanner.

gas as a function of the wavelength. This factor has to be taken into account during the design of spaceborne passive sensors since only the wavelengths not strongly affected by gas absorption can be used for RS. The atmosphere introduces distortion in the measured signal not only due to absorption but also due to diffusion effects such as Rayleigh and Mie scattering. The first one is related to the presence of small molecules whereas Mie scattering occurs in presence of larger particles caused for example by smoke or aerosol. Due to these scattering effects, the radiation measured at the sensors for a given object is affected also by the radiation reflected by neighbour objects.

As for every digital imager system, RS passive optical sensors acquire the image on a 2-D grid. Typically, optical sensors do not perform a full frame acquisition (i.e., all the pixels are acquired at once) but perform a scanning along the across-track direction (orthogonal to the flight or orbit direction) and exploit the platform movement to scan the area in the along-track direction. Different types of scanning system in the across-direction exist: line, whiskbroom and pushbroom scanners. Line and whiskbroom scanners acquire one or few pixels at a time, respectively and use a rotating mirror to scan the across-track direction. Compared to the line scanner, the whiskbroom requires a lower mirror rotation speed thanks to the multiple detectors that allow for parallel scanning (Figure 2.1a). However, the spatial resolution of both line and whiskbroom scanners is limited by the speed of the rotating mirror. In contrast, the pushbroom scanner is not affected by such limitation since the across-track swath is scanned all at once using an array of thousand of detectors (Figure 2.1b). Therefore, this kind of scanning is the most suitable for high resolution sensors since the spatial resolution is only defined by the optics characteristics. However, note that for all the sensors that use multiple detectors, the calibration of the latter has to be performed accurately to avoid striping artefacts.

The size of the spatial pixel is the spatial resolution and it is defined by the characteristics of the sensors (detector width w and focal length f) and by the platform altitude

²Images inspired by [84].

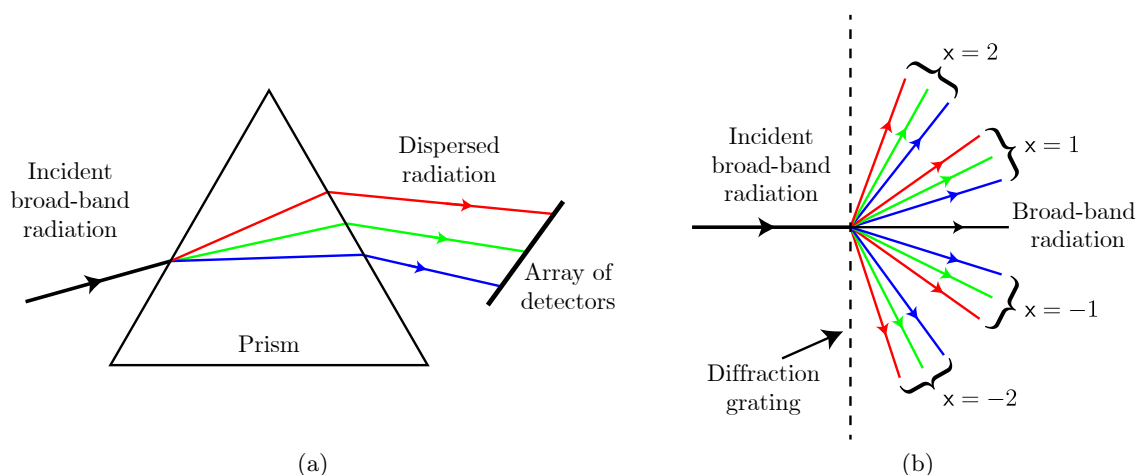


Figure 2.2: Simplified representation of dispersion of radiation in the visible wavelength range by: (a) prism, (b) diffraction grating.

h. Using these parameters the Instantaneous Field Of View (IFOV) and the Ground Instantaneous Field Of View (GIFOV) can be computed. The IFOV is the angle subtended by one detector and depend only on the detector width and focal length:

$$\text{IFOV} = 2 \arctan \left(\frac{w}{2f} \right) \approx \frac{w}{f}. \quad (2.1)$$

The GIFOV is the projection of the IFOV on the ground and thus depend also on the platform altitude:

$$\text{GIFOV} = 2h \tan \left(\frac{\text{IFOV}}{2} \right) \approx \frac{wh}{f}. \quad (2.2)$$

It is worth noting that the time required to scan a single line has to be defined considering the speed of the platform. Indeed, if the line scanning requires too much time with respect to the platform movement, some lines will not be acquired. If v is the platform equivalent ground speed, the line scanning time ΔT should be $\Delta T \leq \text{GIFOV}/v$.

The amount of radiation reflected by a given object depends on its geometric structure, composition and on the radiation wavelength. Therefore, every kind of surface can be characterized by its spectral signature which represents the reflected radiation as a function of the wavelength. By measuring the reflected radiance at multiple wavelengths, MS and HS sensors produce an approximation of the spectral signature which can be used to characterize the analyze object. These two types of sensors can be distinguished by how the reflected radiation is sampled in the spectral domain. MS sensors typically sample the radiation at few wavelengths with a coarse spectral resolution (i.e., broad spectral channels) whereas HS sensors sample the reflected signal at tens or hundreds of spectral channels with a narrow sampling interval thus achieving high spectral resolution. The higher spectral resolution of HS sensors allows for a more accurate approximation of the spectral signature which can be used for a finer discrimination of different objects. Indeed, in RS HS sensors have proven to be a valuable data source for land-cover classification [85–90].

While in MS sensors the separation of the measured broad-band radiation into different spectral components is typically carried out with filters, HS sensors disperse the broad-band spectrum onto an array of detector where each detector measures the reflected radiation in a given wavelength range. The dispersion is typically achieved using prisms or diffraction grating. Prisms are based on the fact that the refractive index of glass varies as a function of wavelength [25]. Therefore, the radiation traveling through the prism is deviated differently depending on the wavelength. The deviation can be defined according to the Snell's law that describes the relation between the incidence angle θ_1 and refraction angle θ_2 of light when passing through a boundary separating two different materials characterized by two refractive indexes n_1 and n_2 . The relation can be defined as:

$$n_1 \sin(\theta_1) = n_2 \sin(\theta_2). \quad (2.3)$$

Since, in the case of void-glass interface, n_2 depends on the wavelength (i.e., $n_2(\lambda)$), the refraction angle θ_2 also depends on the wavelength and can be rewritten as:

$$\theta_2(\lambda) = \arcsin \left(\frac{n_1}{n_2(\lambda)} \sin(\theta_1) \right). \quad (2.4)$$

This equation points out that inside the prism different wavelengths are refracted at different angles. Figure 2.2a shows a basic representation of the dispersion by prism.

A diffraction grating is a panel of transparent material such as glass (or reflective material) upon which multiple parallel dark lines are positioned at a distance d_1 from each other. An incident radiation (perpendicular to the grating) at wavelength λ will be diffracted at an angle $\theta_x(\lambda)$ with respect to the normal to the grating defined as:

$$\theta_x(\lambda) = \arcsin \left(\frac{x\lambda}{d_1} \right), \quad (2.5)$$

where x is an integer (that can assume both positive and negative values) representing the order of the diffracted spectrum. If the incident radiation is a broad-band signal, then it will be dispersed over a given range of angles depending on the wavelength range, distance d_1 and on the value of x . Figure 2.2b shows that different values of x produce multiple spectra of different order. The value $x = 0$ (order of the spectrum equal to 0) corresponds to a 0 diffraction angle for all the wavelengths. Therefore, this 0-order spectrum is equal to the incident radiation in terms of spectral content. Note that the absolute value of x cannot be increased indefinitely. Indeed, if $|x|$ is too large the argument of the arcsin in (2.5) becomes greater than 1 which is not defined since $\sin \in [-1, 1]$. Therefore, the upper limit of $|x|$ (i.e., the highest spectrum order) is defined as $\lfloor d_1/\lambda \rfloor$. An important aspect of any dispersion technique is the angular dispersion which is the angle range over which a given broad-band radiation is dispersed. Indeed, as the angular dispersion increases, more detectors can be used to sample the dispersed radiation thus allowing for higher spectral resolution. In a diffraction grating, the angular dispersion can be increased by decreasing the distance d_1 between the dark lines. However, this may lead to an overlap of the spectra of different order thus requiring a preliminary filtering to limit the wavelength range of the incident radiation. It is worth noting that typically, a radiation with a certain spectral

range is dispersed over a wider range of angles by a diffraction grating with respect to a prism [25].

The spatial and spectral resolution cannot be increased indefinitely. Indeed, as the spatial or spectral resolution increases, the amount of energy at each detector diminishes. Therefore, these two parameters have to be set taking into account the radiometric resolution which is the minimum amount of energy detectable by the sensors. Since this parameter is fixed given the detector, a trade-off between spatial and spectral resolution is required. As an example, if one wants to increase the spectral resolution, the spatial resolution should be decreased in order to respect the radiometric limits. This is one of the main factors that has limited the number of spaceborne HS sensors. Indeed, due to the very high altitude of the satellites, that limits the amount of energy at the sensor, having both high spectral and spatial resolution requires to overcome significant technical challenges. Therefore, to this date HS RS has been limited mainly to airborne platforms using sensors such as HyMap [91] and Aviris [92]. However, as for the LiDAR case, the acquisition of HS data using airborne platforms is costly since it requires ad-hoc flights. This limits the availability of multitemporal datasets.

In contrast to the airborne case, to this date the number of spaceborne HS imagers is very low. Indeed, after the NASA EO-1 satellite (on which was mounted the Hyperion HS sensor) deactivation in March 2017 and the Hyperspectral Imager for the Coastal Ocean (HICO) failure due to a solar storm in September 2014, few spaceborne sensors are still operating. Among them there are the ESA Compact High Resolution Imaging Spectrometer (CHRIS) sensor mounted on the PROBA-1 satellite [93], the Hyperspectral Imager (HSI) sensor mounted on board the Chinese satellite HJ-1B [94], the HyperSpectral Imager (HySI) mounted on board the Indian IMS-1 satellite [95] and the Visual and Infrared Multispectral Sensor (VIMS) mounted on the Chinese Gaofeng-5 (GF-5) satellite that has been launched in May 9, 2018. However, the “PRecursorore IperSpettrale della Missione Applicativa” (PRISMA) [96] launched in March 2019 and in the near future other satellite missions with HS sensors will follow including:

1. “Hyperspectral Imager Suite” (HISUI) that is planned for launch in 2019 [97];
2. “Environmental Mapping and Analysis Programme” (EnMAP) is planned for launch in 2020 [98];
3. “Hyperspectral Infrared Imager” (HypIRI) that is scheduled for launch after 2022 [99];
4. “Spaceborne Hyperspectral Applicative Land and Ocean Mission” (SHALOM) that is scheduled for launch after 2022 [100];
5. “Hyperspectral X IMagery” (HypXIM) that is scheduled for launch after 2023 [101].

Table 2.1 shows the main parameters of these HS missions. These future missions will significantly increase the availability of HS data. Accordingly, HS images will become valuable data source for Earth Observation both for single-date and CD analysis. However, the data distribution policy for these future HS missions is still unclear, which might limit the potential impact on the applications. In addition to satellites, UAVs are likely

to become one of the most relevant platform for HS RS. Several manufacturers are producing miniaturized HS sensors specifically designed to be mounted on UAVs [102]. In this framework, there is an increasing number of works that exploit UAV HS data for different applications such as precision agriculture [103–106], forestry [107–109] and maritime monitoring [110, 111].

Table 2.1: Main parameters of some future spaceborne HS missions (parameters may change before launch).

Parameters		PRISMA [96]	HISUI [97]	EnMAP [98]	HypSIRI [99]	SHALOM [100]	HypXIM [101]
Country		Italy	Japan	Germany	USA	Italy-Israel	France
Spectral range [nm]	VNIR	400-1010	400-970	400-1000	380-2510	400-2500	400-2500
	SWIR	920-2505	920-2500	900-2450			
Spectral sampling [nm]	VNIR	≤12	10	6.5	10	10	10
	SWIR		12.5	10			
Number of bands	VNIR	66	57	88	214	275	210
	SWIR	173	128	154			
Swath Width [km]		30	30	30	185	30	15
Spatial resolution [m]		30	30	30	30	10	8
Revisit time [days]		6	2-60	4-27	16	4	3-5
Planned launch year		2019	2019	2020	≥2022	≥2022	≥2023

2.2 Change Detection in Hyperspectral Images

Change Detection in HS is conducted to represent and discover the temporal changes between the HS image pairs by considering both the spectral signatures in each single time image and the temporal correlation between multitemporal images. To this date, the number of methods for HSCD is still limited due to the limited availability of multitemporal datasets and due to the several additional problems that have to be addressed with respect to MSCD.

Figure 2.3a shows a general block scheme for CD in HS data. The pre-processing steps, such as registration, uncalibrated and noisy band removal, bad band stripes repairing, radiometric and atmospheric corrections, etc., are usually necessary for enhancing the original spectral representation of the input HS images. In particular, an accurate co-registration process in HS images with a limited residual misregistration error sharply impacts on the performance of CD algorithms. Regarding the CD, three main types of multitemporal strategies can be used, which process the HS images relying on: i) an image comparison operator, ii) an image stacking approach, and iii) an independent image analysis. In greater detail, comparison operators model the temporal variations in the multitemporal images according to different techniques, such as univariate image differencing [112], change vector analysis [113], index based differencing [114], distance or similarity measures [115], etc. A summary of the most widely used comparison operators can be found in [21].

The CD problem in HS images can be divided into multiple subproblems among which the most important ones are [116, 117]:

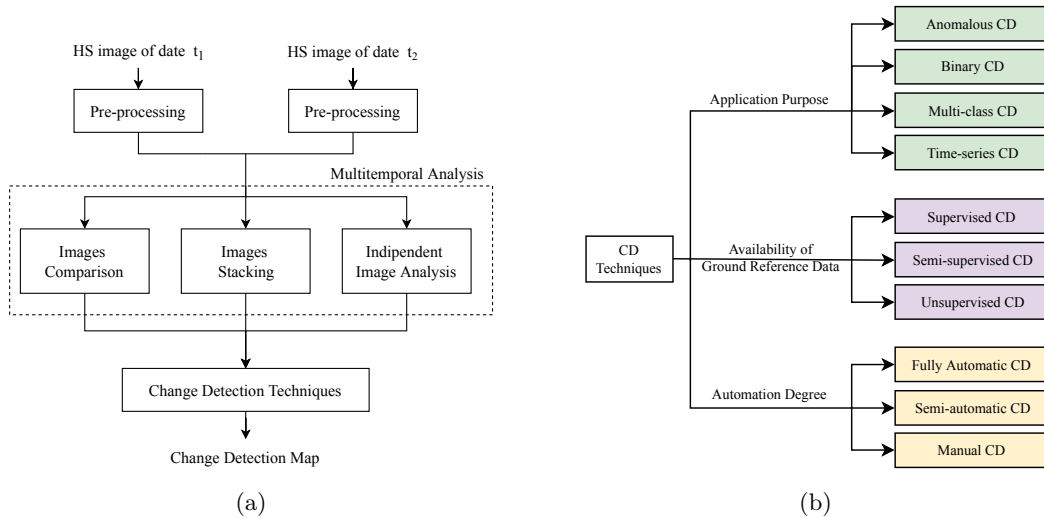


Figure 2.3: Topology of the CD problem in HS data: (a) block scheme of the CD approaches in bitemporal HS images, (b) categories of techniques for CD in HS images.

1. discrimination between unchanged and changed samples;
2. identification of the number of types of change;
3. separation of the samples into the classes representing different kinds of change.

In [24] the authors analyzed the concept of change in bitemporal HS images. In particular, conceptually Hyperspectral Change Vectors (HCVs) can be separated into major changes and subtle changes. Major changes are related to land-cover transitions that have spectral signatures significantly different from each other. Subtle changes show similar behavior to a given major change for most of the analyzed wavelengths but differ significantly only in some components of the spectrum. Subtle changes can be seen as subclasses of the corresponding major change. As an example, a major change representing a major land-cover transition (e.g., from non-cultivated to cultivated) could be divided into subtle changes corresponding to different variations such as water content or different growth rate of the crops. Note that while major changes may be discriminated using MS images, this is not the case for subtle changes since they would be lost (i.e., be grouped with the most similar major change) due to the coarse spectral resolution of such images. Accordingly, HS images can be used to detect a wide variety of changes ranging from major to subtle changes. It is worth noting that different changes can have significantly different relevance from the semantic point of view. Indeed, depending on the application, one may be more interested in detecting the relevant but subtle land-cover transitions. This highlights how the definition of what it is considered as change is not straightforward and depends significantly on the application. Therefore, this aspect should be taken into account when developing CD methods for HS images, for example by organizing the detected changes in a way such that relevance of the different changes is highlighted.

2.2.1 Challenges of Change Detection in HS Images

Even though the use of HS images has key advantages in CD applications with respect to MS images, it also results in significant challenges that have to be properly addressed in order to exploit their rich information content.

One of the main challenge is related to the high dimensionality of HS data. The analysis of high dimensional HS data spaces has proven to be complex and can not be addressed with techniques developed for low dimensional spaces [117, 118]. Indeed, the effectiveness of such techniques decreases due to problems such as reduced efficiency of distance metrics [119] and the Hughes phenomenon [120]. These is due to the fact that the feature space becomes more and more sparse as the number of dimensions increases. In addition to this, high dimensionality introduces challenges in data handling, including storage volume and computing bottle necks, which are actually common problems for all HS images processing tasks (i.e., classification, change detection, target recognition). Another significant problem of HS images is data redundancy. Since a typical HS sensor performs a nearly continuous measurement of the spectrum, for a given pixel adjacent spectral channels have a high probability to contain very similar values of reflected radiance. Therefore, increasing the spectral resolution does not increase the information content indefinitely.

HS sensors are also affected by noise generated by both external sources (atmospheric effects due to absorption and scattering) and internal sources (instrument noise). Note that these noise sources are present also in MS sensors. The atmospheric haze can be mitigated using atmospheric correction techniques such as the ATmospheric RE-Moval (ATREM) [121] or Fast Line-of-sight Atmospheric Analysis of Spectral Hypercubes (FLAASH) [122] algorithms. Instrument noise is introduced by: i) non-ideal electronics (thermal and shot noise); ii) quantization; iii) malfunctioning of the sensors which generate impulsive noise or missing pixels/lines; iv) striping noise due to calibration errors of the array of sensors in pushbroom scanners [116]. Note that when increasing the spectral resolution, the measured reflectance at the sensor decreases whereas signal-independent noise such as the thermal noise does not, thus decreasing the Signal to Noise Ratio [123].

2.2.2 Previous Works on Change Detection in Hyperspectral Data

CD approaches can be grouped in several ways by considering different perspectives. In the literature, there are some review papers that provide classifications of CD techniques [114, 124–126]. However, they are mainly focused on MS images and very few works (e.g., [117, 127]) provide a review of CD techniques in HS images. In general, we can divide CD approaches in HS images by considering different possible variables (Figure 2.3b):

- **Application purpose:** four classes can be defined, including anomalous CD, binary CD, multi-class CD and time series CD methods.
- **Availability of ground reference data:** three classes can be defined, consisting in supervised, semi-supervised, and unsupervised CD methods.
- **Automation degree:** three classes can be defined, including fully automatic, semi-automatic, and manual CD methods.

The following review is developed according to the first categorization since it is the most interesting one from the methodological and application perspectives. Table 2.2 shows a summary of the works described in the following sections grouped according to the categorization selected for this review. Note that several works used more than one dataset considering different acquisition platforms and both real and simulated data. Since the spatial resolution is not always provided, in some cases approximated values based on the acquisition settings are showed.

Table 2.2: Summary of the techniques showing the resolution of the HS datasets used in each work (synthetic datasets are not considered).

Category	Reference	Resolution [m]	Platform	
Anomaly CD	Schaum and Stocker [128]	1x2	Aircraft	
	Shimoni et al. [129]	2.5	Aircraft	
	Theiler et al. [130]	<20 ≈0.04	Aircraft Ground	
	Wu et al. [131]	30	Spacecraft	
	Zhou et al. [132]	≈0.04	Ground	
	Meola et al. [133]	<4 ≈0.04	Aircraft Ground	
	Wu et al. [134]	30 100 30	Spacecraft Spacecraft Spacecraft (sim)	
	Acito et al. [135]	0.6	Aircraft	
	Vongsy et al. [136]	<1	Aircraft	
	Meola and Eismann [137]	≈0.04	Ground	
	Theiler and Wohlberg [138]	3	Aircraft	
	Meola et al. [139]	≈0.04	Ground	
	Eismann et al. [140]	≈0.04	Ground	
	Binary CD	Frank and Canty [141]	20	Aircraft
		Nielsen [142]	5	Aircraft
		Ortiz-Rivera et al. [143]	<0.01	Ground
Nielsen [144]		5	Aircraft	
Liu et al. [145]		30	Spacecraft	
Yuan et al. [146]		30	Spacecraft	
Du et al. [147]		2	Aircraft	
Chen and Wang [148]		30 1.3	Spacecraft Aircraft (sim)	
Du et al. [149]		2 <20	Aircraft Aircraft (sim)	
Ertürk and Plaza [150]		16.7 1.3 3.7	Aircraft Aircraft (sim) Aircraft (sim)	
Ertürk et al. [151]		30 3.4 <5 1.3 3.7	Spacecraft Aircraft Aircraft Aircraft (sim) Aircraft (sim)	

*sim = simulated

Category	Reference	Resolution [m]	Platform
	Ertürk et al. [152]	3.4	Aircraft
		<5	Aircraft
		<20	Aircraft
		1.3	Aircraft (sim)
		3.7	Aircraft (sim)
	Lyu et al. [153]	30	Spacecraft
Wang et al. [154]	30	Spacecraft	
Multiple CD	Liu et al. [24]	30	Spacecraft
		<0.01	Ground (sim)
	Liu et al. [155]	30	Spacecraft
		3.7	Aircraft (sim)
		<0.01	Ground (sim)
	Liu et al. [156]	30	Spacecraft
Liu et al. [157]	30	Spacecraft	
	3.7	Aircraft (sim)	
Time Series CD	Hemissi et al. [158]	30	Spacecraft
		18	Aircraft (sim)
	Yang and Sun [159]	<0.1	Aircraft
		<0.2	Aircraft (sim)
	Henrot et al. [160]	-	Ground
	Veganzones et al. [161]	250	Spacecraft

*sim = simulated

Anomalous Change Detection

Anomalous CD (ACD) aims at identifying anomalous changes between images by suppressing background and accentuating changes [162]. In general, ACD approaches in HS images can be separated into single-instance and multi-instance target detection [137]. The key point is to investigate the statistics of the images, and to increase the detection probability of man-made changes and suppress background in the image scene sequences. For ACD, special attention is usually paid on the detection of small changes resulting from insertion, deletion, or movement of man-made small size objects, and also from the small stationary objects having spectrum changes between images, such as the case of camouflage, concealment and deception [135].

In literature, approaches such as chronochrome [163] and Covariance Equalization (CEQ) [128], are classical algorithms for ACD. They investigate a linear prediction of post-time data using the statistics of both pre-time and post-time data sets, in order to discover and highlight the anomalous change pixels in the unchanged background. In greater detail, in [163] the authors compute the covariance matrices of the spectral signatures at times t_1 and t_2 and the cross-temporal covariance matrix. Then they compute the Chronochrome prediction error between the real signatures at t_2 and the ones predicted using the Chronochrome. The prediction error is then used in the Reed-Xiaoli (RX) anomaly detector to identify changes. In [128], the authors consider a covariance equalization implementation in order to be more robust to registration errors. They exploit an ACD approach that is based on the assumption that the mean spectral signature of the

target is known. They also use a combination of the Chronochrome and matched filtering. In [129], three iterative clustering methods, i.e., class-conditional Covariance-Equalization (QCEQ), bitemporal QCEQ and Wavelength Dependent Segmentation (WDS) are applied to detect man-made changes in HS images. Results proved that the use of a spatially adaptive detector greatly enhanced the ACD performance in target change detection in terms of reduction of false alarm.

Other techniques focus on modelling the data variables from different perspectives. For instance, in [130] the anomalous changes in HS images are modeled and detected according to elliptically contoured distributions. This is motivated by the fact that, since the problem is the detection of anomalous changes which are rare, there is a high probability that these changes are represented in the tail of the statistical distribution. Therefore elliptically contoured distributions may be more suitable compared to Gaussian distribution. In [131], the change residual image is computed based on Slow Feature Analysis (SFA) and changes are detected using the RX anomaly detector. The SFA is used to compute the change residual image in which the unchanged areas and large areas affected by changes show small values. This makes the problem of ACD a classical anomaly detection problem which is solved using the RX algorithm. In [132], a Cluster Kernel RX (CKRK) algorithm is presented. It clusters the background samples while using the cluster centers for anomaly detection. The clustering step is used to cluster the background pixels which are then replaced with the corresponding cluster centers. The RX is then applied to the new samples reducing the computation load. An improved ACD approach that exploits a model-based method is proposed in [133]. It is extended for use on both relatively calibrated and uncalibrated HS images and applied to airborne HS images. In [134], the authors propose a subspace-based CD method by using the undesired class information as prior knowledge. A subspace distance is computed to determine the anomalous pixels as changed when compared with the background subspace. Recently, a tutorial on the ACD problem in HS images within a theoretical gaussian framework is presented [135]. This tutorial addresses several solutions based on the statistical detection theory by formulating the ACD as a binary decision problem.

In the literature, there are also some other works mainly focused on the detection of changes by addressing specific issues, e.g., eliminating image parallax errors [136], registration errors [137, 138], vegetation and illumination changes [139] and diurnal and seasonal variations [140].

Binary Change Detection

The objective of binary CD is to detect and separate the change and no-change classes in the considered multitemporal images. Accordingly, from the spectral point of view, pixels with significant spectral variations between the considered dates have higher probability to be changed, and vice versa. A common way to identify the binary information based on comparison operators such as Change Vector Analysis (CVA) is to construct the compressed change magnitude information as the magnitude of the difference image. Other methods focus on the construction of binary representations based on similarity measures, such as the Spectral Angle Mapper (SAM) [164] or the Spectral Information Divergence (SID) [165]. Therefore, it is possible to use approaches similar to those developed for

Binary CD in MS since the full dimensionality of data is compressed into one magnitude feature space. However, the information redundancy in the adjacent bands might affect the change magnitude and thus the binary CD performance, so the selection of most informative band subsets can be important as pointed out in [118]. Based on the magnitude image, it is possible to model the specific statistical distribution of the two classes (e.g., by Gaussian Mixture [166], Rayleigh-Rice Mixture [167]) under the Bayesian framework and then use thresholding techniques to generate the CD map. Note that in [166] and [167], the statistical distribution parameters are estimated using the Expectation Maximization (EM) algorithm.

Another major group of classical binary CD methods in HS images is designed based on the features extracted by using data transformation techniques. The original high dimensional HS data are transformed into a few components where change information can be compressed and highlighted. Within this context, the Multivariate Alteration Detection (MAD) based on canonical correlation analysis is proposed in [168] and applied to monitor vegetation changes in HS images [141]. The aim of MAD is to find a linear transformation of the two HS images such that a measure of change is maximized. In particular, the linear transformation aims at maximizing the variance of the difference of the two transformed bitemporal data. The extended version, named Iterative Reweighted MAD (IR-MAD), is proposed in [142] to better model the change and no-change background representation. The IR-MAD is an iterative version of MAD, which is based on the re-weighting of the individual samples. In particular, at each iteration each pixel is weighted according to a measure based on the sum of the squared MAD variables.

Temporal Principal Component Analysis (T-PCA) is proposed in [143], which exploits the variances in principal components after transforming the differencing and stacking bitemporal images, respectively. Thus the no-change and change classes are associated with specific principal components. In [144], two kernel versions of Maximum Autocorrelation Factor (MAF) analysis and Minimum Noise Fraction (MNF) analysis are introduced for CD.

Several others recent papers present solutions to the binary CD problem in HS images. In [169], a Spatio-Temporal ICA (STICA) extracts the spatio-temporal patterns from different HS sensors or from different acquisition conditions and dates. The aim of the STICA is to reach signal data independence both in the spatial and temporal domain. In [145], Independent Component Analysis (ICA) is applied with the uniform feature design strategy in a hierarchical framework focusing on the detection of the specific cropland vegetation changes. In [146], a semisupervised method based on a Laplacian regularized metric framework learns a distance metric for detecting changes under noisy conditions. In [147], the authors propose a relative radiometric normalization method and two automatic binary CD approaches after normalization, including a kurtosis maximization-based analysis and a distinct change vector extraction and classification. In [148], the authors propose a spectrally-spatially regularized low-rank and sparse decomposition model for binary CD. The proposed method decomposes the HCV image into three different components, i.e., a locally smoothed low-rank matrix for the clean change features, a sparse matrix for the outliers and an error matrix for the small Gaussian noise. The final change map is obtained based on the k-means clustering applied to the extracted change features.

There is also a group of recent works that address the considered binary CD problem in HS images from the subpixel point of view. In [149], a linear mixture model is applied to analyze the endmembers and abundances estimated from each single-time HS image to address the binary CD problem. In [150], the potential of unmixing for binary CD is investigated based on stacked bitemporal HS images. In [151] and [152], the sparse unmixing methods are exploited. It is worth noting that even though unmixing CD methods can provide results also in terms of abundances of endmembers spectra, the above-mentioned papers only provide results in term of binary CD.

The attention towards CD in HS images using Neural Networks (NNs) is increasing with the first works for binary CD being published in the last years [153, 154]. In [153] the HS data are simply used to simulate MS images to validate a method for binary CD. In [154] a 2-D Convolutional NN (CNN) is used for binary CD. The author propose a novel mixed-affinity matrix to better analyze the cross-channel information of the change vectors. While the use of NNs in RS and more specifically HS images has significantly increased, their use for HSCD is still limited with most of the existing works being focused on MS images [170].

Multiple Change Detection

The goal of multiple CD is to detect and identify different kinds of changes associated with different land-cover transitions, material composition changes or other dynamic variables such as moisture conditions. Compared with the ACD and binary CD tasks, the multi-class CD task is more complex and thus challenging as its aim is not only to detect the changes but also to discriminate different change classes. If comprehensive bitemporal reference data are available, multi-class CD can be carried out by using Post Comparison Classification (PCC) [112] (considering the independent classification on each single-date image) or Direct Multidate Classification (DMC) [171, 172] relying on the stacked bitemporal HS images. However, these methods require reference data which are rarely available for the bitemporal case. Therefore, the design of advanced unsupervised or semi-supervised CD techniques as much independent as possible from the ground reference data is one of the most important tasks for multi-class CD in HS images.

In [24], the authors use a hierarchical spectral change analysis investigating in detail the spectral variations from coarse to fine processing levels. At each level of the hierarchy, changes are analyzed using a change vector analysis in the polar domain. The number of changes is automatically identified and a clustering procedure is applied to identify the multi-class change information. In [155], the authors follows a similar hierarchical approach to the one proposed in [24] where the changes are manually selected at each iteration. At each iteration, the original high dimensional feature space is adaptively and iteratively compressed and projected into a sequence of 2-D feature spaces used for the manual selection. This adaptive representation is used in [156] to provide the prior knowledge of the multi-class change information. This information is used to generate pseudo-training samples for each change class which are then used by a supervised classifier such as Support Vector Machine (SVM) and Random Forest (RF) for classifying the original HCVs or transformed features.

The above works mainly focus on the detection of multi-class changes at pixel-level.

In the literature there are few works addressing CD at subpixel-level. In [173], CD is implemented at subpixel level based on nonlinear spectral unmixing and decision fusion, where the inner-pixel subtle changes are analyzed and multiple land-cover compositions are combined. Although it was originally designed for CD in MS images, this technique can be also applied to HS images with the available reference training data. An unsupervised Multitemporal Spectral Unmixing (MSU) model is proposed in [157]. It investigates the spectral-temporal mixture properties in bitemporal HS images. The CD problem is solved by analyzing the abundances of different distinct bitemporal endmembers (including both change and no-change classes) at subpixel level. Taking advantage from the endmembers extraction and change and no-change spectral compositions within a pixel, the identification of the number of changes is performed by identifying the distinct endmembers and the discrimination of multi-class changes is addressed by linear unmixing and abundance analysis.

CD in Image Time Series

CD in time series exploit long time sequences of HS images to analyze the changes or trends in a given area. The changes of interest for the user may be either abrupt changes that occurred on the land surface or subtle changes present in a given time period. From the current HS satellites, it is still difficult to have a high temporal resolution. Therefore, to this date, there are few works addressing CD in time series of HS images.

In [158], the authors propose a method for modeling the temporal variation of the reflectance response as a function of time period and wavelength. It is designed based on a new 3D model of the spectral signature that considers concurrently the spectral, spatial, and temporal information. In [159], the authors propose an unsupervised CD method for detecting small changes in a bitemporal HS images sequence. The feature space is built using block processing and locally linear embedding, whereas the CD map is generated by clustering the change and no-change binary classes. A framework for dynamically modeling and efficient unmixing a time series of HS images is proposed in [160]. Based on linear mixing process at each time, the spectral signatures and fractional abundances of the pure materials in the scene are viewed as latent variables that follow a dynamical structure. The method uses a spectral unmixing algorithm to estimate the latent variables by performing alternating minimizations. In [161], the authors apply canonical polyadic tensor decomposition techniques to the blind analysis on HS big data that can be either time series or multi-angular acquisitions. The method can be interpreted as a multilinear blind spectral unmixing, where the big HS tensor is decomposed into three factors such as spectral signatures, fractional spatial abundances and temporal/angular changes.

This state-of-the-art review shows that most of the existing HSCD methods are focused mainly on ACD and binary CD. Such techniques exploit only part of the rich information content of HS data since they focus mainly on the detection of change and do not address the discrimination of the different changes. Unsupervised multiple CD has been addressed only by a very limited number of works. Some of these works addressed the complexity of HS data using feature reduction or band selection techniques while little effort has been devoted to the generation of highly representative change features from the high dimensionality spectral channels. In particular, there should be more focus on how

the change information in the individual bands is represented. This requires a detailed analysis of such representation to better understand how the relevant change information of each spectral channel can be identified and highlighted. Indeed, a simpler but exhaustive representation could be effectively used in CD to discriminate between the different changes without losing subtle spectral variations.

Chapter 3

A Hierarchical Method for Individual Tree 3-D Change Detection in LiDAR Data

This Chapter¹ presents a novel hierarchical approach to the detection of 3-D changes in forest areas by using bitemporal LiDAR data. Differently from most of the existing approaches, the proposed method works directly in the point cloud domain to better exploit the rich information content of LiDAR data. The method first detects the large changes (e.g., cut trees) by comparing the CHMs derived from the two LiDAR data. Then, according to an object-based CD approach, it detects the single-tree changes. To this end, first the individual trees are identified and delineated. Then, a 3-D parametric model is used to reconstruct the shape of the tree at both dates and the two 3-D models are compared to estimate both the tree-top and the crown volume growth. The proposed approach can compare LiDAR data with significantly different pulse densities due to the use of the 3-D model, thus allowing the use of a large part of the data available for real applications. Experimental results pointed out that the method can accurately detect large changes, exhibiting a low rate of false and missed alarms. Moreover, it can detect changes in terms of single-tree growth which are consistent with the expected growth rates of the considered areas.

3.1 Introduction

Forests are a living ecosystem characterized by natural and anthropogenic processes and thus they are constantly changing. Hence, it is very important to develop techniques for monitoring forest areas in order to update forest inventories (for management and planning) and to analyze the health of wooded areas (e.g., reduced growth rate due to tree diseases). LiDAR data acquired at different times over large forest areas are a suitable

¹This Chapter appears in:

[J1] D. Marinelli, C. Paris, L. Bruzzone, "A Novel Approach to 3-D Change Detection in Multitemporal LiDAR Data Acquired in Forest Areas," in *IEEE Transactions on Geoscience and Remote Sensing*, vol. 56, no. 6, pp. 3030-3046, June 2018.

information source to perform automatic CD.

From the analysis of the literature of Chapter 1, it turns out that little research regarding the analysis of multitemporal LiDAR data has been carried out. In particular, most of the techniques present in the literature perform the CD at stand level, thus producing maps representing the variation of forest metrics at plot level. Very little has been done regarding the single-tree analysis with most of the papers focusing on the vertical growth of the canopy. For all these reasons, in this paper we propose a novel approach to the detection of large changes (e.g., cut trees) and single-tree changes (i.e., vertical and crown volume growth) in multitemporal LiDAR data. The proposed approach is based on a hierarchical strategy that first detects the large changes and then identifies the changes at the individual tree level according to an object-based approach. This allows us to decompose the complex multitemporal analysis into simpler problems, thus simplifying the 3-D CD problem. While the large changes are detected in the CHM, the object-based approach focuses on the single-tree-crowns directly in the point cloud domain to exploit the full information of the LiDAR data to detect the 3-D changes of the canopy. Unlike most of the literature methods, the proposed approach estimates both the vertical and horizontal growth to characterize the canopy volume growth. Moreover, we are able to perform the CD using point clouds with very different pulse densities. It is worth noting that the crown volume is an important tree parameter which has been demonstrated to be a good predictor for the estimation of the forest biomass [174, 175], for forest fire simulations [176, 177] and for Diameter Breast Height (DBH) estimation [178] (since DBH and crown volume are correlated). In [176] the authors estimate the crown volume and the foliage biomass to compute the single-tree-crown density as the foliage biomass divided by the crown volume. Thus, the detection of the changes of the crown volume is really important for the monitoring of forest areas.

To assess the effectiveness of the proposed approach, experiments have been carried out on two forest areas located in the southern Italian Alps of the Trentino region (Italy). This work focuses on conifers which are the primary tree species in Alpine environment. We used both high density (up to 50 pulses/m²) and medium density (up to 10-15 pulses/m²) LiDAR data. Results confirmed the effectiveness of the proposed 3-D CD method.

This Chapter is organized as follows. Section 3.2 describes the proposed approach, by illustrating in detail all the different steps. The data used for the validation of the proposed method and the experimental results are presented and discussed in Section 3.3. Finally, Section 3.4 draws the conclusions and presents possible directions for future developments.

3.2 Proposed Hierarchical 3-D Change Detection Method

The aim of the proposed hierarchical CD approach is to accurately detect 3-D forest changes in bitemporal LiDAR data. After the pre-processing, first the method identifies the large changes (e.g., cut trees, new buildings) and then focuses the attention on the individual trees in order to detect the changes of the tree-canopies both in term of vertical and crown volume variation. Figure 3.1 shows the architecture of the proposed method, which is composed of 3 main parts: i) pre-processing (to make the two point clouds

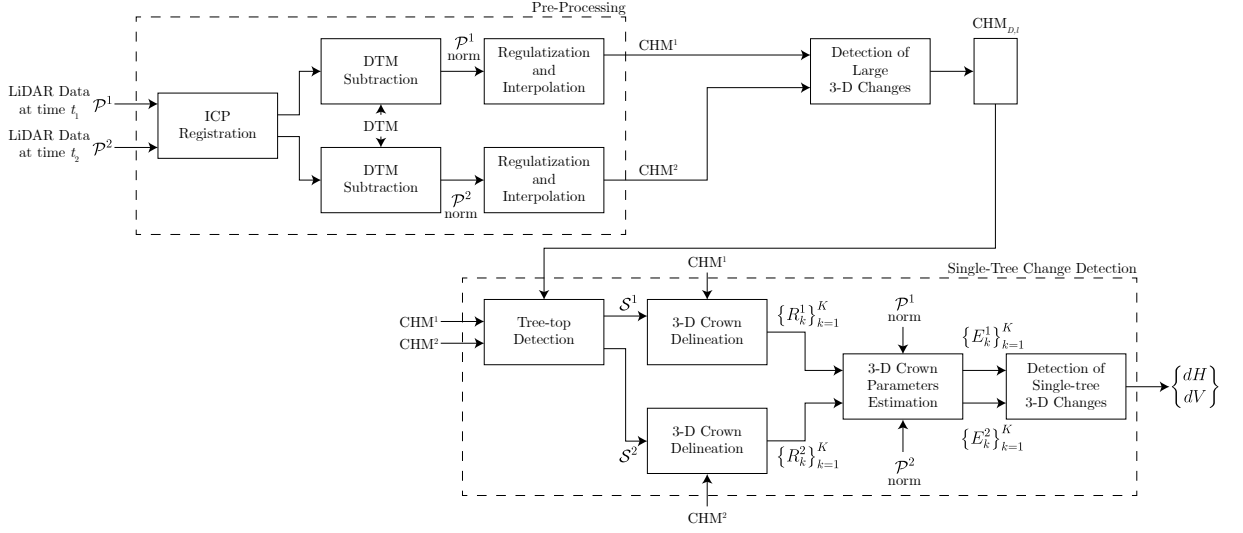


Figure 3.1: Architecture of the proposed method for the detection of large changes and single-tree changes.

comparable); ii) detection of large changes by comparing the two CHMs; iii) object-based detection of changes at the individual-tree level.

3.2.1 Problem definition

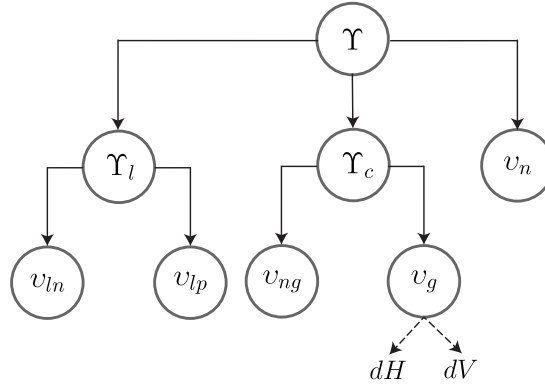


Figure 3.2: Hierarchical tree structure of the considered CD problem in forest areas. The represented classes are: Υ set of all considered classes; Υ_l large changes; v_{ln} large negative changes; v_{lp} large positive changes; Υ_c forest canopy cover present at both dates; v_{ng} trees with no growth; v_g trees with growth; v_n areas of no interest for forest change studies.

As mentioned in Section 3.1, forests are characterized by heterogeneous changes. In order to correctly identify all of them, it is necessary to properly define the CD problem. Let us assume to have a multitemporal LiDAR dataset consisting of two point clouds \mathcal{P}^1 and \mathcal{P}^2 (each composed by a set of points \mathbf{p} having coordinates x, y, z) acquired on the same forest area at different times t_1 and t_2 , respectively. Let $\Upsilon = \{\Upsilon_l, \Upsilon_c, v_n\}$ be the set of

all the considered classes where Υ_l is composed by the areas affected by large changes, Υ_c corresponds to the areas with forest canopy cover present at both dates and v_n represents all the areas that are of no interest for forest change studies, i.e., areas that do not have any canopy cover. Class $\Upsilon_l = \{v_{ln}, v_{lp}\}$ represents the classes of changes corresponding to large negative changes v_{ln} (e.g., cut trees, destroyed buildings) and large positive changes v_{lp} (e.g., new trees or buildings). Finally, $\Upsilon_c = \{v_{ng}, v_g\}$ represents the status of the areas covered by trees. We distinguish between trees with no growth (class v_{ng}) and trees that have changed between the two acquisitions (class v_g). Class v_g represents the growth of the trees both in terms of vertical variation dH and crown volume variation dV . It is worth noting that dH and dV are not mutually exclusive but they are usually correlated as the height variations contribute also to crown volume growth. Figure 3.2 shows the modeling of the hierarchical tree structure in the considered CD problem.

3.2.2 Pre-processing

The aim of the pre-processing is to make the two point clouds \mathcal{P}^1 and \mathcal{P}^2 comparable to accurately perform the bitemporal analysis. Accordingly, first we register the two data by applying the ICP algorithm, which aims at minimizing the Euclidean distance between the two 3-D point clouds. In this step we assume that a large portion of the forest did not change significantly between the two acquisitions. To this end, the algorithm iteratively searches for the rigid transformation $\mathbb{T} = [\mathbf{R}|\mathbf{t}]$ (defined by a rotation matrix \mathbf{R} and a translation vector \mathbf{t}) that best aligns the two LiDAR data. This is done by finding, at each iteration, a one-to-one correspondence between the points of \mathcal{P}^1 and the reference point cloud \mathcal{P}^2 thus generating a set of Q matched points $\{\mathbf{p}_q^1, \mathbf{p}_q^2\}_{q=1}^Q$. The algorithm searches for a transformation \mathbb{T} that minimizes the 3-D Euclidean distance between each point \mathbf{p}_q^2 and the corresponding transformed point $\mathbf{p}_q^{1,\mathbb{T}} = \mathbf{R}\mathbf{p}_q^1 - \mathbf{t}$, i.e.,:

$$d(\mathbf{p}_q^{1,\mathbb{T}}, \mathbf{p}_q^2) = \|\mathbf{p}_q^{1,\mathbb{T}} - \mathbf{p}_q^2\|. \quad (3.1)$$

Thus, the algorithm searches for the \mathbb{T} such that:

$$\mathbb{T} = \underset{\mathbb{T}'}{\operatorname{argmin}} \mathcal{E}(\mathbb{T}') = \underset{\mathbb{T}'}{\operatorname{argmin}} \sum_{q=1}^Q d(\mathbf{p}_q^{1,\mathbb{T}'}, \mathbf{p}_q^2). \quad (3.2)$$

The transformation \mathbb{T} is applied to the point cloud \mathcal{P}^1 (or \mathcal{P}^2 if the reference point cloud is \mathcal{P}^1). The algorithm then defines a new set of matched points between the reference and transformed point clouds and searches for a new transformation. These operations are repeated until $\mathcal{E}(\mathbb{T}')$ is smaller than a given threshold. It is worth noting that the ICP algorithm was originally developed for computer vision applications. Thus, it has been applied mostly to 3-D models having a very high point density. Moreover, a basic assumption of the original ICP is that the two 3-D models are almost identical (at least the portions that have to be aligned). Unfortunately, this is not the case for bitemporal airborne LiDAR data acquired on forest areas. Hence, the point-to-point approach of the ICP may lead to compute the rigid transformation using unreliable pairs of points. To mitigate the effects of this problem, we use only the first return of the two point

clouds, thus considering only the external surface of the tree-crowns, which is also the most informative. In addition, we discard a given percentage of pairs of points with the largest Euclidean distance. In particular, at each iteration we compute the set $D = \{d(\mathbf{p}_q^1, \mathbf{p}_q^2)\}_{q=1}^Q$ of the Euclidean distances between all the pairs of matched point (before computing the transformation) and we define a binary variable ψ_q as:

$$\psi_q = \begin{cases} 0 & d(\mathbf{p}_q^1, \mathbf{p}_q^2) > PCT(D) \\ 1 & d(\mathbf{p}_q^1, \mathbf{p}_q^2) \leq PCT(D) \end{cases}, \forall q = 1, \dots, Q, \quad (3.3)$$

where $PCT(D)$ is the PCT th percentile of D . The defined binary variable ψ_q can be used in $\mathcal{E}(\mathcal{T}')$ to discard pairs of point for which the pairwise Euclidean distance is large, i.e.,:

$$\mathcal{E}(\mathcal{T}') = \sum_{q=1}^Q \psi_q d(\mathbf{p}_q^{1, \mathcal{T}'}, \mathbf{p}_q^2). \quad (3.4)$$

These points cannot be used to reliably compute the transformation because they have a high probability of not representing the same portion of the tree or ground at the two dates. This may be due to outliers or large changes (e.g., a point representing a branch of a tree that has been cut between the two acquisitions should not be used in the ICP). Moreover, we decimate the two point clouds in order to apply the ICP on two data with the same density. Note that the ICP is applied to the two point clouds before subtracting the Digital Terrain Model (DTM). This allows us to use the information regarding the morphology of the terrain in the registration step. The transformation is applied also to the discarded points, which are considered in all the following steps.

After the registration phase, a DTM is subtracted from the two LiDAR data to obtain the relative height of the points with respect to the ground (i.e., normalized point clouds \mathcal{P}^1 and \mathcal{P}^2). Then, we regularize the two LiDAR data on a square grid. To this aim, we compute the value for each square as the elevation of the highest point which x, y coordinates fall inside the cell. Subsequently, to fill the gaps in the grid due to missing points, we apply an interpolation algorithm [179]. The selected interpolation algorithm is based on the concept of inpainting and the reconstruction of missing information. The algorithm reconstructs missing information caused by the irregular sampling of the LiDAR sensor allowing for a regularization on a higher resolution grid with respect to the case where no interpolation is applied. However, note that the resolution can not be increased at will since if the number of gaps is too large, the reconstruction leads to poor results and artifacts. Finally, the regularized point clouds can be easily converted into images, thus obtaining the two Canopy Height Models CHM^1 and CHM^2 .

3.2.3 Detection of Large Changes

According to the hierarchical approach, first we need to automatically identify the areas affected by large positive v_{lp} and negative v_{ln} changes. To this end, we compute the difference image CHM_D by subtracting CHM^1 and CHM^2 [71, 74, 75] as follows:

$$\text{CHM}_D(x, y) = \text{CHM}^2(x, y) - \text{CHM}^1(x, y). \quad (3.5)$$

As we are searching for large changes, to identify only the areas in which there is a substantial height variation, two thresholds T_{lp} and T_{ln} are applied to CHM_D , in order to obtain two binary maps $\text{CHM}_{D,lp}(x, y)$ and $\text{CHM}_{D,ln}(x, y)$ according to:

$$\begin{aligned} \text{CHM}_{D,lp}(x, y) &= \begin{cases} 1 & \text{CHM}_D(x, y) \geq T_{lp} \\ 0 & \text{otherwise} \end{cases} \\ \text{CHM}_{D,ln}(x, y) &= \begin{cases} 1 & \text{CHM}_D(x, y) \leq -T_{ln} \\ 0 & \text{otherwise} \end{cases} \end{aligned} \quad (3.6)$$

where the pixels set to 1 identify the areas affected by large changes (positive changes v_{lp} for $\text{CHM}_{D,lp}(x, y)$ and negative changes v_{ln} for $\text{CHM}_{D,ln}(x, y)$). We use two thresholds (considering $T_{lp} < T_{ln}$) since the magnitude of the deforestation changes can be much larger with respect to the one of the forestation changes. Indeed, whereas the cut of a tree may correspond to a variation of more than 30 m, the growth of a new tree corresponds to much lower absolute values in $\text{CHM}_D(x, y)$, which depend also on the elapsed time between the two acquisitions. It is worth noting that the choice of two different threshold values does not affect the detection of other large changes such as the construction or destruction of buildings since their magnitude is large both for positive and negative changes. Then we perform a series of morphological operations on both binary maps starting with an erosion filter based on a circular structuring element. This operation allows us to remove most of the noise, thus identifying either the cut or new tree-canopies and other large changes. Then, all the regions with area lower than a given threshold T_A are removed and finally a dilation filter (having the same structuring element used in the previous morphological operation) is applied to the resulting binary image. It is worth noting that the size of the structuring element and the threshold area T_A should be chosen according to the spatial resolution of the CHMs. The obtained binary maps $\text{CHM}_{D,ln}(x, y)$ and $\text{CHM}_{D,lp}(x, y)$ are then merged in a single map $\text{CHM}_{D,i}(x, y)$ which is used to drive the detection of the single-tree changes, i.e., all the operations of the second part of the method are applied only on to the areas that are not affected by large changes. At this point of the analysis, all the areas not affected by large changes may belong to areas not of interest for forest studies (i.e., v_n class) or to areas with the presence of canopy cover at both dates (i.e., Υ_c class).

3.2.4 Single-Tree Change Detection

In the last step of the proposed hierarchical approach, we address the difficult task of detecting the single-tree changes and the related attributes dH and dV . This requires to accurately detect and delineate the tree-canopies at the two dates since every error in the crown detection and delineation step will affect the single-tree CD results. The individual tree-crowns are detected and delineated in the CHMs and then the bitemporal analysis is performed directly in the point cloud space. This condition allows us to exploit the full information content of the point clouds to improve the detection of the single-tree changes. To overcome the problem related to the CD in bitemporal LiDAR data (i.e., point-to-point comparison is not feasible), we focus the attention on the whole tree structure by means of an object-based approach based on the geometry of the tree-canopy.

Tree-top Detection

To detect the trees at the two dates, first we apply median and Gaussian filtering to the two CHMs. Then, by applying a Level Set Method (LSM) [178] to CHM^1 and CHM^2 , we separately identify the positions of the tree-tops, hereafter referred also as seeds. Level Set Methods are typically used to analyze surfaces and their topology without the need of a parametric model. Therefore, they are suitable for the analysis of the CHM which can be seen as a surface with several local maxima each representing, in an ideal case, a tree-top (for conifers forests). The method slices the surface at several heights (bottom up) producing a binary image for each sliced plane. By comparing each binary image with the upper one and searching for changes in the number of connected binary regions, the local maxima are detected. Compared to other techniques such as the Local Maxima Filtering (LMF) [180], the used LSM does not require the tuning of parameters to perform the detection. In contrast, the LMF is based on a sliding window where the window size affects the detection results and thus have to be tuned accordingly. The LSM produces the set of candidate tree-tops $\{\mathbf{s}_{k^1}^1\}_{k^1=1}^{K^1}$ at time t_1 and the set of candidate tree-tops $\{\mathbf{s}_{k^2}^2\}_{k^2=1}^{K^2}$ at time t_2 , where $\mathbf{s}_{k^1}^1$ and $\mathbf{s}_{k^2}^2$ represent the (x, y) positions of the tree-tops at the two dates. According to the availability of the bitemporal dataset, we can employ in a synergistic way the two LiDAR data to improve the detection result. Thus, we compare the set of candidate tree-tops $\{\mathbf{s}_{k^1}^1\}_{k^1=1}^{K^1}$ with $\{\mathbf{s}_{k^2}^2\}_{k^2=1}^{K^2}$ to match the trees present at both dates. The position of the same tree-top may be different at the two dates due to natural causes or residual registration error (which we assume to be small due to registration step applied in the pre-processing phase). Thus we can perform a final object-based registration by matching the two sets of seeds associating to each candidate tree-top $\mathbf{s}_{k^1}^1$ the nearest seed $\mathbf{s}_{k^2}^2$ according to the Euclidean distance:

$$\mathbf{s}_{k^2}^2 : k^2 = \underset{k^2 \in \{1, \dots, K^2\}}{\operatorname{argmin}} \left\| \mathbf{s}_{k^2}^2 - \mathbf{s}_{k^1}^1 \right\|. \quad (3.7)$$

To avoid false matching, we discard all the matched pairs having an Euclidean distance greater than a given threshold T_s . Note that the matching is performed considering only the tree-tops locations, without taking into account the tree-top heights, which change due to the vertical growth of the trees. For those candidate tree-tops detected only in one acquisition, we improve the detection accuracy by using the information provided by the other acquisition. In particular, we aim to distinguish between false alarms (i.e., false tree-tops detected due to noise at one date) or true tree-tops correctly identified only at one date. To this end, we compute a rough estimate of the crown width by analyzing the behavior of the CHM around each of these seeds by means of a directional analysis. If the estimated crown width is greater than 1 m at least at one of the two dates, we recover the tree-top, otherwise we definitely discard it. This operation allows us to use in a synergistic way the bitemporal information to reduce the number of false alarms without increasing the number of missed alarms. In this step we compute a rough estimate of the crown radius. However, to perform an accurate CD a more precise approach to the crown delineation is required. The results of these operations are two set of tree-tops $\mathcal{S}^1 = \{\mathbf{s}_k^1\}_{k=1}^K$ and $\mathcal{S}^2 = \{\mathbf{s}_k^2\}_{k=1}^K$ where K is the number of tree-tops detected at both dates.

Tree Crown Delineation

To fully characterize the tree-canopies, we perform the crown delineation separately in CHM^1 and CHM^2 around each \mathbf{s}_k^t , ($t = 1, 2$). In the CD, segmentation errors may lead to the detection of changes which are not related to the growth of the trees. Thus, we aim to perform a conservative segmentation to reduce the number of errors (i.e., portions of crowns that are included in the segmentation region of other tree-canopies). For this reason, in the first phase of the segmentation we delineate a preliminary bounding box around each tree-top. Second, we refine the segmentation result by accurately delineating the crown boundaries. Let us focus on a generic k th tree and on CHM^1 , (i.e., time t_1). Note that all the following operations are performed also at time t_2 considering \mathcal{S}^2 and CHM^2 . After a median filtering of the CHM, the J neighbouring tree-tops of \mathbf{s}_k^1 within a maximum radius T_r are detected, i.e., we select a subset of tree-tops $\{\mathbf{s}_j^1\}_{j=1}^J \in \mathcal{S}^1$ such that:

$$\mathbf{s}_j^1 \in \mathcal{S}^1 : \|\mathbf{s}_k^1 - \mathbf{s}_j^1\| \leq T_r. \quad (3.8)$$

If no trees are found around \mathbf{s}_k^1 (i.e., the tree-can be considered isolated), the method moves directly to the second phase of the segmentation. For each $\{\mathbf{s}_j^1\}_{j=1}^J \in \mathcal{S}^1$, we define the 2-D line $\ell_{k,j}^1$ connecting \mathbf{s}_k^1 and \mathbf{s}_j^1 and the corresponding values of CHM^1 $\gamma_{k,j}^1$. We search for the absolute minimum of $\gamma_{k,j}^1$ and the corresponding x, y position in $\ell_{k,j}^1$. The 2-D line perpendicular to $\ell_{k,j}^1$ passing through the x, y point corresponding to the minimum of $\gamma_{k,j}^1$ can be considered as a conservative crown boundary. By repeating this operation for all $\{\mathbf{s}_j^1\}_{j=1}^J$ we generate the preliminary bounding box of the k th tree. The bounding box allows us to use the contextual information of the tree and its neighbours in the segmentation. Figure 3.3 illustrates the preliminary segmentation of a tree surrounded by three neighbours.

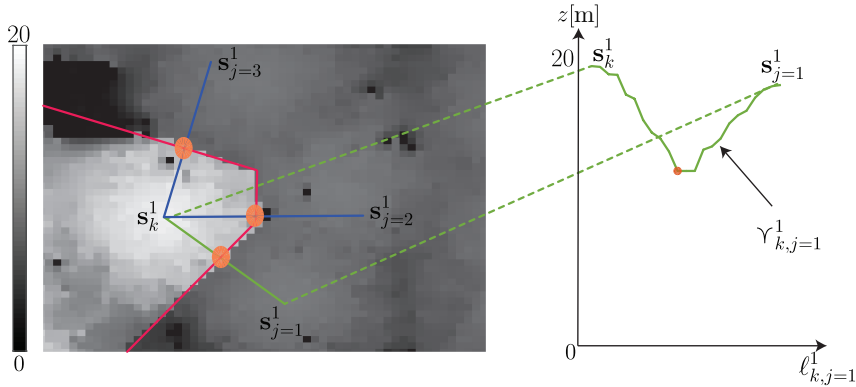


Figure 3.3: Example of the first phase of the segmentation (at time t_1) of tree \mathbf{s}_k^1 surrounded by three trees $\{\mathbf{s}_j^1\}_{j=1}^3$. In blue the lines $\ell_{k,j}^1$ with in green $\gamma_{k,j=1}^1$. The orange dots represent the points at which the considered tree intersects with its neighbours. The portion of the CHM^1 shows the result of the partial segmentation as the bright area (delineated by the red bounding box).

In the second phase of the segmentation we delineate the crown by analyzing the values

of the CHM around the tree-top position \mathbf{s}_k^1 . To this end, we apply a crown delineation algorithm similar to those proposed in [10, 56]. In greater detail, we analyze the profile of the canopy in several directions starting from the position of the tree-top. For each direction, we search for the first local minimum and its position is considered as a crown boundary reference point. It is worth noting that, to increase the reliability of the segmentation result, we consider only the crown boundary reference points that are inside the conservative bounding box delineated in the previous phase of the segmentation. Indeed, in some cases the first local minimum may be found further away than the true crown boundary point (e.g., due to the interpolation artifacts in the regularization step). The use of the bounding box allows us to reduce the probability of such errors by discarding large portions of the CHM that do not belong to the considered canopy. Finally, to define the final polygon of the segmented region, we compute the 2-D convex hull of the obtained set of reference crown boundary points. This is done because it is reasonable to approximate the crown perimeter as a 2-D convex polygon and in this way we discard the points that are inside the canopy perimeter but are wrongly detected as crown boundary. The outcomes of the segmentation are two sets of regions $\{R_k^1\}_{k=1}^K$ and $\{R_k^2\}_{k=1}^K$, where R_k^1 and R_k^2 delineate the crown of the k th tree in CHM^1 and CHM^2 , respectively. It is worth noting that all the areas that are not included in $\{R_k^1\}_{k=1}^K$ and $\{R_k^2\}_{k=1}^K$, and are not affected by large changes Υ_l , belong to the class v_n .

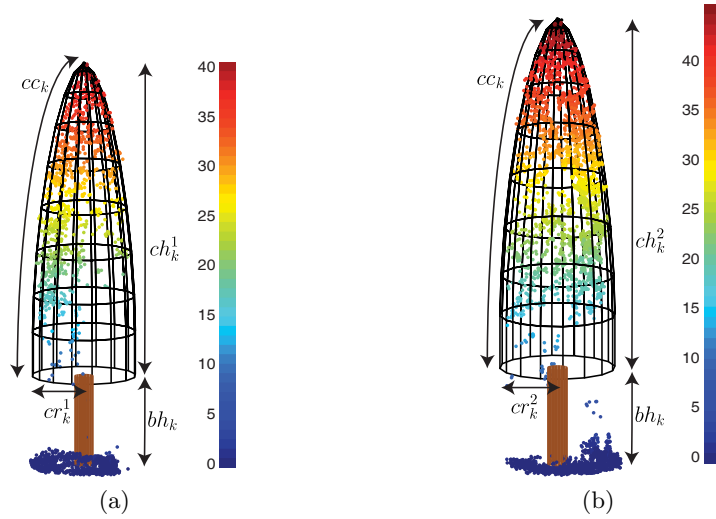


Figure 3.4: 3-D models fitted on the segmented point clouds at the two dates for a generic tree k : (a) C_k^1 and E_k^1 , (b) C_k^2 and E_k^2

Single-Tree Growth Analysis

In order to exploit the full information content of the LiDAR data we perform the detection of the single-tree changes directly in the point cloud domain. To this end, we transfer the sets of regions $\{R_k^1\}_{k=1}^K$ and $\{R_k^2\}_{k=1}^K$ to the 3-D point cloud space, generating two sets of segmented point clouds $\{C_k^1\}_{k=1}^K$ and $\{C_k^2\}_{k=1}^K$ where C_k^1 and C_k^2 represent the crown of the

k th tree at times t_1 and t_2 , respectively. Since it is not feasible to compare the two point clouds C_k^1 and C_k^2 using a point-to-point approach, we reconstruct the external surface of the tree-canopy at the two dates using an object-based approach defined by a parametric modeling. The 3-D model can be used to compute an estimate of the crown volume which is less affected by outliers with respects to other methods such as convex hull or alpha shape. Using a 3-D model allows us to address also the problem related to the irregular sampling of the LiDAR sensor which for single-trees become significant especially when the pulse density is low. Indeed, this increases the probability of having portions of the canopy not hit by the laser pulses. The model allows us to reconstruct the missing portion of the canopy using as additional information the expected shape for the crown. It is worth noting that any model can be used in principle with the proposed technique but here we focus on conifer trees and thus a 3-D ellipsoid is suitable to accurately model the tree-canopy [181–183]. The selection of this model has been done considering the conical shape of the average conifer. Most importantly, conifers are typically highly symmetric shapes showing a similar profile in every direction. This relevant characteristics is exploited when using the 3-D model since it allows for the reconstruction of the portions of the canopy that have not been hit by the LiDAR sensor. The mathematical model of the generic k th tree is defined by four parameters that control the shape of the ellipsoid: i) the tree-top height zh located in (xh, yh) , ii) the canopy height ch , iii) the crown radius cr , iv) the crown curvature cc . The 3-D model is defined as follows:

$$\frac{(z + ch - zh)^{cc}}{ch^{cc}} + \frac{[(x - xh)^2 + (y - yh)^2]^{cc/2}}{cr^{cc}} = 1, \quad zh - ch < z < zh. \quad (3.9)$$

Figure 3.4 shows an example of the 3-D ellipsoids with the described parameters. To define the 3-D ellipsoid for both point clouds C_k^1 and C_k^2 , we need to estimate the sets of parameters $(zh_k^1, ch_k^1, cr_k^1, cc_k^1)$ and $(zh_k^2, ch_k^2, cr_k^2, cc_k^2)$. Due to the conservative crown segmentation, the number of outliers in the segmented point clouds C_k^1 and C_k^2 is reduced, thus making the parameters estimation process more reliable. Since we are in a multi-temporal framework, we perform the estimation by fusing the information of both dates to improve the accuracy of the estimates at single-date. To this end, we define a set of rules based on natural physical constraints. First, we estimate the tree-top heights zh_k^1 and zh_k^2 as the highest elevation values of the two point clouds C_k^1 and C_k^2 , respectively. It is very unlikely that tree-top height decreases over time except some cases in which the highest part of the tree is damaged (e.g., due to severe weather conditions). Thus, we assume that $zh_k^1 \leq zh_k^2$ and if this condition is not satisfied we set $zh_k^1 = zh_k^2$.

Then, we estimate the crown base heights bh_k^1 and bh_k^2 (i.e., heights of the lowest branch) defined as $bh_k^t = zh_k^t - ch_k^t$, ($t = 1, 2$). The estimates are obtained by analyzing the vertical profiles of the segmented point clouds. If the two point clouds have been acquired few years apart, we can assume that the base height does not vary significantly with time (i.e., $bh_k^1 = bh_k^2 = bh_k$). Indeed, the base height variation (i.e., rise of the lowest branch of the tree) is due to the death of the lowest branches of the canopy [184] and thus it does not change rapidly. Accordingly, we can define a single base height as $bh_k = \min\{bh_k^1, bh_k^2\}$. In this way we improve the estimation of the base height by fusing the information of the bitemporal LiDAR data. Indeed, the laser may penetrate more the lower portion of the canopy at one of the two dates with respect to the other due to

a higher pulse density thus allowing for a more accurate estimation. By fusing the two estimates we use the higher density data to improve the estimation in the other one. The two crown heights can be computed as $ch_k^t = zh_k^t - bh_k$, ($t = 1, 2$). It is worth noting that, if the time difference between the acquisitions of the two LiDAR data is large, this assumption is not valid anymore and the base heights have to be estimated separately at the two dates.

To estimate the crown radius, for each segmented tree we select all the points belonging to the canopy (i.e., points for which $z > bh_k$) and then we compute the area Ξ_k^t , ($t = 1, 2$) at both dates of the 2-D convex hull computed using the x, y coordinates of the selected points. Finally, we calculate the crown radius as $cr_k^t = \sqrt{\Xi_k^t/\pi}$, ($t = 1, 2$). Also in this case we use the multitemporal information to improve the estimation accuracy. To this end, we consider the constraint on the radius $cr_k^1 \leq cr_k^2$. In particular, for those crowns where $cr_k^1 > cr_k^2$ we set $cr_k^1 = cr_k^2$ since it is plausible to assume that the crown radius does not decrease in time.

The crown curvature is estimated by detecting the value that minimizes a residual distance metric between the 3-D ellipsoid and the points belonging to the external surface of the segmented point cloud. Similarly to the base height, it is reasonable to assume that the crown curvature does not change significantly in time (i.e., $cc_k^1 = cc_k^2 = cc_k$). Thus, the fitting of the 3-D models is done on the segmented point cloud with the highest number of points. If we consider the crown at time t_1 as the one with larger number of points, we can define the residual distance metric of a single x_i, y_i, z_i point for a given cc_k' as:

$$r_i(cc_k') = \frac{(z_i + ch_k^1 - zh_k^1)^{cc_k'}}{ch_k^{1cc_k'}} + \frac{\left[(x_i - xh_k^1)^2 + (y_i - yh_k^1)^2 \right]^{cc_k'/2}}{cr_k^{1cc_k'}} - 1. \quad (3.10)$$

Thus, the overall residual distance metric for can be defined as:

$$r(cc_k') = \sum_{i=1}^{\#C_k^1} r_i(cc_k')^2 \quad (3.11)$$

where $\#C_k^1$ is the number of points in C_k^1 . The estimate of cc_k is selected according to:

$$cc_k = \underset{cc_k'}{\operatorname{argmin}} r(cc_k'). \quad (3.12)$$

The aforementioned operations allow us to simplify the detection of the 3-D changes at the individual tree level (in particular the detection of the crown volume growth dV) by characterizing the canopy structure using a 3-D ellipsoid regardless of the pulse density. For each k th tree, we have the following variables:

- tree-top heights zh_k^1 and zh_k^2 ;
- two 3-D ellipsoids E_k^1 and E_k^2 (defined using $(zh_k^t, ch_k^t, cr_k^t, cc_k^t)$, ($t = 1, 2$)) representing the canopy structure at the two dates.

The vertical growth of the considered tree can be computed as $dH_k = zh_k^2 - zh_k^1$. In order to compute the crown volume growth, first we compute the volume of the considered tree at the two dates according to:

$$V(E_k^t) = \iint_{\sqrt{x^2+y^2} \leq cr_k^t} \left(ch_k^{t \ cc_k} + \frac{(x^2 + y^2)^{cc_k/2}}{cr_k^{t \ cc_k}} ch_k^{t \ cc_k} \right)^{1/cc_k} - ch_k^t + zh_k^t \, dx \, dy, \quad (t = 1, 2). \quad (3.13)$$

Then, the crown volume growth is estimated as:

$$dV_k = V(E_k^2) - V(E_k^1). \quad (3.14)$$

It is now possible to distinguish between trees with no growth (class v_{ng}) and trees with growth (class v_g) by applying two thresholds to dH_k and dV_k , i.e.:

$$\mathbf{s}_k \in \begin{cases} v_{ng} & dH_k < T_{dH} \wedge dV_k < T_{dV} \\ v_g & dH_k \geq T_{dH} \vee dV_k \geq T_{dV} \end{cases}, \quad (3.15)$$

where \wedge is the logical and and \vee is the logical or. We used these thresholds to avoid the effects of small differences that may depend on either systematic acquisition errors of LiDAR or the complex forest scenario. Thus, the thresholds allow us to correctly identify the trees that show a significant growth. From the definition of dH_k and dV_k , one can see that these two attributes are not mutually exclusive since both zh_k^t , ($t = 1, 2$) and E_k^t , ($t = 1, 2$) are dependent from ch_k^t , ($t = 1, 2$).

3.3 Experimental Results

3.3.1 Experimental Setup

To assess the effectiveness of the proposed method, we performed the CD analysis on two forest areas located in the southern Italian Alps in the Trento province. The first area is located in Baselga di Piné, Trentino (central point coordinates $46^\circ 10' 79,18''$ N, $11^\circ 22' 66,13''$ E) and extends approximately 25 ha. The terrain is characterized by a complex morphology with an altitude ranging from 850 m to 1000 m. The species composition of the forest is mainly *Larix decidua* (European Larch) and *Picea abies* (Norway Spruce). The LiDAR data were acquired in 2010 and 2014 by an ALTM 3100EA sensor with a maximum pulse density of 10 pulses/m² and 15 pulses/m², respectively, and four returns registered for each pulse. We selected two 70 m \times 70 m areas (see Figures 3.5a,3.5e and 3.5b,3.5f) for our experiments.

The second study area is an old-growth coniferous forest located in Pellizzano, Trentino (central point coordinates $46^\circ 17' 31,00''$ N, $10^\circ 45' 56,49''$ E). The size of the area is 3200 ha with an altitude ranging from 900 to 2800 m and a complex terrain morphology. The species composition is similar to the one of the first test forest. The LiDAR data were acquired in 2012 by a Riegl LMS-Q680i sensor with a maximum pulse density of

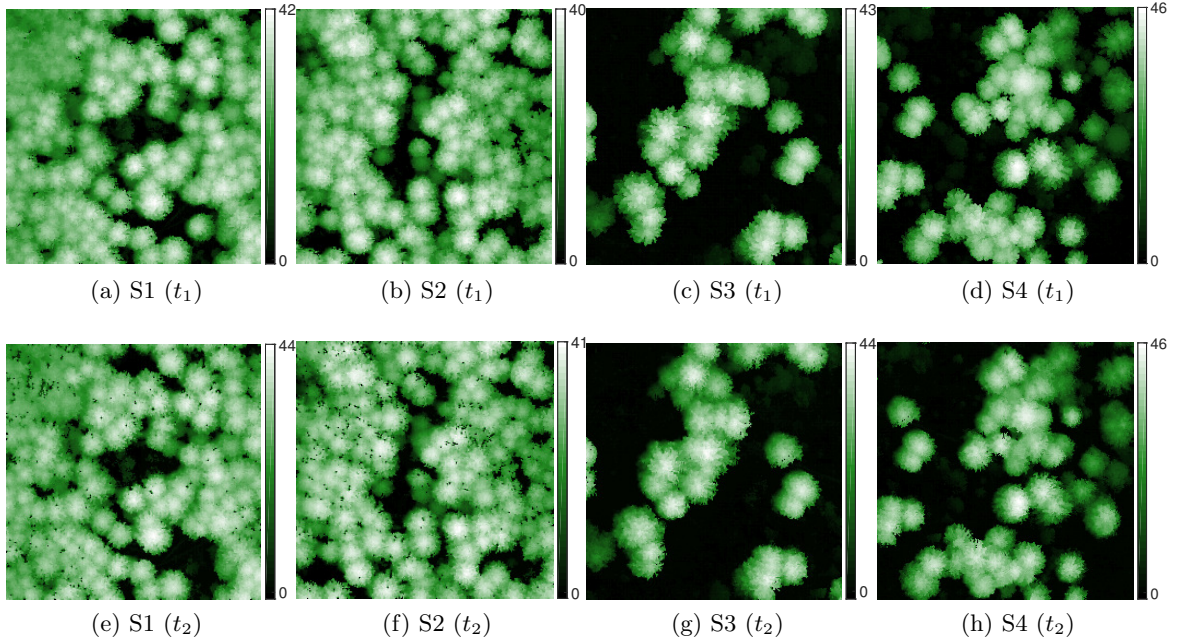


Figure 3.5: CHMs of the 4 stand plots at times t_1 and t_2 . The considered forest stands are characterized by different forest densities and terrain morphologies. The rasterization has been carried out at 0.3 m resolution.

50 pulses/m² and in 2015 by an ALTM 3100EA sensor with a maximum pulse density of 15 pulses/m². In both the acquisitions four returns were registered for each pulse. We selected a 70 m × 70 m area (Figures 3.5c,3.5g) and a 80 m × 80 m area (Figures 3.5d,3.5h) for our experiments.

Table 3.1 shows the parameters of the proposed method used for all the considered LiDAR point clouds. To generate the CHMs, we considered a spatial resolution of 0.3 m to accurately represents the forest structure. Accordingly, the radius of the structuring element (with the shape of a disk) was set to 3 and the large changes area threshold T_A was set equal to 100 pixels (i.e., minimum large changes area 9 m²) in order to avoid the detection of the crown widths variations as large changes. For the detection of the tree-tops a small 3 × 3 median kernel filter and a 4 × 4 Gaussian kernel filter were considered to reduce the missed detection of trees present in the scene, even though this increases the detection of false trees. However, due to the synergistic use of the of bitemporal data, the number of false trees is reduced by comparing the two sets of tree-tops. The distance threshold T_s for the matching was set to 1.5 m in order to be robust to the presence of residual registration errors or variations of the tree-top position due to natural causes.

For the segmentation we selected a larger 5 × 5 kernel filter to avoid the detection of local minima caused by errors in the regularization step. The preliminary segmentation is carried out analyzing a maximum of $J = 4$ neighbours trees (selected according to the typical structure of the forest) in a range of $T_r = 10$ m from the considered tree. The minimum canopy height growth T_{dH} and minimum crown volume growth T_{dV} were set to 0.2 m and 10 m³, respectively, considering the time interval between the two acquisitions.

Table 3.1: Parameters values defined for the proposed method.

Parameter	Value
Percentile PCT	70 th
Resolution of CHM and DSM	0.3 m
Height threshold (v_{lp}) T_{lp}	3 m
Height threshold (v_{ln}) T_{ln}	5 m
Structuring element radius	3
Area threshold T_A	100
Median kernel size (tree detection)	3×3
Gaussian kernel size (tree detection)	4×4
Gaussian filter standard deviation	4
Matching threshold T_s	1.5 m
Median kernel size (crown delineation)	5×5
Maximum number of neighbours trees J	4
Search Radius for neighbours trees T_r	10 m
Minimum height growth T_{dH}	0.2 m
Minimum crown volume growth T_{dV}	10 m ³

Note that we used the same parameters for all the considered LiDAR data even if they are characterized by very different pulse densities and represent forests with very diverse characteristics. This choice of parameters can be considered general for alpine forests. It is worth noting that a minimum pulse density of 5 pulses/m² is required in order carry out an accurate CD.

The first step of the method is the ICP registration. Since the data were already registered, to validate the ICP algorithm with the used settings we simulated different registration errors and analyzed the registration results using Ground Control Points (GCPs). In greater detail, for each stand we tested shift errors ranging from 0 to 10 m. For each shift we selected two partially overlapping portions of the data (one at time t_1 and one at time t_2) with the same size and we shifted data at time t_2 in such a way that they completely overlap. To test also the robustness to rotation errors we added different amounts of rotation (from 0° to 5°). We validated the results both from a qualitative (by visual analysis of the registered point cloud and the reference data) and quantitative (using GCPs) point of view. We selected as GCPs the position of the tree-tops at the two dates and we manually matched the tree-top at time t_1 with the tree-tops at time t_2 . For each test we applied the corresponding shift and rotation to the GCPs and after the ICP step (applied to the shifted point cloud) we applied the resulting rigid transformation on the GCPs of time t_2 . Finally, we computed the average Euclidean distance between the tree-tops at time t_1 and the registered tree-tops at time t_2 .

The results of the detection of large changes have been validated using reference maps derived by photo-interpretation of the two CHMs and CHM_D. The reference maps were then compared with the ones automatically generated by the proposed method. The validation of the tree detection has been carried out using a map of trees identified by a visual analysis. The trees have been detected manually by first selecting the local maxima

in the CHM and then by analyzing directly the point cloud to remove false trees and recover missed trees that do not have a corresponding local maximum in the CHM. Each tree detected at both dates has been manually delineated by analyzing both the CHM and the point cloud. Using this set of reference tree-tops, the obtained results were evaluated in terms of Commission Errors (CE), Omission Errors (OE) and Overall Accuracy (OA) considering only the trees present at both dates. Then, we selected 72 trees in stand S1, 80 trees in stand S2, 16 trees in stand S3 and 36 trees in stand S4 for the manual estimation of the crown parameters. A small number of trees were not considered for the validation since, even when manually delineated, the crown structure was not clearly represented by the segmented point cloud. In particular, we discarded crowns on the border of the stand, crowns with few points and trees partially covered by dominant trees. We analyzed the manually segmented point cloud of each tree, separately at both dates, to estimate the crown radius and crown base height. The crown radius has been estimated considering only the (x, y) information of the LiDAR points computing the crown radius in multiple directions, starting from the crown center, to select the most reasonable estimate. In particular, we discarded outliers such as a too short radius (due to missing points of the crown) and then we computed the mean of the remaining radii. The base height has been estimated considering both the canopy density profile and the projection of the LiDAR points on a 2-D plane perpendicular to the ground in order to detect the lowest branch of the tree. Note that we consider as lowest branch of the tree not the lowest point but the lowest group of points representing a branch. The segmentation results have been validated qualitatively by visual analysis of the segmented point clouds comparing the automatic result with the manual one. Moreover, a quantitative evaluation was carried out comparing the manually estimated radius with the one estimated automatically. We computed the Mean Absolute Error (MAE), the Root Mean Square Error (RMSE), the Normalized Mean Square Error (NRMSE) and the coefficient of determination (R^2) for both the radius and base height estimations. Finally, since the single-date reference data could not be used to validate the change analysis, the single-tree changes results were evaluated by a team of experts of the regional forest service. In particular, the forest service team compared the change results with the characteristic of the analyzed forest to understand if the amount of detected growth is compatible with the stand. For each stand, the forest service considered the age and height of the trees to provide an estimate of growth both in terms of vertical and crown volume growth. These estimates were then compared with the stand-wise average of the values of growth estimated at the single-tree level.

3.3.2 Results

Registration

Figures 3.6 and 3.7 show the results obtained in the ICP step in terms of residual mean Euclidean distance on the GCPs at times t_1 and t_2 . In the case of no artificial rotation, Figure 3.6a shows that the proposed ICP procedure can accurately register data up to a shift of 4 m for all the stands and up to 7 m for the stand S4. On the contrary, the standard ICP procedure (Figure 3.6b) is robust to shift up to 3 m. At a shift of 4

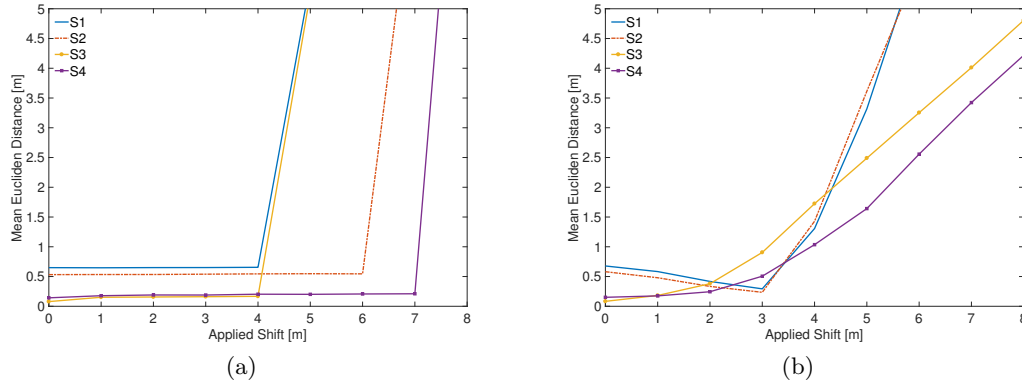


Figure 3.6: Plots showing the residual registration error (on the GCPs) versus the amount of artificially introduced shift. The x-axis represents the applied shift while the y-axis corresponds to the residual error: (a) proposed ICP procedure; (b) standard ICP procedure.

in the residual error becomes significant for the stand S3. Figure 3.7 shows the results with different amounts of shift and an applied rotation ranging from 0° to 5° degrees. Figures 3.7a, 3.7c, 3.7e, 3.7g shows that the proposed ICP procedure is robust also to rotation errors since it reaches almost equal results with different combination of shift and rotation. Figures 3.7b, 3.7d, 3.7f, 3.7h point out that the standard ICP procedure shows stable results at different rotations but is more sensible to shift errors.

Detection of Large Changes

Let us focus the attention on the detection of large changes $\Upsilon_l = \{v_{ln}, v_{lp}\}$. Figure 3.8 shows a qualitative example of how morphological operators remove the noise from the CD map. The erosion filter and the threshold on the area of the large changes allow us both to discard the false alarms due to noise in the CHMs and to remove the pixels representing the expansion of the tree-crowns. These qualitative results are confirmed by the quantitative evaluation given in Table 3.2. In the considered forest areas, only deforestation changes (i.e., large negative changes v_{ln}) are present. The three confusion matrices show good detection accuracy with a small number of missed and false alarms. Note that no large changes were present in stand S2 and the proposed technique did not detect any false alarm.

Single-Tree Change Detection

After having identified the large changes, we focus the attention on the changes at the individual tree level. Table 3.3 presents the numerical results of the tree-top detection. By matching the two set of tree-tops, we reduced the CE rate from 4.9%-5.5% to 1.7% without affecting the OE rate. This shows that the method in most of the cases correctly distinguishes between trees that have been detected only at one date and CE. The CE that are not discarded during the matching are mostly due to steeply inclined tree branches that generate a peak in the CHM. The analysis of the OE rate shows that there is almost

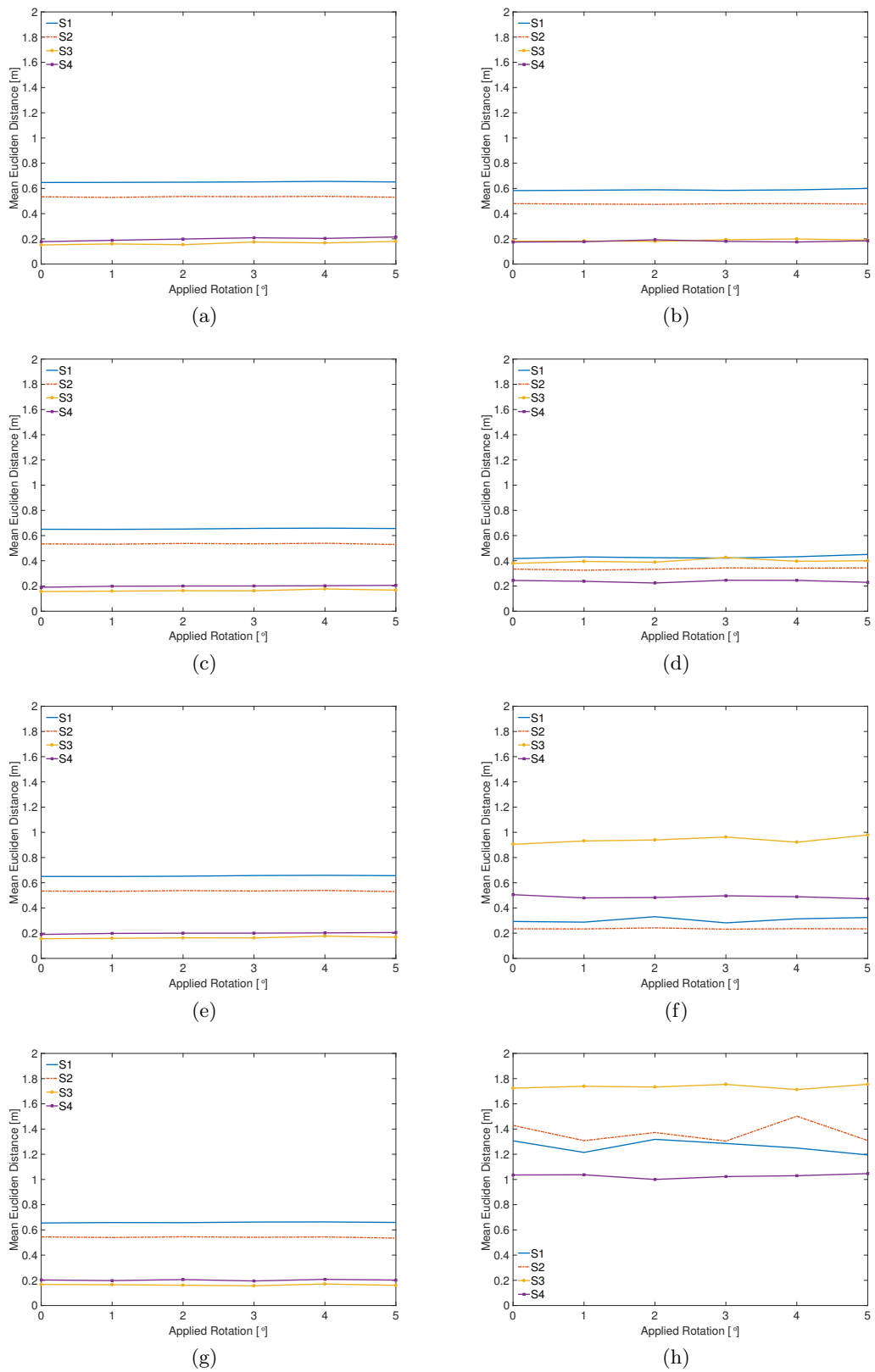


Figure 3.7: Plots showing the residual registration error (on the GCPs) versus the amount of artificially introduced rotation for different shifts: (a-c-e-g) proposed ICP procedure with an applied shift of 1, 2, 3, 4 m, respectively; (b-d-f-h) standard ICP procedure with an applied shift of 1, 2, 3, 4 m, respectively.

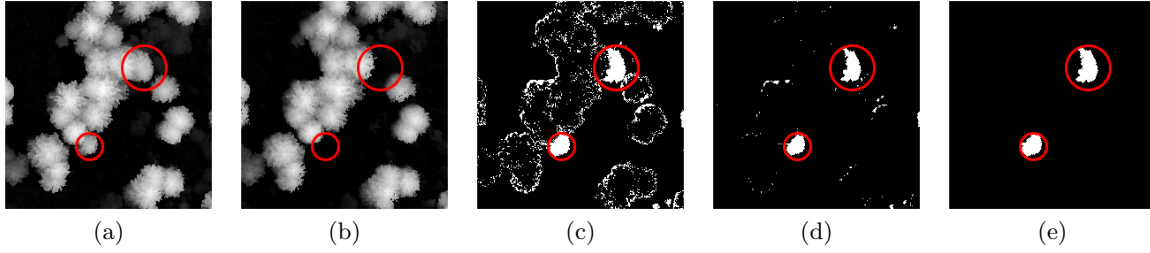


Figure 3.8: Example of the detection of large changes for stand S3 (the red circles highlight the large changes identified by photo-interpretation): (a)-(b)CHMs at times t_1 and t_2 ; (c) binary difference image of the two CHMs after the thresholding operation; (d) binary map after the erosion morphological filter; (e) final result after the elimination of small patches and the dilation filter.

Table 3.2: Confusion matrices of the detection (Det) of large negative changes v_{ln} in terms of classified pixels in the CHM for stands: (a) S1, (b) S3 and (c) S4.

(a)				(b)			
		Reference				Reference	
		$\{v_n, \Upsilon_c\}$	v_{ln}			$\{v_n, \Upsilon_c\}$	v_{ln}
Det	$\{v_n, \Upsilon_c\}$	54172	34	Det	$\{v_n, \Upsilon_c\}$	53877	56
	v_{ln}	19	531		v_{ln}	98	959

(c)			
		Reference	
		$\{v_n, \Upsilon_c\}$	v_{ln}
Det	$\{v_n, \Upsilon_c\}$	69547	103
	v_{ln}	186	1453

Table 3.3: Omission Errors (OE), Commission Errors (CE) and Overall Accuracy (OA) obtained by the single-date detection and by the proposed method for the tree-top detection in the four stands.

Approach	Trees	OE		CE		OA
	#	#	%	#	%	%
Single-date t_1	344	7	2	19	5.5	92.8
Single-date t_2	344	9	2.6	17	4.9	92.8
Matching	344	8	2.3	6	1.7	96

no improvement after the matching. This is due to two main reasons : i) the tree has not been identified at both dates and thus it is not possible to exploit the bitemporal information to recover it, ii) the tree-top is covered by dominant trees.

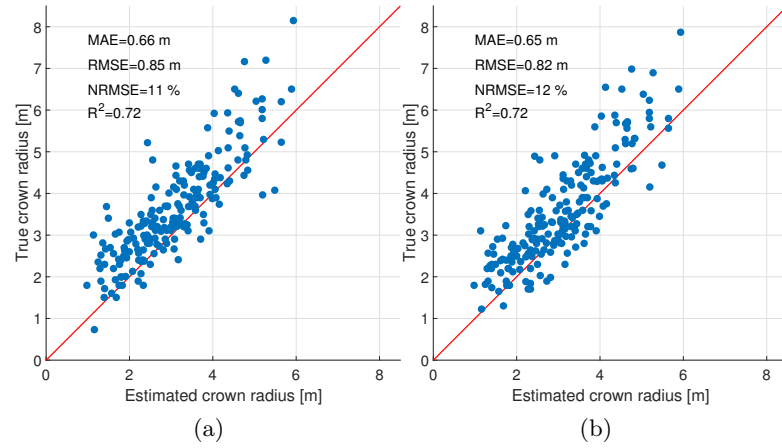


Figure 3.9: True versus estimated crown radius (cr) for all the stands at the two dates: (a) time t_1 , (b) time t_2 .

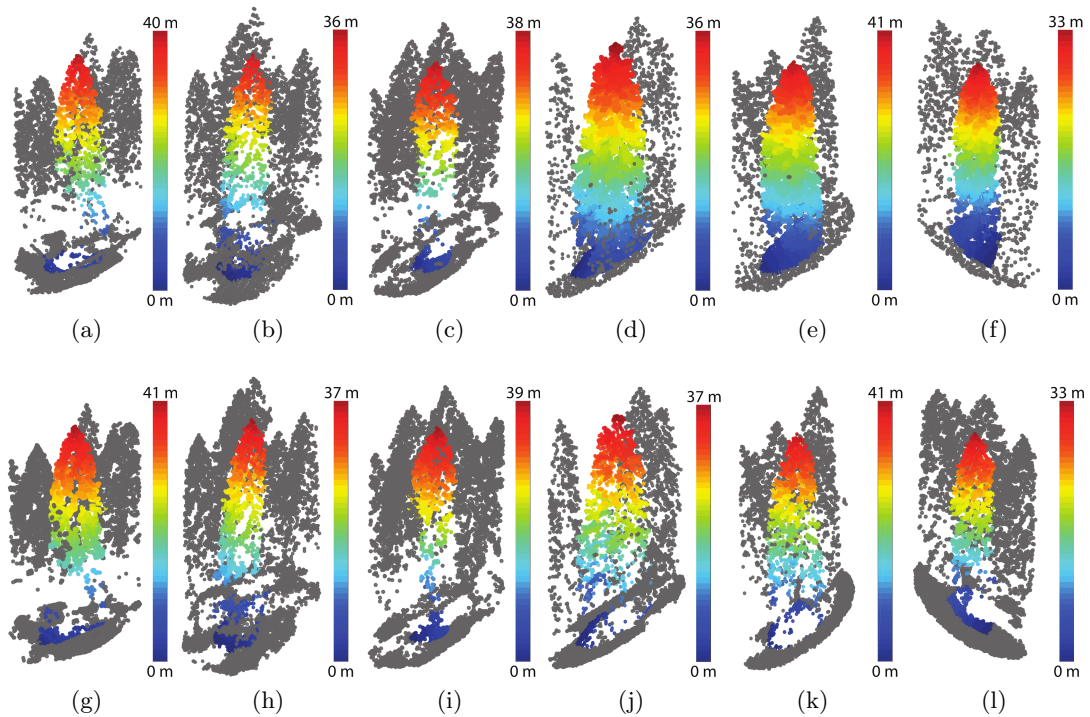


Figure 3.10: Qualitative examples of delineated tree-canopies obtained by the proposed crown following approach (the segmented crowns are displayed in bright colors): (a-f) segmented crowns at time t_1 ; (g-l) segmented crowns at time t_2 .

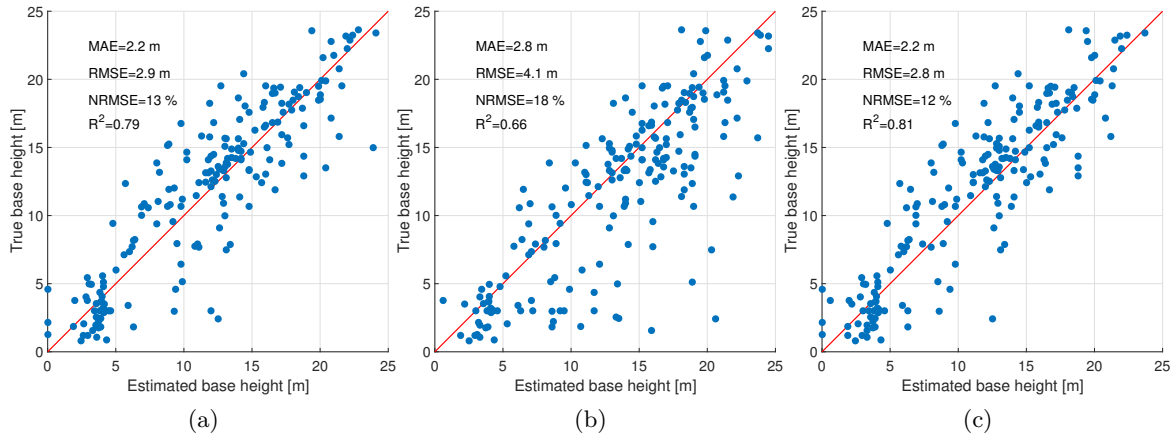


Figure 3.11: True versus estimated base height (bh) for all the stands: (a) single-date estimation at time t_1 , (b) single-date estimation at time t_2 , (c) bitemporal estimation.

At the end of the tree detection part, we move to the crown delineation. Figure 3.9 shows the scatter plots and error metrics for the estimated crown radius at the two dates. The plots show the effectiveness of the proposed segmentation method which accurately segments the tree-crowns and estimates the crown radius. Thus, the coefficient of determination R^2 shows quite high values at both dates ($R^2 = 0.72$ at time t_1 and $R^2 = 0.72$ at time t_2). In addition, the visual analysis (see Figure 3.10) of the segmented point clouds confirms the accuracy of the segmentation results. To validate the 3-D model used to represent the structure of the crown, we evaluate the bh estimation (Figure 3.11). In particular, Figures 3.11a and 3.11b show the results obtained when the estimation is carried out at the single-date, while Figure 3.11c shows the base height estimated by fusing the bitemporal data. As one can see in Figure 3.11b, the base height estimation at time t_2 is less accurate than the one obtained at time t_1 since the LiDAR data acquired at time t_2 (on both the study areas) are characterized by a smaller pulse density that results in a reduced penetration rate of the laser in the lower portion of the canopy, thus making the base height estimation less reliable. However, Figure 3.11c shows that by fusing the bitemporal information of the two acquisitions we can improve the base height estimation with respect to each single-date. Indeed, we improved the coefficient of determination from $R^2 = 0.79$ (at time t_1) and $R^2 = 0.66$ (at time t_2) to $R^2 = 0.81$. It is worth noting that, even though the denser point cloud can be used to improve the crown parameters estimation on the other point cloud, a lower bound on the point density for the applicability of the method should be identified. If the point density of both the point clouds is too low the crown parameters will be inaccurately estimated at both dates. A reasonable lower bound on the pulse density is 5 pulses/m².

The final step of the proposed hierarchical CD method performs bitemporal analysis at the individual tree level to detect and quantify the single-tree changes. Figure 3.12 shows, for each stand, the map with the corresponding identified classes, while Figure 3.13 shows a qualitative example of the object-based change detection of a single-tree. Table 3.4 shows the statistics of the top height and crown volume for each stand together

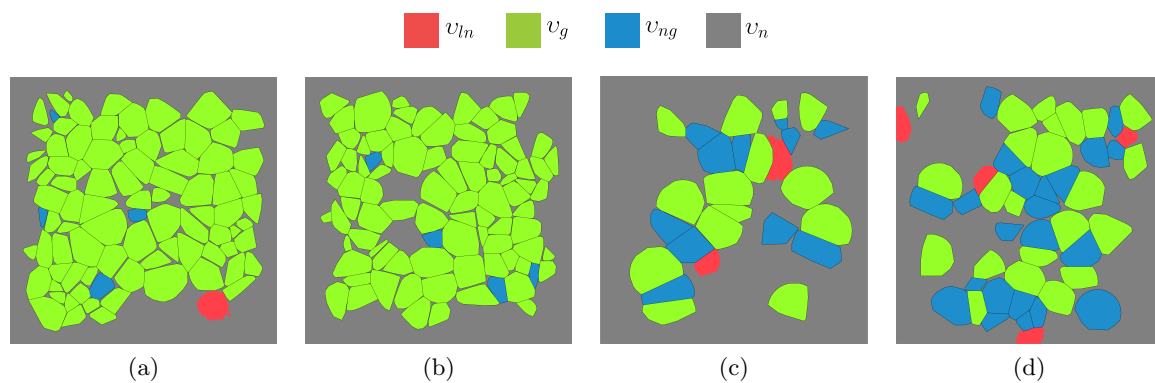


Figure 3.12: Maps representing the different kinds of change identified in the considered stands (i.e., v_{ln} large negative changes, v_g trees with significant growth, v_{ng} trees with no significant growth, v_n areas of no interest for forest studies): (a) S1, (b) S2, (c) S3, (d) S4.

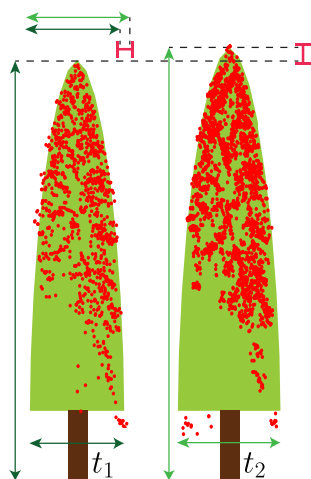


Figure 3.13: Real example of CD at the individual tree level showing the 3-D model (with the two related segmented point clouds in red). Note the height and horizontal growth that contribute to the crown volume variation.

with the corresponding dH and dV statistics. It is worth noting that the statistics of the single-tree changes have been computed considering both the trees in v_{ng} and v_g . Focusing on the vertical growth showed in Table 3.4a, we can observe a different behavior in stands S1 and S2 and stands S3 and S4. Indeed, stands S3 and S4 show a vertical growth with a mean variation of 0.4 m and 0.3 m, respectively, whereas stands S1 and S2 show a vertical growth of 1 m and 0.9 m, respectively. These results are in agreement with the expectation of the team of experts of the forest service since stands S3 and S4 are characterized by older trees with respect to stands S1 and S2. Indeed, it is well known that the age of the tree influences its growth rate which decreases as the age of the tree increases. This observation can be extended also to the crown volume variation. Table 3.4b shows that in stands S1 and S2 there is a larger variation in terms of crown volume growth with respect to stands S3 and S4. Moreover, Figure 3.12 shows that for stands S3 and S4 there is a larger number of trees that do not show significant growth (i.e., belong to class v_{ng}) with respect to stands S1 and S2. Note that stands S1 and S2 have very similar characteristics in terms of forest structure (see Figures 3.5a and 3.5b); this is also true for stands S3 and S4 (Figures 3.5c and 3.5d). This condition affects the single-tree changes since stands with similar characteristics show similar value of vertical and crown volume growth.

Table 3.4: Statistics of the individual tree parameters CD for each stands at both dates and in terms of: (a) dH ; (b) dV .

(a)						
Stand	Top height [m]				dH [m]	
	t_1		t_2		Range	Mean
	Range	Mean	Range	Mean		
S1	16.9-42.9	35.2	18.3-44.1	36.2	0-2.8	1
S2	18.7-40.6	33.4	19.5-41.5	34.3	0-2.7	0.9
S3	6.8-41.7	33.9	7.2-41.8	34.4	0-2.5	0.4
S4	21-46.2	36.5	21.3-46.4	36.7	0-0.7	0.3

(b)						
Stand	Crown Volume [m ³]				dV [m ³]	
	t_1		t_2		Range	Mean
	Range	Mean	Range	Mean		
S1	53-1200	431	54-1237	463	0-93	31
S2	55-1265	345	73-1284	373	0-95	27
S3	57-2394	1044	88-2410	1058	0-42	14
S4	150-2160	987	150-2179	1004	0-67	15

3.4 Conclusion

In this work we have presented a method for the detection of 3-D changes in forest areas using bitemporal LiDAR data. The method first detects the large changes and then focuses on the individual tree-canopy in order to detect the single-tree changes by means of an object-based CD. The object-based CD identifies both the vertical and the crown volume growth of each single-tree.

The experimental results confirmed the effectiveness of the proposed method. The large changes were accurately identified in all the considered stands with low false and missed alarm rates. In the tree detection phase, after the matching we jointly use the bitemporal LiDAR data in order to reduce the number of CE (from 4.9-5.5% to 1.7%) without significantly increasing the number of OE (from 2-2.6% to 2.3%). Regarding the canopy characterization, we used a 3-D ellipsoid model in order to reconstruct the canopy structure considering the bitemporal information to improve the parameters estimation accuracy. The comparison between estimated parameters and the true parameters pointed out that the method estimated the crown radius with an R^2 of 0.72 at both dates. The base height estimation performed at the single-date showed good performance at time t_1 with an R^2 of 0.79, whereas at time t_2 the estimation was significantly less accurate with an R^2 of 0.66. However, by fusing the information of the two dates we reduced the effect of the low penetration of the laser in the lower portion of some canopies thus improving the estimation reaching an R^2 of 0.81. By means of the 3-D ellipsoid, we computed the vertical growth dH and crown volume growth dV for each tree. The statistics of these changes were consistent with what expected by the experts of the regional forest service according to the properties of the analyzed stands. In particular, stands S1 and S2 showed a larger vertical growth (i.e., 1-0.9 m) with respect to stands S3 and S4 (0.4-0.3 m) which are characterized by older trees. The crown volume growth showed similar results with the first two stands characterized by a growth of 31 m³ and 27 m³, respectively. One of the most important properties of the proposed method is that it can effectively compare LiDAR data with different pulse densities. However, for an accurate characterization of the tree growth the lower bound on each single-date density is of 5 pulses/m².

As future developments of this work, we plan to extend the detection of single-tree changes to analyze the variation of biomass in order to better characterize the health status of the forest and to test the proposed method on forests with younger trees to analyze the growth rate of trees with very different ages. Finally, we plan to use convex hull and alpha shape in order to characterize more accurately the canopy structure and thus its changes.

Chapter 4

A Method based on Binary CVA for Multiple Change Detection in Hyperspectral Images

This Chapter¹ presents a novel method for unsupervised multiple CD in bitemporal HS images based on a discrete representation of the change information. Differently from the state-of-the-art methods, which address the high dimensionality of the data using band reduction or selection techniques, in this work we focus our attention on the representation and exploitation of the change information present in each band. After a band-by-band pixel-based subtraction of the bitemporal images, we define the Hyperspectral Change Vectors (HCVs). The change information contained in the HCVs is then simplified by independently analyzing the radiometric information of each band to generate a quantized discrete representation of the HCVs. These discrete HCVs are jointly analyzed by considering the hierarchical nature of the changes in HS images. A tree representation is defined and used to discriminate between different kinds of change. The proposed method has been tested on a simulated dataset and two real bitemporal datasets acquired by the Hyperion sensor over agricultural areas. Experimental results confirm that the proposed method can automatically detect and discriminate between the different changes using bitemporal HS data.

4.1 Introduction

In the literature, most of the existing CD methods are designed for multitemporal MS images and Synthetic Aperture Radar (SAR) data. Here we focus on the former. CD methods for optical passive data can be split into two main categories: i) binary CD [166, 185–192], and ii) multiple CD [168, 193–200]. Binary CD consists in the discrimination between changed and unchanged samples only. It can be performed either in the spectral

¹This Chapter appears in:

[J2] D. Marinelli, F. Bovolo, L. Bruzzone, "A Novel Change Detection Method for Multitemporal Hyperspectral Images Based on Binary Hyperspectral Change Vectors," in *IEEE Transactions on Geoscience and Remote Sensing*, vol. 57, no. 7, pp. 4913-4928, July 2019.

band domain using all the spectral channels or by manually selecting the relevant ones [185], or by working in a transformed feature space. The most common approach is to apply a threshold to the magnitude of the difference image (obtained by pixel-by-pixel subtraction of each spectral channel of the bitemporal images). The statistical distribution of the magnitude variable can be modelled either in parametric [166] or non parametric ways [201]. The decision strategy can be designed in the Bayesian framework according to minimum error [166] or minimum cost [186] rules. Other methods are based on the use of genetic algorithms [187], fuzzy clustering [188] or data fusion techniques [189]. Pixel based results can be improved by taking into account the spatial correlation. Examples of this include Hopfield-Type neural networks [190], self-organizing feature map neural network [191] or Markov Random Fields [192].

Multiple CD methods allow for the discrimination between multiple kinds of change. Existing methods can be either supervised [193–199] or unsupervised [168, 200]. Supervised methods use training data to achieve accurate CD results. Among them we recall: i) post classification comparison [193–195]; ii) direct multirate classification [196]; and iii) compound classification [197–199]. A critical analysis of these kinds of approach can be found in [21, 112]. The key issue is that multitemporal labelled reference data are seldom available thus making unsupervised methods potentially more useful also in the more complex multiple CD case. Some of the existing unsupervised multiple CD methods are based on transformations such as Independent Component Analysis (ICA) [200] or multivariate analysis techniques (e.g., Multivariate Alteration Detection [168]).

In Chapter 2 we pointed out that multitemporal analysis of HS images introduces new problems with respect to MS data. Thus, most of the methods for MSCD can not be effectively used to perform CD on in HS images. The analysis of the existing methods for HSCD presented in Chapter 2 points out that most of them address the high complexity of CD in HS images by applying transformations or feature reduction techniques. This is done to reduce: i) the dimension of the features space and thus the computational burden; and ii) the noise impact and thus the number of errors. This often results in a loss of change information. Moreover, most of the existing feature reduction techniques are developed for single-date analysis and are often supervised thus limiting their use in a multitemporal framework. Indeed, in the multitemporal case change information showing low prior probability should be preserved and unsupervised method are preferred being multitemporal ground truth seldom available. Little work has been done regarding the definition of alternative effective representations of change that focus on the relevant change information of each band of the HCVs. Accordingly, we work on the HCVs to highlight the change information by representing the HCVs with binary codewords. For a given HCV, each spectral channel is represented using Q bits (where in HS images typically $Q \geq 10$) to code all the possible radiometric values. In the new representation we can reduce the number of bits used for each band thus moving from 2^Q (e.g., $2^{12} = 4096$) to few values that represent the essential change information in each channel. To this end, the method first performs a binary CD to discriminate between changed and unchanged HCVs. It then focuses only on the changed HCVs (the ones with a high magnitude value induced by change impact on one or more spectral channels) in order to convert them into binary codewords working on each band separately. The method adaptively quantizes the

values of the HCVs at the considered band so that different kinds of change fit to different quantization intervals. In such a way, the behavior of each change (or group of changes) is modeled accurately in each band and coded using binary strings. The fusion of the band-by-band binary representations provides a codeword that models the change information content of the full HCV. Thus, despite binarization is conducted on each band separately, the correlation of the change information in adjacent spectral bands is preserved. The binary codewords are then compressed across bands to reduce the remaining redundant information. Finally, the method organizes the codewords in a dendrogram (i.e., a tree structure) by means of an agglomerative hierarchical clustering. The hierarchical structure allows us to obtain different results in terms of level of detail of the CD by cutting the dendrogram at different heights. The entire process is unsupervised.

The main novel contributions of the proposed method are:

- An adaptive band-dependent model to represent the information of multiple kinds of change in bitemporal HS images.
- A compressed representation of the bitemporal information associated to changes that is simple, efficient and reduces data volume.
- An adaptive mechanism to discriminate between the kinds of change depending on the selected sensitivity.

The method has been tested on a simulated HS dataset and on two real bitemporal HS datasets acquired by the Hyperion sensor over two agricultural areas in Washington state (USA) and in the Albacete province (Spain). Experimental results confirmed the effectiveness of the proposed method. The rest of the paper is divided in 3 Sections. The next Section describes in detail the proposed method. Section 4.3 presents and analyzes the experimental results. Finally Section 4.4 draws the conclusion.

4.2 Proposed Method for Unsupervised Change Detection in Hyperspectral Data

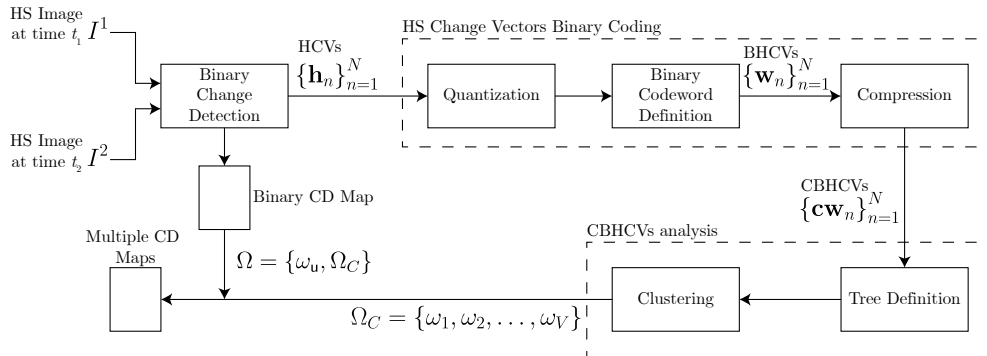


Figure 4.1: Block scheme of the proposed method for unsupervised multiple CD.

Figure 4.1 shows the block scheme of the proposed method that consists of three main steps: i) binary CD; ii) Hyperspectral Change Vectors Binary Coding; iii) Compressed

Binary Hyperspectral Change Vectors analysis. The binary CD separates changed from unchanged samples. After that the method focuses on the changed samples only. The coding of the changed HCVs first adaptively quantizes the values of the HCVs in each band to simplify the representation of the change information. The codeword definition and compression steps allow us to obtain binary codewords coding the change information contained in all the spectral channels. Finally, the Compressed Binary Hyperspectral Change Vectors (CBHCVs) analysis separates the different kinds of change.

Let I^1 and I^2 be two HS images acquired at times t_1 and t_2 , respectively with $I^1 = \{I_b^1\}_{b=1}^B$ and $I^2 = \{I_b^2\}_{b=1}^B$, where I_b^1 and I_b^2 are the single band images representing the b th spectral channel. We define $\Omega = \{\omega_u, \Omega_C\}$ as the set of classes containing both unchanged (ω_u) and changed (Ω_C) pixels. $\Omega_C = \{\omega_1, \omega_2, \dots, \omega_V\}$ is the macro-class of changed pixels that can be further divided into V classes, one for each type of change.

4.2.1 Binary Change Detection

The first step of the method is the binary CD that discriminates between changed and unchanged pixels. To this end, we follow a state-of-the-art approach based on the statistical analysis of the magnitude of the difference image which has been extensively used in the literature [166, 186, 202, 203]. However, note that other binary CD strategies could be used. First we compute the HS difference image as $I_D = I^2 - I^1$ and its magnitude I_ρ as:

$$I_\rho = \sqrt{\sum_{b=1}^B (I_{D,b})^2}. \quad (4.1)$$

It is expected that unchanged pixels show a small magnitude value whereas changed one show large magnitude. Thus, we analyze the Probability Density Function (PDF) of I_ρ in order to discriminate between ω_u and Ω_C . According to the literature, we approximate the PDF of the magnitude as a mixture of two parametric distributions. Unchanged pixels are approximated as Rayleigh distributed whereas the changed ones are approximated as Rice distributed [167]. After estimating the parameters of the two models using an Estimation Maximization (EM) algorithm, according to Bayes theory it is possible to determine a threshold T_ρ such that pixels below T_ρ belong to class ω_u , whereas pixels above T_ρ belong to class Ω_C . From here on we focus on the set $\{\mathbf{h}_n\}_{n=1}^N$ of N changed HCVs ($\mathbf{h}_n \in \Omega_C, \forall n = 1, \dots, N$), where $\mathbf{h}_n = \{h_{n,b}\}_{b=1}^B$ is the n th HCV and $h_{n,b}$ the value at b th spectral channel of \mathbf{h}_n .

4.2.2 Hyperspectral Change Vectors Binary Coding

In the second step we move from the real valued representation of the HCVs usually employed in the literature to the novel binary codeword based one. The aim is to provide a simpler yet effective representation of the HCVs focused on the information associated with different kinds of change and thus able to improve their separability. Figure 4.2a shows that kinds of change in the original HCV space (i.e., the real valued space) can be discriminated more or less effectively depending on the considered band. As an example, in band b_y (Figure 4.2a) it is possible to separate between two groups of changes (ω_1, ω_2

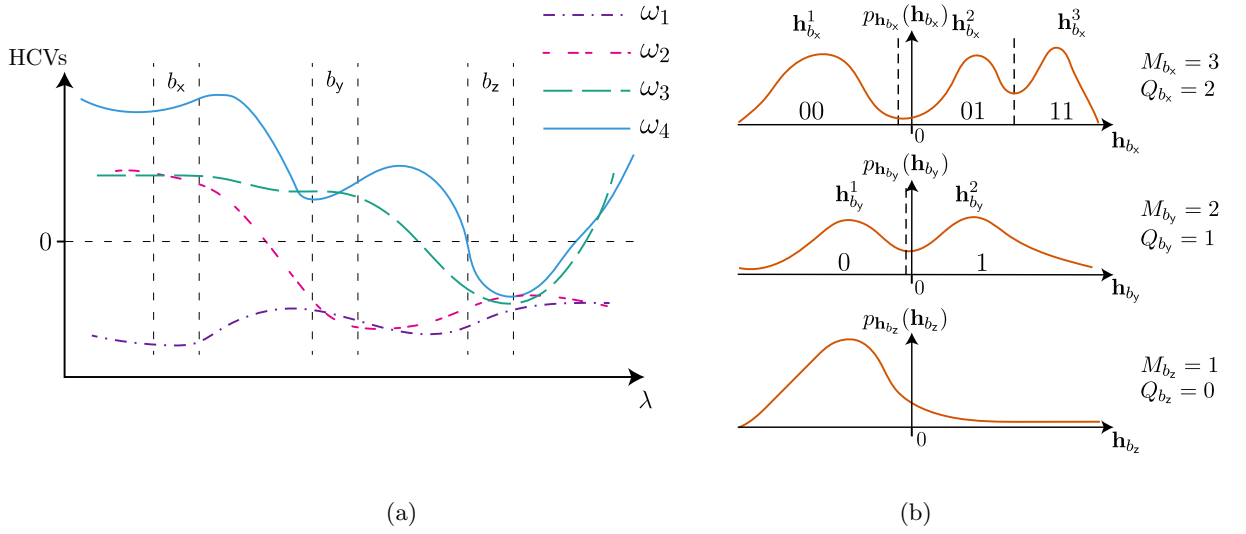


Figure 4.2: Qualitative illustration of the quantization step of the proposed technique: (a) HCVs of 4 pixels belonging to 4 different kinds of change (ω_{1-4}). (b) Probability Density Functions of the values of the changed pixels for the 3 bands. The dashed lines identify the boundaries of the quantization intervals with the corresponding binary strings.

and ω_3, ω_4) whereas in band b_z the four changes are indistinguishable from each other. This illustrates that bands may contain significantly different change information with some of them (e.g., bands b_x and b_y) being more relevant to the CD problem with respect to others (e.g., band b_z) where all the changes show similar values and cannot be separated. Therefore, we adaptively analyze each band to detect the information that can be useful for the change discrimination. At the same time we represent each HCV in a more efficient and compact way. In particular, we move from the common real valued representation to the proposed binary representation by assigning to each HCV \mathbf{h}_n a binary codeword referred to as CBHCV \mathbf{cw}_n . This is achieved by: 1) *Quantization*; 2) *Binary Codeword Definition*; 3) *Compression*.

1) *Quantization*: It identifies, by working separately on each band, the information that allows us to separate the different changes. We consider the content of a band relevant for solving the CD problem if we can identify more than one cluster of pixels, where each cluster contains the samples related to a given kind of change or a group of kinds of change. This is reflected in the PDF of the values of $\mathbf{h}_b = \{h_{n,b}\}_{n=1}^N$ (i.e., values of the b th component of the HCVs) since samples that fall inside the same mode are likely to belong either to the same kind of change or different changes that in turn are indistinguishable using the informative content of the considered band. In contrast, samples that fall inside different modes are likely to belong to different kinds of change. Thus, we are interested in identifying these modes. Figure 4.2b shows the PDFs of the values in \mathbf{h}_b for the 3 different bands b_x, b_y, b_z . In band b_z only one mode exists whereas for bands b_x and b_y more modes can be identified. Therefore, we can simplify the radiometric information related to changes of each band by quantizing the $h_{n,b}$ in the same mode into one single quantization interval. Since different bands contain different change information, the

proposed quantization step has to be performed adaptively in order to properly preserve and capture the change information. A uniform band-by-band quantization would lead to split samples belonging to the same change class into different quantization levels and thus to a poor representation.

To apply the quantization, we identify and separate the modes so that each one corresponds to a quantization interval. To this end, first we estimate the PDF $p_{\mathbf{h}_b}(\mathbf{h}_b)$ of \mathbf{h}_b using a Kernel Density Estimator (KDE) [201] (however, any other estimation methods can be used). Then we search for the M_b modes of $p_{\mathbf{h}_b}(\mathbf{h}_b)$ by identifying the local maxima and we define M_b quantization intervals. Note that M_b can vary for different spectral channels. If only one mode is identified (i.e., $M_b = 1$), the band is discarded (e.g., band b_z in Figure 4.2b). The boundaries of each quantization interval are positioned at the minimum between two modes with the corresponding interval as large as the distance between the two minima. Each $h_{n,b} \in \mathbf{h}_b$ is assigned to the corresponding quantization interval thus obtaining M_b sets $\{\mathbf{h}_b^m\}_{m=1}^{M_b}$ (see Figure 4.2b). The PDF estimation is intrinsically subject to errors. Moreover, typically the modes of the PDF are overlapped. Therefore, it is likely that the quantization leads to errors such as that pixels belonging to the same kind of change are split by a wrongly positioned boundary. Quantization errors mitigation will be addressed in the following. The proposed strategy results in better performance than other approaches like those based on clustering.

2) *Codeword Definition:* After the quantization step, we move to the binary representation of the quantized intervals. For a given band, we assign a different binary string to each quantization interval and thus to all the pixels in the corresponding set \mathbf{h}_b^m . For each band b , the length Q_b of the corresponding binary string depends on the number of quantization intervals M_b . We compute the number of bits as $Q_b = \lceil \log_2 M_b \rceil$. Note that since $2^{Q_b-1} < M_b \leq 2^{Q_b}$ some combinations of binary strings may remain unused. The binary strings are coded according to the Gray code such that adjacent quantization intervals (i.e., modes) differ by only one bit at the considered band. This reduces the impact of the errors introduced in the quantization step in the binary codeword representation. Figure 4.2b shows an example of the binary string assigned to each quantization interval for the two bands b_x, b_y .

Concatenating the binary strings assigned to a pixel in the B bands, we obtain its codeword which codes the change information of the corresponding HCV. By applying the codeword definition for each band to each $\mathbf{h}_n \in \{\mathbf{h}_n\}_{n=1}^N$, we obtain a set of codewords $\{\mathbf{w}_n\}_{n=1}^N$ called Binary Hyperspectral Change Vectors (BHCVs). Each $\mathbf{w}_n = \{w_{n,i}\}_{i=1}^I$, ($w_{n,i} \in \{0, 1\}$) is a binary string of length $I = \sum_{b=1}^B Q_b$. In the I_D the number Q of bits used for each band is constant and thus the total number of bits required to code a HCV is $Q \times B$. Since typically $Q \geq 10$ whereas Q_b is much smaller (we expect $Q_b \leq 3$ in most of the cases), then $I \ll Q \times B$.

3) *Compression:* The last step of the coding of the HCVs is the compression of the codewords in $\{\mathbf{w}_n\}_{n=1}^N$. Typically, HS data are highly redundant due to the narrow sampling of the spectrum. This means having large number of samples showing very similar values at multiple bands. When moving to the codeword based representation, redundancy still exists. In this domain, there is redundancy when a large portion of the samples in set \mathbf{h}_b is quantized identically (i.e., the same samples are split into the same groups)

at multiple bands. In terms of binary representation, this translates into large number of samples that share the same value for more than one bit of the codeword. Thus, we propose to analyze the redundancy in terms of groups of bits (i.e., redundant bits) that have equal values for a large number of samples.

In order to search for the redundant bits, first we sort them along the i index (i.e., we swap the position i of the bits) in such a way that groups of bits showing the same value for a large number of samples are positioned near each other. The sorting algorithm [204] first produces a tree structure with I leaves where the i th leaf represents the binary vector of length N containing the values of the i th bit of all the codewords in $\{\mathbf{w}_n\}_{n=1}^N$. It then applies an efficient leaf ordering method that aims at maximizing the sum of the similarities of the elements of adjacent leaves (note that others sorting algorithm could be used). We obtain a new set $\{\mathbf{w}'_n\}_{n=1}^N$ (with $\mathbf{w}'_n = \{w'_{n,i}\}_{i=1}^I$) of BHCVs that contains exactly the same change information of the set $\{\mathbf{w}_n\}_{n=1}^N$ with the bits sorted according to similarity. Tables 4.1a and 4.1b show an example with a set of 5 BHCVs before and after the ordering, respectively. The ordering allows us to simplify the identification of redundant bits since set $\{\mathbf{w}'_n\}_{n=1}^N$ is defined so that they are positioned near each other. We can now identify these groups by evaluating the redundancy of adjacent bits. To this end, we compute the sum of all the N pairwise Hamming distances of two bits i and $i + 1$ as:

$$\eta(i, i + 1) = \sum_{n=1}^N |w'_{n,i+1} - w'_{n,i}|, i \in \{1, \dots, I - 1\}. \quad (4.2)$$

Distance η will show small values when the pair of adjacent bits $(i, i + 1)$ contains redundant information whereas it will show large values when the change information of the two bits is not redundant. The last rows of both Table 4.1a and Table 4.1b show the Hamming distances computed between each adjacent pair of bits. Note that in Table 4.1a the values of η are much larger and distributed with respect to Table 4.1b. This highlights how the bit ordering effectively positions near each other bits with similar information.

We analyze the vector η to find sequences of small values (i.e., groups of redundant bits) surrounded by large values (i.e., adjacent pairs not redundant). We consider two adjacent bits i and $i + 1$ redundant if $\eta(i, i + 1) \leq T_\eta$, ($T_\eta > 0$) and not redundant if $\eta(i, i + 1) > T_\eta$. By applying the threshold to the distances we identify the groups of redundant bits (i.e., groups of adjacent bits for which $\eta \leq T_\eta$) and those that are likely to be not redundant and thus that contain relevant and unique change information. The horizontal lines in Table 4.1b highlight the different groups of bits that have been identified as containing redundant informations and thus should be compressed. Here we propose to work separately on each BHCV and compress each group of redundant bits into one bit using a majority rule. This allows us not only to reduce the redundant information, but also the number of errors thus reducing the number of outliers. Indeed, the majority rule can filter out outliers (e.g., a bit that in very few samples shows a different value with respect to the other bits of the redundant group). The new set $\{\mathbf{cw}_n\}_{n=1}^N$ is composed by binary strings defined as Compressed Binary Hyperspectral Change Vectors (CBHCVs) where each $\mathbf{cw}_n = \{cw_{n,j}\}_{j=1}^J$, ($cw_{n,j} \in \{0, 1\}$, $J \ll I$). Note that the compression rate I/J is strongly dependent on the set $\{\mathbf{w}'_n\}_{n=1}^N$ and the amount of redundant information it contains. Table 4.1c shows the CBHCVs of the corresponding sorted BHCVs of Table

4.1b. Note that unlike existing dimensionality reduction methods (e.g., [205–208]), the proposed compression of BHCVs is specifically designed to exploit the simplified binary representation of the change information.

Table 4.1: Compression of the codewords of five pixels: (a) BHCVs before the bit sorting showing the Hamming distance η between adjacent pairs of bits. (b) sorted BHCVs. (c) Codewords after the compression (i.e., CBHCVs). The values of η in bold in (b) satisfy $\eta \leq T_\eta$.

(a)									
\mathbf{w}_1	1	1	1	0	1	1	1	1	1
\mathbf{w}_2	1	1	1	0	1	1	1	1	1
\mathbf{w}_3	0	1	1	0	0	0	1	0	0
\mathbf{w}_4	0	1	0	1	0	0	1	0	0
\mathbf{w}_5	0	1	0	1	0	0	1	0	0
η	3	2	5	4	0	3	3	3	0

(b)									
\mathbf{w}'_1	1	1	1	1	1	1	1	1	0
\mathbf{w}'_2	1	1	1	1	1	1	1	1	0
\mathbf{w}'_3	1	0	0	0	0	0	1	1	0
\mathbf{w}'_4	0	0	0	0	0	0	1	1	1
\mathbf{w}'_5	0	0	0	0	0	0	1	1	1
η	1	0	0	0	0	0	3	0	3

(c)			
\mathbf{cw}_1	1	1	0
\mathbf{cw}_2	1	1	0
\mathbf{cw}_3	0	1	0
\mathbf{cw}_4	0	1	1
\mathbf{cw}_5	0	1	1

4.2.3 Compressed Binary Hyperspectral Change Vectors Analysis

In the last phase we exploit the simplified binarized representation of the change information (i.e., the codewords) to discriminate between the different kinds of change. HS data allow us to discriminate between both major land cover changes and more subtle changes [24]. The sensitivity required in the discrimination between the kinds of change may vary depending on the considered application. Indeed, whereas in some cases one may want to discriminate between all the possible kinds of change, this may not be the case for other applications in which the main aim is to detect specific land cover changes only. For this reason, we propose to represent the set of changed samples in a hierarchical tree structure defined using an agglomerative hierarchical clustering approach. This representation al-

lows us to analyze the tree at different depths which correspond to different sensitivities in the discrimination of the kinds of change.

The HCVs coding phase resulted in a simplified representation of the change information. Thus, we expect to have a large number of changed pixels that share the same CBHCVs. First, we select only the unique CBHCVs $\{\mathbf{ucw}_u\}_{u=1}^U$ and we compute the corresponding prior probabilities as:

$$P_u = \frac{|\{n \in \{1, \dots, N\} : \mathbf{cw}_n = \mathbf{ucw}_u\}|}{N}, \quad (4.3)$$

where $|\cdot|$ is the cardinality of the set. We can assume that, if the prior probability P_u of an unique CBHCVs is low, the corresponding samples are non interesting outliers or are related to errors in the HCVs coding step (which have been reduced by the compression step). Therefore, we discard the \mathbf{ucw}_u for which $P_u \leq T_P$, where T_P is a threshold on the prior probability. However, it may happen that CBHCVs with very low prior probabilities actually correspond to a real change which occurred only in a very small area. Thus, the value of threshold T_P has to be selected considering the trade-off between the capability of removing noisy samples and outliers and the risk of losing true changes. The hierarchical clustering is then applied only to the \mathbf{ucw}_u for which $P_u > T_P$, which is a set $\{\mathbf{ucw}'_u\}_{u=1}^{U'}$ where $U' \leq U$.

The agglomerative hierarchical clustering is based on the Unweighted Pair Group Method with Arithmetic Mean (UPGMA). The algorithm starts with U' clusters, each corresponding to an unique \mathbf{ucw}'_u and at each iteration it merges the two most similar clusters. Merging is conducted according to the pairwise normalized Hamming distance. Since the compression involves groups of redundant bits with different sizes, the Hamming distance is computed in a weighted manner, where the weight of each bit of the CBHCVs is directly proportional to the number of bits that were compressed to generate it. The pairwise distance computation is the most computationally demanding part of the clustering algorithm since it requires the computation of $U'(U' - 1)/2$ distances. However, since $U' \ll N$ the computational time is significantly smaller with respect to computing the pairwise distances in the original domain which means computing $N(N - 1)/2$ distances ($U'(U' - 1)/2 \ll N(N - 1)/2$). At each iteration, after merging the two most similar clusters, the algorithm recomputes the distance between the newly formed one and all the others. Let us consider the first iteration of the algorithm and three generic clusters $\mathbf{ucw}'_1, \mathbf{ucw}'_2, \mathbf{ucw}'_3$ with prior probabilities P_1, P_2, P_3 , respectively. Let $\delta(\mathbf{ucw}'_1, \mathbf{ucw}'_2)$ be the pairwise distance between \mathbf{ucw}'_1 and \mathbf{ucw}'_2 . Let us suppose that we merge clusters \mathbf{ucw}'_1 and \mathbf{ucw}'_2 (i.e., $[\mathbf{ucw}'_1, \mathbf{ucw}'_2] = \mathbf{ucw}'_1 \cup \mathbf{ucw}'_2$ and $P_{1,2} = P_1 + P_2$). The distance between the new cluster $[\mathbf{ucw}'_1, \mathbf{ucw}'_2]$ and \mathbf{ucw}'_3 can be computed using the linkage criterion defined as:

$$\begin{aligned} \delta([\mathbf{ucw}'_1, \mathbf{ucw}'_2], \mathbf{ucw}'_3) &= \\ &= \frac{P_1 \delta(\mathbf{ucw}'_1, \mathbf{ucw}'_3) + P_2 \delta(\mathbf{ucw}'_2, \mathbf{ucw}'_3)}{P_{1,2}} \end{aligned} \quad (4.4)$$

This equation is general and applies to each iteration considering as inputs the distance values computed at the previous iteration. By weighting the distance using as weights

P_1 and P_2 we preserve the information regarding the prior probabilities of each unique CBHCVs. The algorithm iterates until all of the unique CBHCVs are merged into one single group and the tree structure (called dendrogram) is constructed. The length of the branches of the dendrogram is related to the distance between the clusters (i.e., a long branch indicates a significant difference between the samples contained in the two clusters).

To separate the samples into different kinds of change ω_v , the dendrogram can be cut at a given depth defined by a threshold T_δ . Figure 4.3 shows two examples of dendrogram cut that highlights how by cutting the tree at different depths we separate the changed samples into different numbers of clusters (3 and 6 in the example). By varying T_δ we vary the sensitivity of the method to the different kinds of change. Lowering T_δ corresponds to increasing the sensitivity of the method to the different kinds of change. Indeed, it is equivalent to a decrease of the threshold on the Hamming distance above which two CBHCVs are considered to belong to different kinds of change. Instead, increasing T_δ decreases the sensitivity of the method. Small values of T_δ may allow for the discrimination of very similar (in terms of spectral signature) kinds of change, but at the cost of an increased vulnerability to noise and outliers. A large value of T_δ may result in the grouping of different changes into the same cluster. Thus, the choice of T_δ has to be done taking into account the trade-off between sensitivity to the changes and robustness to noise. Moreover, note that the selection of T_δ can be easily done also in an iterative way by changing the threshold depending on the required level of detail of the CD map.

When T_δ is selected and thus the kinds of change are identified, the samples for which the corresponding \mathbf{ucw}_u shows a $P_u \leq T_P$ have to be assigned to one of the identified changes. To this end, we move back to the HCV representation and, for each sample that has to be assigned, we search for the nearest 50 samples (that have already been assigned to one change). We analyze the 50 nearest samples instead of considering only the nearest one in order to be more robust to outliers such as samples assigned to the wrong change. Finally, we assign the sample to the change that has the highest number of occurrences within the 50 samples.

4.3 Experimental Results

4.3.1 Experimental Setup

We tested the proposed method on one simulated dataset and two real bitemporal Hyperspectral datasets. The simulated dataset is based on a real HS image available in the Real-World Hyperspectral Images Database [209]. The image (Figure 4.4a) represents a wall in an outdoor area and was acquired by a Nuance FX camera that has a spectral resolution of approximately 10 nm with 31 bands ranging from 420 to 720 nm. To simulate changes, 7 tiles (colored tiles in Figure 4.4a) were extracted from the original image and inserted in different areas of the same image (Figure 4.4b). The selected tiles represent different materials and illumination condition thus simulating different changes. Additive White Gaussian noise was added to the simulated images (SNR 15 dB). Figure 4.4c shows the reference map of the 7 simulated changes.

The two real bitemporal Hyperspectral datasets were acquired by the Hyperion sen-

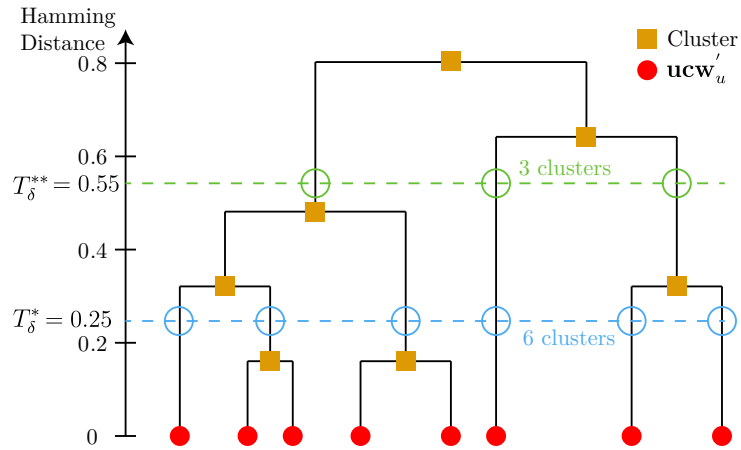


Figure 4.3: Example of a dendrogram. Red dots represent leaves and correspond to unique ucw'_u . Orange squares represent the clusters. The blue (T_δ^*) and green (T_δ^{**}) dashed lines show two examples of cut of the dendrogram.

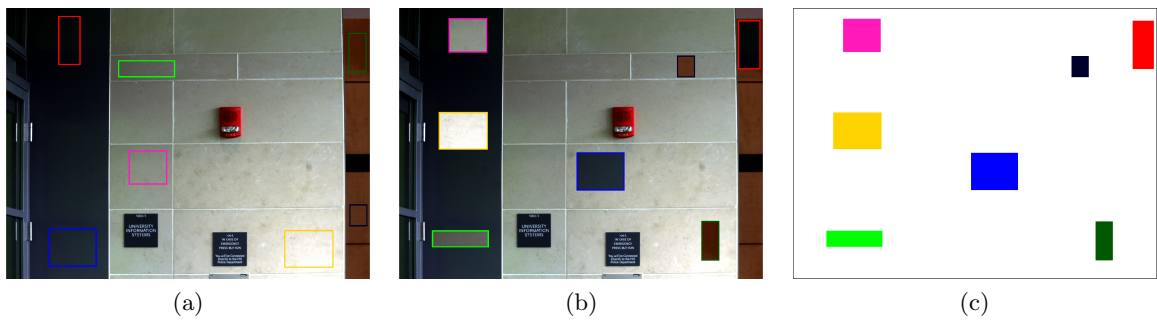


Figure 4.4: Simulated dataset: (a-b) true color composites (R: 710 nm; G: 620 nm; B: 510 nm) of the original (a) and simulated image (b) . (c) Reference change map where each color represents one of the 7 changes and white represent the no changed class.

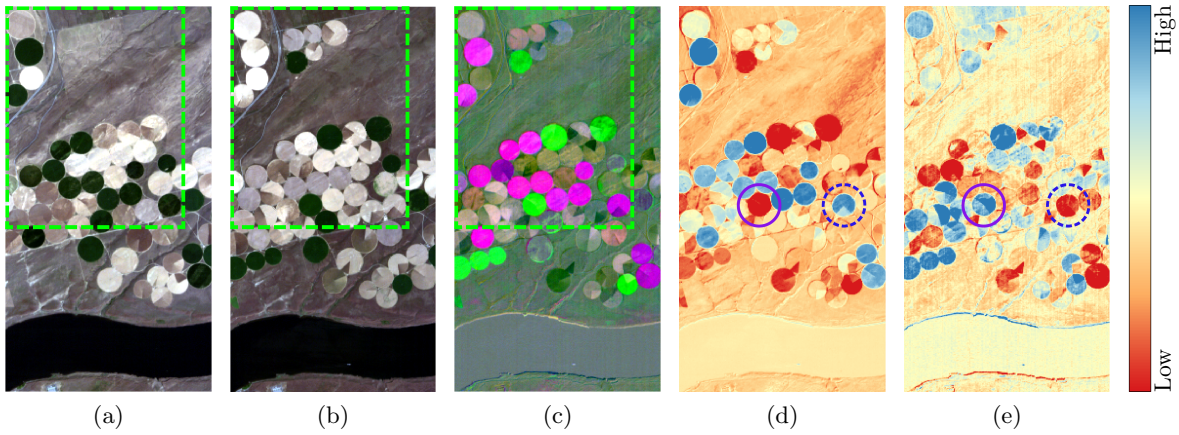


Figure 4.5: Benton County agricultural area dataset: true color composites (R: 640.5 nm, G: 569.27 nm, B: 467.52 nm) of the HS data acquired at times (a) t_1 (2004) and (b) t_2 (2008), respectively. (c) False color composite (R: 1729.7 nm, G: 1023.4 nm, B: 447.17 nm) of the difference image (i.e., HCV image). Single bands (d) 34 (691.37 nm) and (e) 103 (1174.77 nm) of the HCV image, respectively, with the corresponding color bar. The green dashed lines in (a-c) identify the portion of the dataset for which a reference map is available (BentonRM).

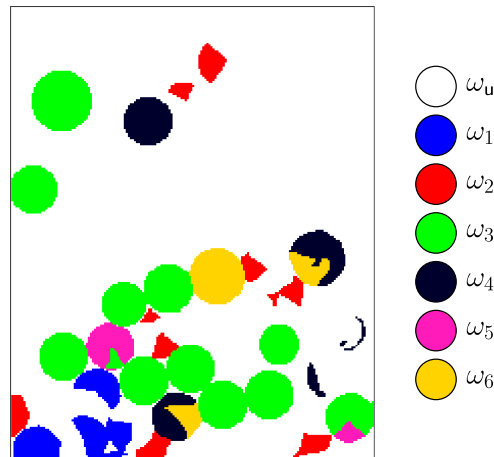


Figure 4.6: Reference map of the 6 classes of change (BentonRM dataset delineated by the dashed line in Figure 4.5).

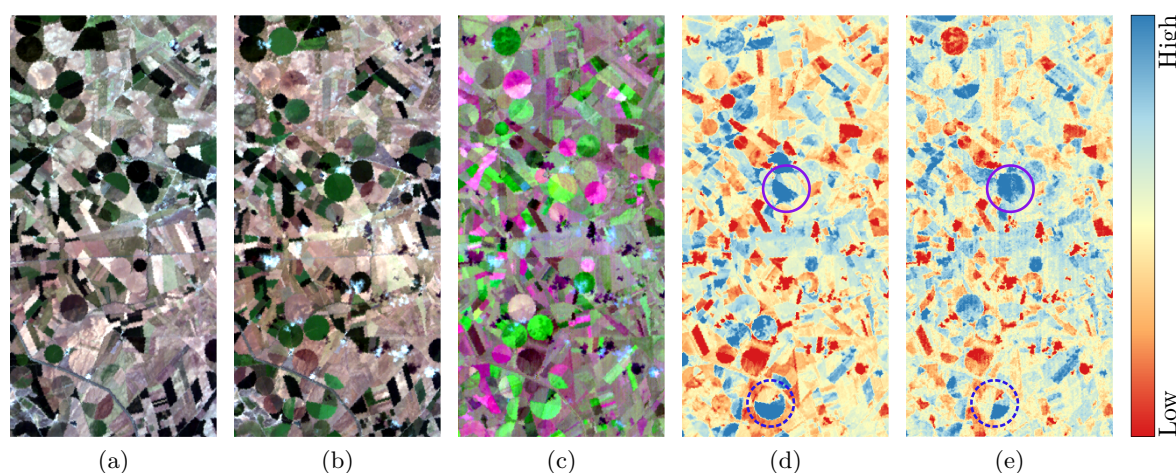


Figure 4.7: Albacete province agricultural area dataset: true color composites (R: 640.5 nm, G: 569.27 nm, B: 467.52 nm) of the HS data acquired at times (a) t_1 (2012) and (b) t_2 (2014), respectively. (c) False color composite (R: 1275.66 nm, G: 732.07 nm, B: 548.92 nm) of the difference image (i.e., HCV image). Single bands (d) 38 (732.07 nm) and (e) 100 (1144.48 nm) of the HCV image, respectively, with the corresponding color bar.

sor mounted on board the EO-1 satellite. The data used to generate these two datasets can be downloaded at [22]. The Hyperion data are characterized by 242 spectral bands ranging from 350 to 2580 nm, with a spectral resolution of 10 nm and a spatial resolution of 30 m. The second dataset represents an agricultural area in the Benton County, Washington, USA. The first image was acquired on May 1st, 2004 while the second image was acquired on May 8th, 2007. Figures 4.5a and 4.5b show the true color composition of the two HS images characterized by circular agricultural fields (due to the pivot irrigation system). Almost all the changes in this area are related to variations of the crop, soil or water content (caused by different amount of irrigated water) in the fields. The false color compositions of the HS difference image in Figure 4.5c highlights how the study area is characterized by different kinds of change and that one single field can be affected by more than one type of change. Figure 4.5c gives only a partial representation of the change information present in the data since only 3 spectral channel are exploited. The blue dashed circle in Figure 4.5d shows that two changes can be distinguished at band 34 but not at band 103 (Figure 4.5e). Conversely, the violet circle highlights a field that has uniform behavior at band 34 while it shows two uniform regions at band 103. This highlights how the different spectral channels can contain significantly different change information. For this dataset, a reference map (Figure 4.6) was defined by photointerpretation from experts² for a portion of the image (dataset box in Figure 4.5). We will refer to the portion of the Benton dataset with reference map as BentonRM.

The third dataset was acquired over an agricultural area in the Albacete province, Spain. The two images were acquired on May 22th 2012 (Figure 4.7a) and May 14th

²We thank Professor Sicong Liu from the College of Surveying and Geo-Informatics, Tongji University, Shanghai, China for providing the reference map of the BentonRM dataset.

2014 (Figure 4.7b). This area is characterized by agricultural fields with various shapes. The false color composition of the difference image (Figure 4.7c) shows that the area has been affected by different kinds of changes. Also for this dataset, most of the changes are related to variation of the crop, soil or water content and the presence of some clouds in the 2014 acquisition. The blue dashed circle and violet circle in Figures 4.7d and 4.7e confirm that for a given kind of change one or more bands may contain more relevant information with respect to other spectral channels.

We applied a radiometric calibration followed by an atmospheric correction carried out using the FLAASH algorithm [122, 210]. We applied the FLAASH algorithm only to the calibrated non overlapping bands, i.e., channels 8-57 and 79-224 [211]. Bands related to water absorption, i.e., bands 121-126, 167-180 and 222-224 [212] were removed as well as noisy bands with wavelength close to the water vapor absorption ones thus obtaining the final set of channels 8-57, 82-119, 131-164, 182-184, and 187-220. In the second dataset we removed also bands 117, 141, 146, 188, 198 due to bad stripes (band 117) and noise (bands 141, 146, 188, 198). It is worth noting that the selected bands still contain also noisy bands thus preserving the complexity of the two datasets.

We used the simulated dataset and the BentonRM dataset to perform a quantitative evaluation and we compared the numerical accuracy with the one obtained by the S²CVA [155], which is based on the manual identification of the different kinds of change. In order to have a fair comparison, we used the same binary CD map both for the proposed method and for the S²CVA. For the BentonRM dataset, multiple CD results are available for the method proposed in [118]. This method is based on a supervised Band Selection (BS) followed by a supervised classification of the difference image using a Support Vector Machine (SVM). In the BS-SVM the binary CD was performed in the classification step and thus it was not possible to use the same binary CD map. However, note that the two binary maps are very similar. The datasets with reference maps were also used for a sensitivity analysis of the method parameters. To perform this quantitative analysis, for both datasets we set the sensitivity (i.e., threshold T_δ) such that the number of identified change classes V is equal to the one of the reference map.

Quantitative CD results are presented for the pixels correctly identified as changed in the binary CD map. This allows us to assess the effectiveness of the proposed method in distinguishing types of change without error propagation from the binary CD step (which in turn is common with the S²CVA). Since no reference map is available for most of the second and the third datasets, we also validated the results by photointerpretation using different false color composites of the HCV images. For each of the two real datasets, we analyzed the effectiveness of the method in detecting changes with different levels of sensitivity setting T_δ to obtain as number of changes $V = 4$ and $V = 15$. Moreover, we used the S²CVA method to extract the changes and then we compared the resulting map with the one obtained by the proposed method setting T_δ to obtain the same number of changes as the S²CVA map.

We set the threshold T_η on the Hamming distance between adjacent bits (of the sorted BHCVs) to $0.1N$. The threshold T_P on the prior probability of each CBHCV was set to 0.001. Since our aim is to analyze the different CD maps obtained by varying the depth T_δ at which the dendrogram is cut, we did not set a fixed threshold T_δ , but we set a lower

bound. In particular, we set the lower bound of T_δ such that the maximum number of changes in which the samples can be separated is 15.

4.3.2 Results

Sensitivity Analysis

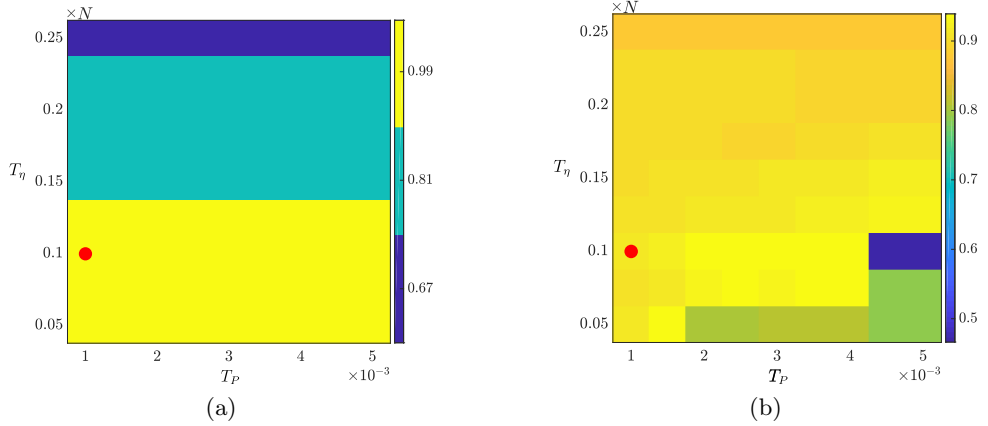


Figure 4.8: Sensitivity analysis results showing the values of the \mathcal{K}_c coefficient for different combinations of T_η and T_P : (a) simulated dataset and (b) BentonRM dataset. The red dot identifies the optimal settings.

Sensitivity analysis was conducted on the simulated dataset and on the BentonRM dataset by running the proposed method with different values of T_η and T_P ($T_\eta \in [0.05N, 0.25N]$ and $T_P \in [0.001, 0.005]$). For each combination of the two parameters we computed the \mathcal{K}_c (Cohen's Kappa) coefficient for the multiple CD result. Figure 4.8 shows a visual representation of the values of \mathcal{K}_c coefficient for different settings for the simulated dataset (Figure 4.8a) and for the BentonRM dataset (Figure 4.8b). In the simulated dataset, the proposed method reached a \mathcal{K}_c coefficient of 0.99 for a 44.4% of the combinations of the parameters, $\mathcal{K}_c = 0.81$ for another 44.4%. The remaining few cases are the ones corresponding to the combinations with $T_\eta = 0.25N$ which is at the very end of the considered interval. For the BentonRM dataset (Figure 4.8b), 44.4% of the combinations reached a \mathcal{K}_c coefficient larger than 0.9, while 48.1% of the combinations reached a value between 0.8 and 0.9. By analyzing these results we can conclude that the algorithm is robust to the variation of the threshold T_η and T_P .

Quantitative and Qualitative Comparison

For the simulated dataset (the reference map was used to eliminate unchanged samples), the quantization and codeword definition steps converted the $N = 113937$ changed HCVs into BHCVs composed by $I = 82$ bits. The compression step led to the CBHCVs obtaining codewords having a length of $J = 9$ bits. The CBHCVs analysis identified $U = 65$ unique CBHCVs with $U' = 28$ unique compressed codewords having a corresponding

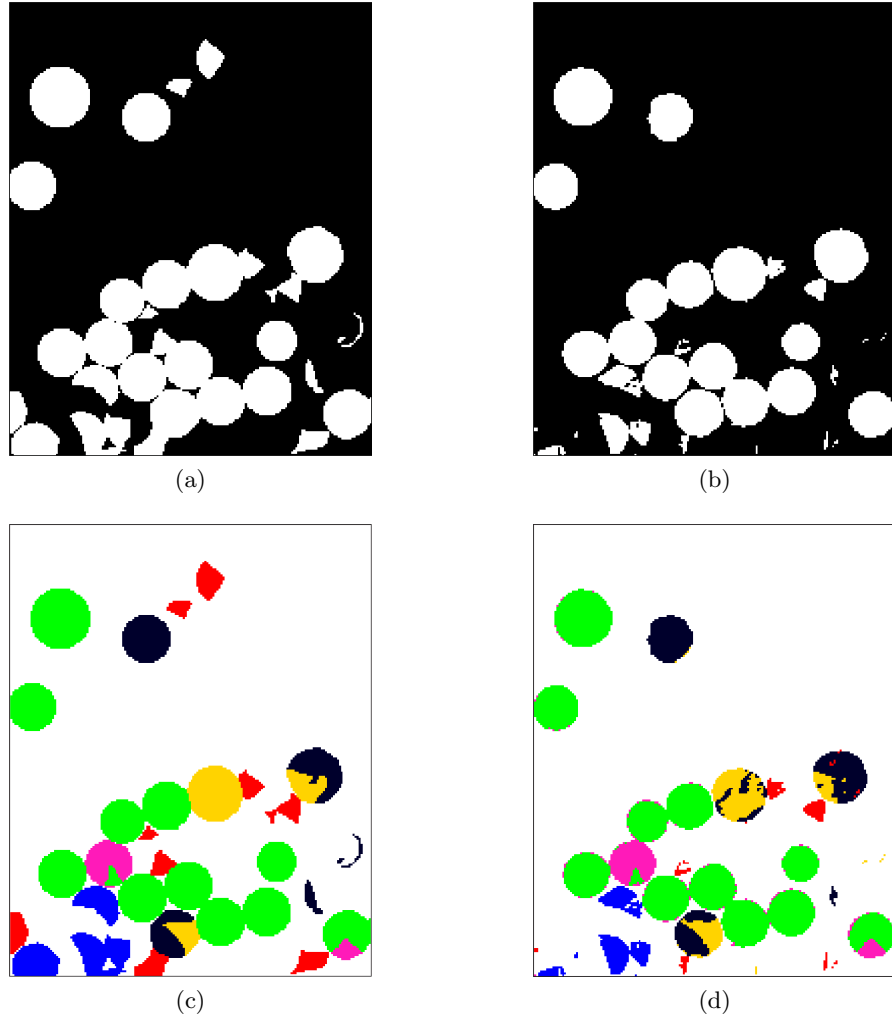


Figure 4.9: CD results for the BentonRM dataset: (a) reference binary CD map, (b) proposed method binary CD map, (c) reference multiple CD map, (d) proposed method multiple CD map.

Table 4.2: Quantitative results comparison among the proposed method, the S^2CVA and the BS-SVM for the simulated and BentonRM datasets.

Dataset	OA[%]		\mathcal{K}_c	
	Simulated	BentonRM	Simulated	BentonRM
Proposed Method	99.88	94.55	0.99	0.91
S^2CVA [155]	99.99	94.37	0.99	0.91
BS-SVM [118]	–	96.92	–	0.95

Table 4.3: Confusion matrix for the multiple CD results of the BentonRM dataset.

		Ground Truth						
		ω_u	ω_1	ω_2	ω_3	ω_4	ω_5	ω_6
Proposed Method	ω_u	30564	502	829	455	178	29	55
	ω_1	0	532	0	0	0	0	0
	ω_2	1	0	218	0	11	0	1
	ω_3	5	0	0	4509	0	5	0
	ω_4	1	0	1	0	1029	0	221
	ω_5	4	0	0	147	0	445	0
	ω_6	4	0	0	0	43	0	711

prior probability $P_u > T_P$. Therefore, the hierarchical clustering algorithm was applied only to 28 codewords. The $U' = 28$ unique CBHCVs represent the 99.3% of the total number of changed samples, thus showing that the coding step effectively represents the change information. The analysis of the CD map showed that the method can discriminate between all the kinds of change in an unsupervised and automatic way with an Overall Accuracy (OA) of 99.98% and a $\mathcal{K}_c = 0.99$. The S²CVA provided similar performances but relying on a supervised and non-automatic analysis. Table 4.2 shows the numerical results for the simulated dataset. The very high accuracy is motivated by the fact that the simulation does not fully captures all the challenges that have to be addressed when dealing with real HS data.

In the BentonRM dataset, the binary CD achieved an OA of 94.91% and a \mathcal{K}_c coefficient of 0.85. The method converted the $N = 7888$ HCVs into BHCVs composed by $I = 393$ bits, which were then compressed into CBHCVs having a length $J = 25$ bits. $U = 574$ unique CBHCVs were identified and the hierarchical clustering was applied to $U' = 107$ CBHCVs. The $U' = 107$ CBHCVs represent the 87.2% of the changed samples. This confirms that the coding step effectively represents in an efficient way the change information. Indeed, we are representing most of the changed samples with few binary codewords. The remaining samples (i.e., 12.8%) are not used in the construction of the dendrogram, since they are likely to be noisy samples. They are nevertheless assigned to one of the kinds of change after the change classes are identified.

Figure 4.9 shows the results in terms of binary and multiple CD obtained by the proposed method compared with the reference map. Table 4.3 shows the confusion matrix of the multiple CD for the proposed approach. Most of the samples correctly identified as changed have been assigned to the correct change class. The multiple CD achieved an OA of 94.55% and a \mathcal{K}_c coefficient of 0.91. Table 4.2 shows a quantitative comparison between the proposed method, the S²CVA [155] and the BS-SVM [118]. The proposed method achieved a slightly higher accuracy compared to the S²CVA despite being completely automatic. The BS-SVM reached a modestly higher accuracy (+2.4%). However, note that this method is supervised and requires bitemporal reference samples to train the SVM. Thus the proposed unsupervised method is competitive with state-of-the-art

supervised methods.

Let us consider the entire Benton County dataset. The visual analysis of the binary Change Detection map shows that changes are identified with high accuracy with only few false alarms due to outliers in the HCV image and residual registration errors. Also some missed alarms are present but they correspond to changes with low magnitude. The quantization and codeword definition steps converted the $N = 11965$ changed HCVs into BHCVs composed by $I = 375$ bits and the compression generated CBHCVs with $J = 27$ bits. $U = 681$ unique CBHCVs were identified with only $U' = 106$ compressed codewords with a prior probability $P_u > T_p$. The selected 106 unique CBHCVs represent 10544 of the 11965 samples (i.e., 88%).

Figure 4.10 shows the CD results for the second dataset. Figures 4.10a-4.10c show the CD maps obtained by cutting the dendrogram at different depths. The figures show that by decreasing (moving from Figure 4.10a to 4.10c) the depth value T_δ , it is possible to discriminate among an increasing number of changes. The scatter plots (Figures 4.10e-4.10g) point out that the discrimination into different kinds of change is made consistently for almost all the changes since most of the clusters show little overlapping between each other. Figure 4.10d shows the CD map obtained by the manual identification of the S²CVA, which identified 8 changes. The change maps obtained by the proposed automatic method (Figure 4.10b) and the manual S²CVA (Figure 4.10d) are very similar, with large portion of the data showing the same kinds of change in both images.

Figure 4.11 shows three details (d_1, d_2, d_3) of the CD maps of Figure 4.10 together with false color composition of the HCV difference image. The images show that when the dendrogram is cut to obtain 4 clusters we identify one kind of change in each field. The false color compositions of the difference image in Figure 4.11 highlight that more than one kind of change is present in the selected fields. The Figures related to details d_1 and d_3 show that by increasing the sensitivity of the method we increase the sensitivity to the different kinds of change and we can separate subtle changes in uniform areas. In contrast, the Figures regarding detail d_2 show that when the sensitivity of the method goes above a given threshold, the noise in the CD map becomes significant ($V = 15$). However, note that the false color composition of the difference image of d_2 shows that in the considered field there is a high probability of having more than 2 changes. The S²CVA CD map show similar results to the proposed method for details d_2 and d_3 . However, note that for detail d_1 the S²CVA identifies only two different changes, whereas the proposed method identifies all the changes of the considered field (as confirmed also by the false color composition). This analysis points out that while increasing the sensitivity allows us to discriminate between more kinds of change, this comes at the cost of an increase in the vulnerability of the method to noise and outliers. In other words, after a given value of T_δ , as expected the method starts to identify the noisy samples as different changes.

In the Albacete dataset, a visual analysis of the binary CD map shows a slightly higher percentage of missed and false alarms with respect to the second dataset. This is due to the overlapping of changed and unchanged statistical distributions in the magnitude of the difference image. The $N = 33693$ samples were converted into BHCVs composed by $I = 372$ bits, which were then compressed into $J = 28$ bits to obtain the CBHCVs. The CBHCVs analysis selected $U = 2382$ unique CBHCVs and $U' = 150$ codewords

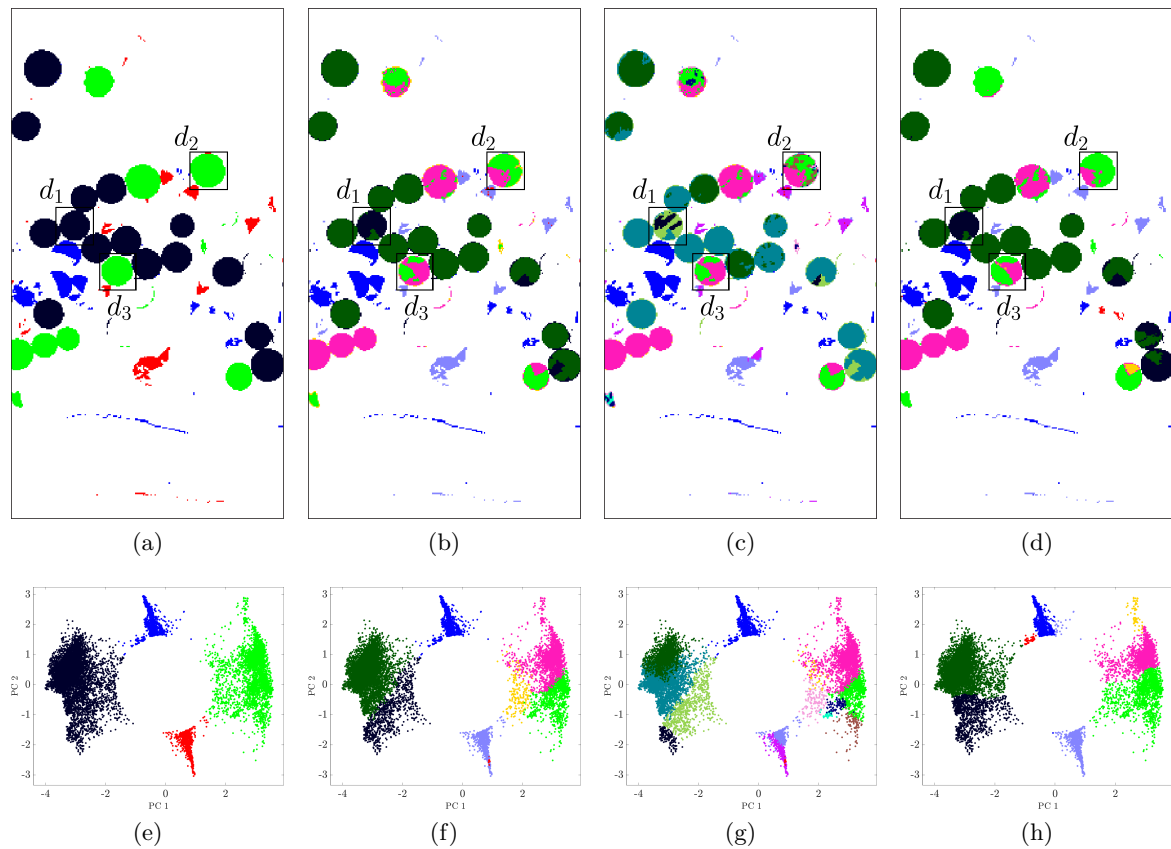


Figure 4.10: CD results for the Benton dataset: CD maps obtained by cutting the dendrogram at a depth to obtain (a) $V = 4$, (b) $V = 8$, (c) $V = 15$. (d) S^2CVA map with 8 identified changes. 2-D scatter plots representing the first two components of the Principal Component Analysis of the HCVs (in the original representation) of the changed samples: the plots represent the (e) 4, (f) 8, (g) 15 (g), (h) 8 (S^2CVA) clusters. Each color represents a kind of change ω_v , whereas white identifies the no changed areas.

with a prior probability greater than T_P . The U' represented 25150 of the 33693 samples (i.e., 74.6%). This confirms the results of the Benton dataset regarding the efficient representation of the change information.

Figure 4.12 shows the CD maps and the corresponding scatter plots for the Albacete dataset. The maps (Figures 4.12a-4.12c) show that the proposed method discriminates consistently among the different kinds of change since most of the changed areas show homogeneous spatial behaviour. This is also confirmed by the scatter plots (4.12e-4.12h) with the identified cluster showing little overlapping between each other. Figure 4.12d shows the CD map obtained with the manual iterative S^2CVA which identified 11 changes. By comparing it with the map of the proposed method with $V = 11$ (Figure 4.12b), it is possible to see that there is a large number of fields that show the same change pattern in the two maps. However, there are also some fields that show different change patterns. In some cases, this is due to the fact that the selected sensitivity does not allow to identify

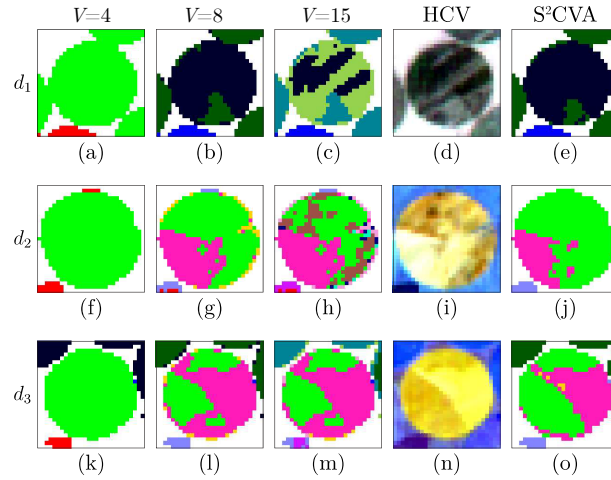


Figure 4.11: Details of the CD maps of the Benton dataset (Figures 4.10a-4.10c): (a-c) detail d_1 . (f-h) Detail d_2 . (k-m) Detail d_3 . False color composites of the HCV image representing detail (d) d_1 (R: 823.65 nm, G: 972.99 nm, B: 1053.69 nm), (i) d_2 (R: 844 nm, G: 1225.17 nm, B: 1689.3 nm), (n) d_3 (R: 1053.69 nm, G: 1336.15 nm, B: 548.92 nm), respectively. Details of the S²CVA map (Figure 4.10d): (e) detail d_1 , (j) detail d_2 , (o) detail d_3 .

some changes. This is the case of detail d_3 in Figure 4.13. The false color composition of the difference image points out that the lower portion of the field shows two different changes. These changes are correctly identified by the S²CVA. Note that by increasing the sensitivity, the proposed method correctly identifies the considered changes (Figure 4.13m). A similar analysis can be done for the detail d_1 . Another cause of these differences is related to the complexity of this bitemporal dataset. Compared to the Benton dataset, the Albacete dataset is a much more complex dataset since the changes are much less separable. This can lead to errors in the CD maps of the proposed method but also in that of the S²CVA since the manual selection of the changes can not be performed accurately due to the difficulties in identifying the boundaries of the different changes. As an example, let us consider detail d_2 shown in Figure 4.13. The false color composition of the HCV image shows a complex spatial pattern. The CD maps of the proposed method separates correctly the different changes when the sensitivity of the method is increased. In contrast, the S²CVA map shows only one kind of change.

4.4 Conclusion

In this work we proposed a method for CD in HS images. HS data are characterized by a rich information content due to the dense sampling of the spectrum. This comes at a cost of having to deal with much more complex data, due to the high dimensionality and redundancy. These factors make the extraction of the change information more complex with respect to MS data, thus increasing the difficulty in discriminating between different kinds of change. In this work we developed a technique that aims at extracting from the individual spectral channels the relevant information for the CD problem. In greater

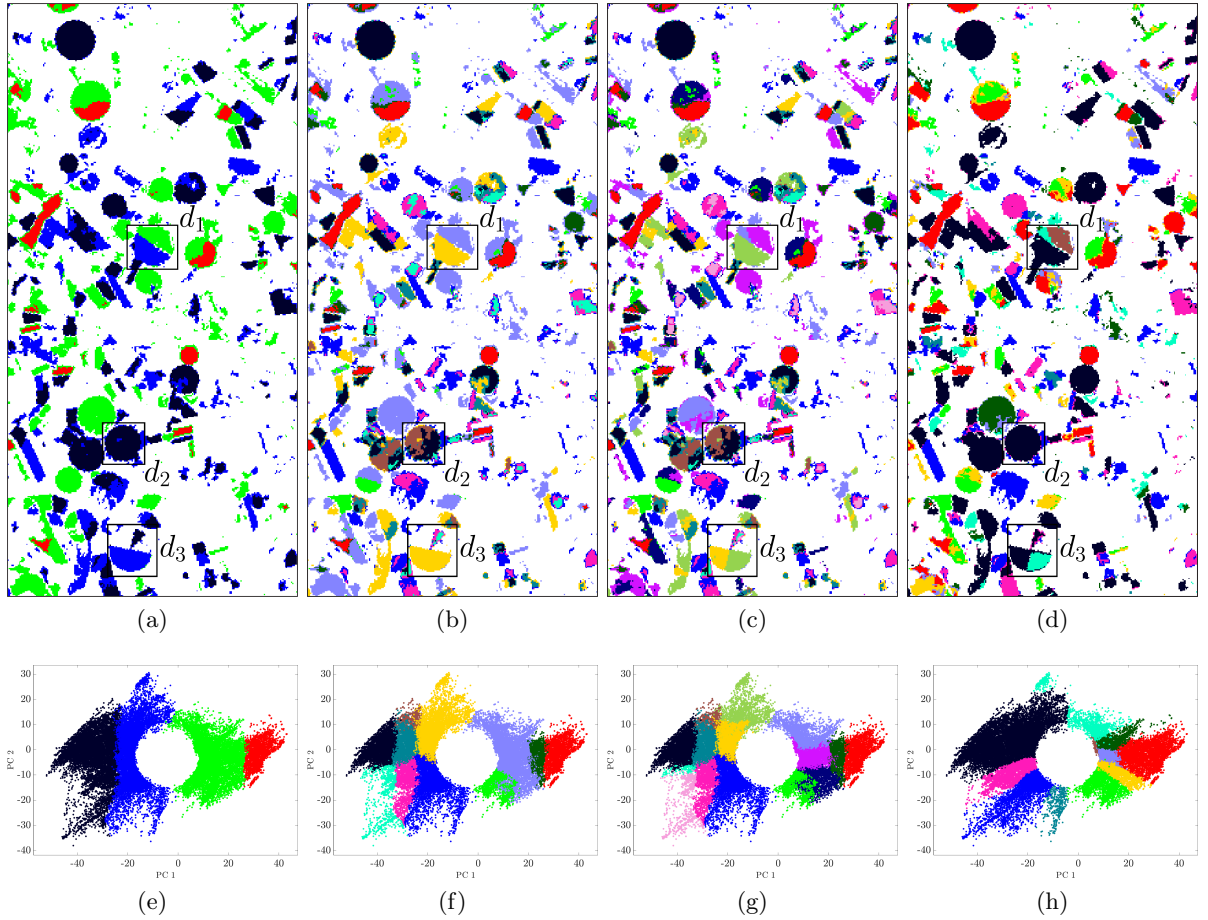


Figure 4.12: CD results for the Albacete dataset: CD maps obtained by cutting the dendrogram at a depth to obtain (a) $V = 4$, (b) $V = 11$, (c) $V = 15$. (d) S^2CVA map with 11 identified changes. 2-D scatter plots representing the first two components of the Principal Component Analysis of the HCVs (in the original representation) of the changed samples: the plots represent the (e) 4, (f) 11, (g) 15 (g), (h) 11 (S^2CVA) clusters. Each color represents a kind of change ω_v , whereas white identifies the no changed areas.

detail, after a binary CD, we focus on the changed samples to move from the real valued representation of the HCVs to a codeword based representation. After the coding of the HCVs, we select only the unique CBHCVs with a prior probability higher than a given threshold thus reducing the number of elements to be processed in the following steps. Finally, we apply the agglomerative hierarchical clustering to the selected unique CBHCVs thus obtaining a dendrogram. The dendrogram can be cut to discriminate between the different kinds of change.

The sensitivity analysis on the selection of the values of T_η and T_P showed that the method reaches similar accuracies for a wide range of combinations thus proving that is robust to the variation of these parameters. The HCVs coding proved to be an effective way of simplifying the CD problem by highlighting the relevant change information. This

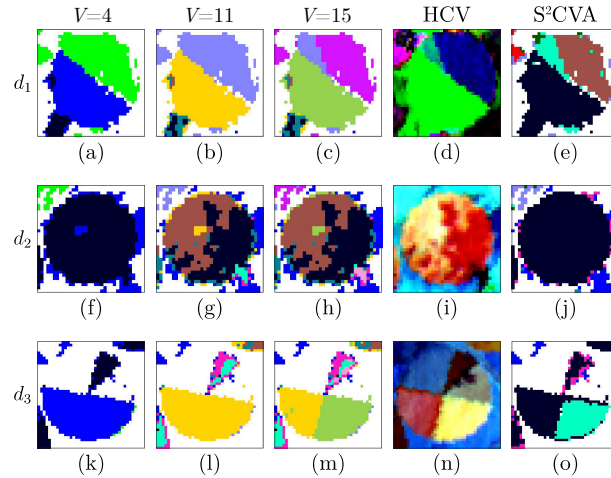


Figure 4.13: Details of the CD maps of the Albacete dataset (Figures 4.12a-4.12c): (a-c) detail d_1 . (f-h) Detail d_2 . (k-m) Detail d_3 . False color composites of the HCV image representing detail (d) d_1 (R: 660.85 nm, G: 833.83 nm, B: 2183.63 nm), (i) d_2 (R: 833.83 nm, G: 538.74 nm, B: 1669.1 nm), (n) d_3 (R: 833.83 nm, G: 1235.27 nm, B: 1669.1 nm), respectively. Details of the S^2CVA map (Figure 4.12d): (e) detail d_1 , (j) detail d_2 , (o) detail d_3 .

was confirmed by the fact that, for all the datasets, a small set of unique CBHCVs represented most of the changed samples. This allowed us to construct the dendrogram using a very small number of samples while preserving almost all the relevant change information. The numerical results obtained on the simulated dataset ($\mathcal{K}_c = 0.99$) and on the BentonRM dataset ($\mathcal{K}_c = 0.91$) showed that the proposed binary codewords representation can be used to discriminate between different changes. Compared to the S^2CVA , the proposed method obtained a slightly lower value of OA for the simulated dataset, whereas for the BentonRM it slightly increased the OA and \mathcal{K}_c . The BS-SVM yielded a higher accuracy compared to the proposed method. However, note that unlike the proposed approach, the S^2CVA is not an automatic method and requires the manual identification of the changes while the BS-SVM requires the availability of bitemporal training samples which are seldom available. The numerical results proved that the proposed unsupervised and automatic approach is competitive with supervised methods and methods based on the manual identification of the changes. The qualitative analysis of the CD maps of the Benton and Albacete datasets confirmed that the proposed method identifies the different changes with a high accuracy. Moreover, the tree structure representation allows us to produce multiple CD maps with different levels of details. The possibility of changing the sensitivity to the different kinds of change showed that the proposed approach can produce different CD maps depending on the selected sensitivity. It is worth noting that a trade-off between sensitivity to changes and sensitivity to noise, outliers and errors generated in the coding step should be obtained. When the depth of the cut T_δ is too small, outliers may be identified as a separate kind of change.

As future developments we plan to: i) consider the spatial context information in the process of detection and discrimination of changes; ii) integrate the binary CD in the coding process in order to reduce missed and false alarms; iii) use advanced information

theory techniques to optimize the compression of the binary codewords to reduce the redundant information; and iv) test the proposed method on other bitemporal HS data and on more real datasets for which bitemporal reference maps are available (still difficult to obtain).

Chapter 5

Methods for the Fusion of Multitemporal LiDAR Data for Individual Tree Characterization

This Chapter ¹ presents two novel approaches for the fusion of bitemporal LiDAR data to improve the analysis and characterization of individual tree. The first method uses bitemporal data to: i) improve the individual tree detection of both dates, and ii) identify forest changes at single-tree level. This is done by using a compound approach to the tree detection based on the Bayes rule for minimum error to model the temporal dependence between the LiDAR acquisitions. The second approach uses medium density LiDAR point clouds to improve single-tree parameters estimation on low density data. The approach first focuses on the accurate characterization of the crown shapes in the high density data using a parametric model. Then, it uses the obtained estimates to drive the tree parameters estimation on the low density LiDAR data. To this end, it considers multitemporal assumptions about how the tree parameters change in time. Experimental results on bitemporal datasets acquired in the Italian Alps confirmed the effectiveness of the two methods reducing the number of errors in the detection of the tree-tops and improving the accuracy of the crown parameters estimates.

5.1 Introduction

The analysis of individual trees requires a precise detection and an accurate characterization of their canopies. The tree identification can be split into two steps: i) detection of the tree-tops and ii) the delineation of the individual tree-crowns. This Chapter is focused on tree detection and characterization. Several methods have been proposed for

¹Part of this Chapter appears in:

[J4] D. Marinelli, C. Paris, L. Bruzzone, "A Novel Data Fusion Approach to Compound Tree Detection in Multitemporal LiDAR Data," in *IEEE Geoscience and Remote Sensing Letters*, in press.

[C5] D. Marinelli, C. Paris and L. Bruzzone, "Fusion of Multitemporal LiDAR Data for Individual Tree Crown Parameter Estimation on Low Density Point Clouds," *2018 IEEE International Geoscience and Remote Sensing Symposium (IGARSS)*, Valencia, Spain, 2018, pp. 3999-4002.

tree identification [10, 55, 175, 178, 180, 213–217]. A common approach to identify the tree-tops is to search for the peaks in the CHM using the Level Set Method (LSM) [178] or maximum filtering [10, 180, 216]. Other techniques perform both tree-top detection and crown delineation in one step using classification based approaches [215], clustering [55, 217], segmentation algorithms [175, 213] or wavelet analysis [214].

The characterization of an individual tree requires the computation of parameters that describe its crown such as top height, base height and crown radius. This can be done by extracting the parameters directly from the point cloud [37, 181, 218, 219] or by reconstructing the shape of the tree-crown and computing the parameters on the reconstructed shape. The reconstruction can be performed in a parametric way using either models suitable for coniferous trees [53, 182, 183, 220] or more general models, like superquadrics, that can be used also for broadleaved trees [221]. Possible non parametric approaches are the convex hull [217, 222] or alpha shape [223–225]. These methods works using single-date data. However, since repeated acquisitions are now taken more and more frequently at large scale, it is important to exploit bitemporal data not only to perform change detection and study forest dynamics but also to improve forest analysis at a given single-date. While in recent years medium (e.g., 10 pulses/m²) and high pulse density (≥ 20 pulses/m²) data are typically acquired, older data may be characterized by low pulse densities (≤ 5 pulses/m²). While at plot scale different pulse densities do not heavily impact on the estimation of forest attributes [226], single-tree level analysis is strongly affected by low pulse density acquisitions. In particular, unrealistic or wrong estimates of the tree parameters may be obtained as pulse density decreases [183, 227]. This limits the use of old datasets for performing single-tree analysis. In this context, it is extremely important to define methods that can take full advantage of the bitemporal acquisitions to improve the forest analysis at single-date. This is to allow for the use of older dataset in single-tree analysis thus significantly expanding the areas where single-tree information is available. Moreover, this could expand also the areas where CD at the single-tree level can be performed exploiting older data together with the new acquisitions. To this end, we aim to define methods capable of fusing the information of bitemporal point clouds with different pulse densities. Note that this has to be done carefully in order to preserve the information content of the low density point cloud and therefore the multitemporal information.

This Chapter presents two approaches that exploit the bitemporal information to improve the single-tree analysis. The first method is a data fusion approach to compound tree detection that takes advantage of the bitemporal information to: i) improve the accuracy of the tree detection performed at each single-date and ii) detect the presence of large forest changes at individual tree level. This is done by first separately detecting the trees at both dates. Then, for each tree detected at least at one date, we perform a morphological analysis to extract geometric features from both scenes. Finally, a Bayesian compound decision rule approach is used to estimate the probability that candidate trees are correctly identified in each LiDAR acquisition.

The second method, which is presented in the second part of the Chapter, addresses the fusion of bitemporal point clouds for individual tree-crown parameters estimation on low density point clouds. It aims to improve the tree parameters estimated on the low density

LiDAR data by using the detailed information from the higher density one, while taking into account the temporal shift. The crown parameters are estimated by reconstructing the shape of the tree using a 3-D model. First, the higher density LiDAR data are used to characterize the individual tree-crowns to accurately model the shape of the trees (e.g., crown location, crown boundaries, etc.) and estimate the related parameters. The estimated parameters are then used to guide the estimation on the low density point clouds taking into account the temporal shift.

The rest of the Chapter is organized in two main parts. Section 5.2 presents the data fusion approach to compound tree detection and the related experimental results. Section 5.3 illustrates the method for individual tree-crown parameters estimation on low density point clouds and shows the related experimental results. Section 5.4 draws the conclusion of the Chapter.

5.2 Proposed Method for Compound Tree Detection

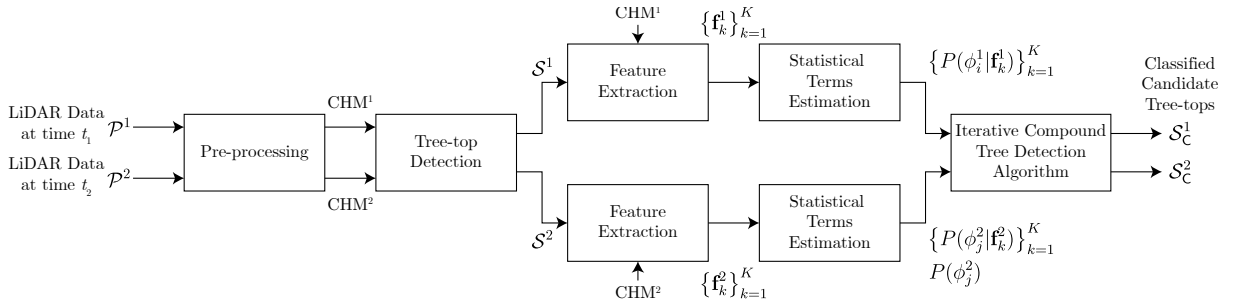


Figure 5.1: Block scheme of the proposed compound method for tree-top detection.

Figure 5.1 shows the block scheme of the proposed method. After the pre-processing which includes co-registration and regularization, the candidate tree-tops are detected in the two CHMs. Then, relevant geometrical features are extracted separately at both dates for each candidate tree-top to estimate the statistical terms for the compound detection. These terms are then used in the iterative compound detection to define the new sets of classified candidate tree-tops.

Let us consider two Canopy Height Model (CHM) images CHM^1 and CHM^2 derived from the LiDAR point clouds acquired at different times t_1 and t_2 , respectively, and representing the same geographical area. Let us assume that the two point clouds are co-registered using the method presented in Chapter 3 and that the tree-top detection has been already performed on both the CHMs. In the considered implementation, we applied a LSM [178] to each CHM to detect the trees present in the scene. However, any other method can be employed. Let $\{\mathbf{s}_{k^1}^1\}_{k^1=1}^{K^1}$ and $\{\mathbf{s}_{k^2}^2\}_{k^2=1}^{K^2}$ be the set of identified candidate tree-tops in CHM^1 and CHM^2 , respectively, where each tree-top is defined by a (x, y) position (i.e., pixel position). The candidate tree-tops are fused considering the distance based criterion proposed in Chapter 3:

$$\mathbf{s}_{k^2}^2 : k^2 = \underset{k^2 \in \{1, \dots, K^2\}}{\operatorname{argmin}} \left\| \mathbf{s}_{k^2}^2 - \mathbf{s}_{k^1}^1 \right\|. \quad (5.1)$$

Also in this case we consider a threshold T_s to avoid false matching. The pairs of fused tree-tops are added to the two set of candidate tree-tops \mathcal{S}^1 and \mathcal{S}^2 . Note that differently from Chapter 3, here we analyze more in detail the candidate tree-tops for which no candidate tree-top has been identified at the other date. In particular, these cases can be: i) trees that have been identified at one date and missed at the other one, ii) trees that have been cut or planted between the two dates or iii) false alarms. Therefore, these candidate tree-tops should be analyzed at both dates to understand to which case they correspond. To this end, each candidate tree-top for which no match is found at the other date is added to both \mathcal{S}^1 and \mathcal{S}^2 . The results of these operations are two set of fused candidate tree-tops $\mathcal{S}^1 = \{\mathbf{s}_k^1\}_{k=1}^K$ and $\mathcal{S}^2 = \{\mathbf{s}_k^2\}_{k=1}^K$ where $K \geq \max\{K^1, K^2\}$.

5.2.1 Bayesian Framework to Compound Tree Detection

The proposed method aims at using a compound approach to improve the tree detection by analyzing the sets of fused candidate tree-tops \mathcal{S}^1 and \mathcal{S}^2 . Compared to the tree-top fusion approach proposed in Chapter 3, this work aims at better exploiting the bitemporal information using a compound approach and to identify large forest changes. In particular, the main aim of this approach is to automatically decide if a pixel \mathbf{s}_k^t , ($t = 1, 2$) identified as a tree-top by [178] is actually a tree-top or if it is related to a cut or a planted tree or a false alarm using the bitemporal information. Let $\Phi = \{\phi_0^t, \phi_1^t\}$, ($t \in \{1, 2\}$) be the set of possible classes at time t_1 and t_2 , where ϕ_0^t and ϕ_1^t indicate that a pixel (i.e., a \mathbf{s}_k^t) is classified as tree-top and as non tree-top (at time t), respectively. Note that a change (e.g., cut trees, forest regrowth or tree planting) is detected if the same pixel is classified with different labels in CHM^1 and CHM^2 . Let us focus the attention on the k th pair of candidate tree-top pixels ($\mathbf{s}_k^1, \mathbf{s}_k^2$) described by the sets of features ($\mathbf{f}_k^1, \mathbf{f}_k^2$). The Bayesian decision rule for compound classification identifies the optimal pair of labels (ϕ_b^1, ϕ_e^2), (with $b, e \in \{0, 1\}$) by maximizing the joint probability considering their temporal correlation:

$$\begin{aligned} (\mathbf{s}_k^1, \mathbf{s}_k^2) \in (\phi_b^1, \phi_e^2) \text{ if} \\ (\phi_b^1, \phi_e^2) = \underset{\phi_i^1 \in \Phi, \phi_j^2 \in \Phi}{\operatorname{argmax}} \{P(\phi_i^1, \phi_j^2 | \mathbf{f}_k^1, \mathbf{f}_k^2)\}, \end{aligned} \quad (5.2)$$

where $P(\phi_i^1, \phi_j^2 | \mathbf{f}_k^1, \mathbf{f}_k^2)$ is the joint conditional posterior probability of the pair of classes (ϕ_i^1, ϕ_j^2) given the feature vectors of the candidate tree-tops ($\mathbf{f}_k^1, \mathbf{f}_k^2$). The pair of classes (ϕ_b^1, ϕ_e^2) that maximizes (5.2) is the same that maximizes:

$$(\phi_b^1, \phi_e^2) = \underset{\phi_i^1 \in \Phi, \phi_j^2 \in \Phi}{\operatorname{argmax}} \left\{ \frac{p(\mathbf{f}_k^1, \mathbf{f}_k^2 | \phi_i^1, \phi_j^2) P(\phi_i^1, \phi_j^2)}{p(\mathbf{f}_k^1, \mathbf{f}_k^2)} \right\}, \quad (5.3)$$

where the joint density $p(\mathbf{f}_k^1, \mathbf{f}_k^2)$ can be neglected since it is not dependent on (ϕ_i^1, ϕ_j^2). $P(\phi_i^1, \phi_j^2)$ is the joint prior probability of having ϕ_i^1 at time t_1 and ϕ_j^2 at t_2 in CHM^1 and CHM^2 , respectively. In the considered tree-top detection problem, it is reasonable to assume temporal class conditional independence since the feature vector \mathbf{f}_k^t depends mainly on the characteristics of the CHM at time t . This allows us to rewrite

$p(\mathbf{f}_k^1, \mathbf{f}_k^2 | \phi_i^1, \phi_j^2) = p(\mathbf{f}_k^1 | \phi_i^1) p(\mathbf{f}_k^2 | \phi_j^2)$ where $p(\mathbf{f}_k^1 | \phi_i^1)$ and $p(\mathbf{f}_k^2 | \phi_j^2)$ are the single-date class conditional density functions. The estimation of the joint conditional posterior probability is therefore simplified and (5.3) can be rewritten as:

$$(\phi_b^1, \phi_e^2) = \underset{\phi_i^1 \in \Phi, \phi_j^2 \in \Phi}{\operatorname{argmax}} \{p(\mathbf{f}_k^1 | \phi_i^1) p(\mathbf{f}_k^2 | \phi_j^2) P(\phi_i^1, \phi_j^2)\}. \quad (5.4)$$

Note that the joint prior probability can be rewritten as:

$$P(\phi_i^1, \phi_j^2) = P(\phi_j^2 | \phi_i^1) P(\phi_i^1), \quad (5.5)$$

where $P(\phi_i^1)$ is the prior probability of class ϕ_i at time t_1 . The class conditional density functions can be rewritten as:

$$\begin{aligned} p(\mathbf{f}_k^1 | \phi_i^1) &= \frac{P(\phi_i^1 | \mathbf{f}_k^1) p(\mathbf{f}_k^1)}{P(\phi_i^1)} \\ p(\mathbf{f}_k^2 | \phi_j^2) &= \frac{P(\phi_j^2 | \mathbf{f}_k^2) p(\mathbf{f}_k^2)}{P(\phi_j^2)}. \end{aligned} \quad (5.6)$$

$p(\mathbf{f}_k^1)$ and $p(\mathbf{f}_k^2)$ do not depend on ϕ_i^1 and ϕ_j^2 and therefore can be neglected. By substituting (5.5) and (5.6) into (5.4) we obtain the following decision rule:

$$(\phi_b^1, \phi_e^2) = \underset{\phi_i^1 \in \Phi, \phi_j^2 \in \Phi}{\operatorname{argmax}} \left\{ \frac{P(\phi_i^1 | \mathbf{f}_k^1) P(\phi_j^2 | \mathbf{f}_k^2) P(\phi_j^2 | \phi_i^1)}{P(\phi_j^2)} \right\}. \quad (5.7)$$

Note that the considered compound approach has been widely employed to classify bitemporal images [197–199]. To apply the Bayesian decision rule for compound classification, we need to estimate all the terms involved in (5.7) in an unsupervised way. In the considered implementation, we estimate $P(\phi_j^2)$, $P(\phi_i^1 | \mathbf{f}_k^1)$ and $P(\phi_j^2 | \mathbf{f}_k^2)$ on the basis of a model translated in a set of rules which are applied to the feature vectors $(\mathbf{f}_k^1, \mathbf{f}_k^2)$. $P(\phi_j^2 | \phi_i^1)$ is estimated using an iterative algorithm which does not require any *a priori* knowledge about probabilities of transition. The rule-based estimation approach is described in the next subsection.

5.2.2 Rule-Based Approach to the Estimation of Statistical Terms

Although LiDAR data allow for accurate tree-top identification results, errors are unavoidable as for instance upper branches may lead to false local maxima (i.e., commission errors) and low density data may lead to missed trees (i.e., omission errors). Moreover, LiDAR data acquired with different pulse densities produce different tree-top detection results due to the different irregular sampling of the LiDAR pulses. In this context, some tree-tops may be better detected in a date with respect to the other. To model each candidate tree-top, we use a feature vector describing the geometric characteristics of the tree-tops identified in the CHMs. For each tree-top, we analyze the geometric behavior of its profile in the CHM along the four main directions (0° , 45° , 90° , 135°) in the (x, y) plane centered in the tree-top position. We work in the CHM domain in order to be more

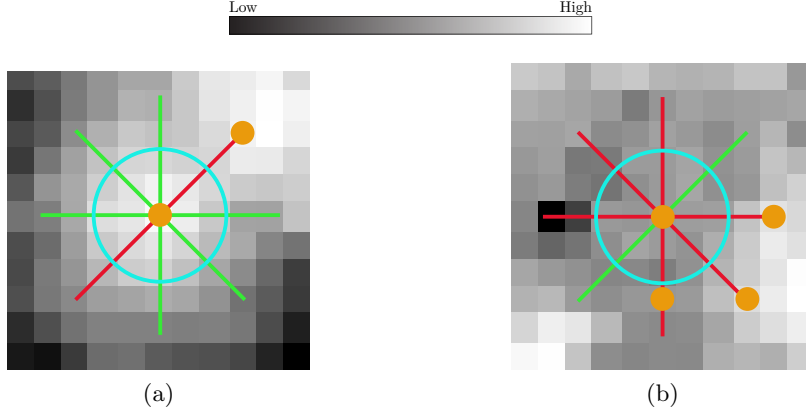


Figure 5.2: Example of features extraction for: (a) true tree-top; (b) false tree-top. The lines represent the 4 profiles and the orange dots represent position of the maximum along each profile. The blue circle has a radius equal to T_β . The lines are red if $\beta_{k,l}^t > T_\beta$ and green if $\beta_{k,l}^t \leq T_\beta$. In (a) 3 out of the 4 maximum positions correspond to the tree-top location, whereas in (b) only 1 out of the 4 maximum positions correspond to the tree-top location.

robust to the irregular sampling of LiDAR data. For each direction, the profile is defined as the values of the CHM along the line. Then, the 1-D distance between the tree-top position and the position of the maximum value (i.e., maximum height of the CHM along the profile) of the considered profile is computed. Let $\mathbf{f}_k^t = \{\beta_{k,l}^t\}_{l=1}^4$ be the feature vector of distances for the k th tree, extracted separately at time t_1 and t_2 . Figure 5.2 shows the feature extraction where for each profile, $\beta_{k,l}^t$ is computed as the distance of the orange dot from the center. To estimate the prior and the posterior probabilities of the classes (ϕ_i^1, ϕ_j^2) at time t_1 and t_2 we use a set of rules applied to \mathbf{f}_k^1 and \mathbf{f}_k^2 , respectively. A measure of the likelihood that \mathbf{s}_k^t is a tree-top is computed according to the following empirical rule:

$$\gamma_k^t = \begin{cases} 0.1 & \alpha = 0 \\ \alpha 0.25 & 1 \leq \alpha \leq 4 \end{cases}, \text{ with } \alpha = |\{l : \beta_{k,l}^t \leq T_\beta\}|, \quad (5.8)$$

where $|\cdot|$ is the cardinality of the set (in this case the number of indexes l for which the corresponding $\beta_{k,l}^t$ satisfies the condition) and T_β is a threshold on the distance $\beta_{k,l}^t$. The number of directions that satisfy the condition $\beta_{k,l}^t \leq T_\beta$ indicates how much the maximum of the candidate tree-top is prominent considering the possible others surrounding maxima. In Figure 5.2a (true tree-top) 3 profiles satisfy the condition ($\gamma_k^t = 0.75$), whereas in Figure 5.2b (false tree-top) only one profile satisfies it ($\gamma_k^t = 0.25$). We empirically use the likelihood as an approximation of the posterior probabilities, i.e.,:

$$\begin{aligned} P(\phi_0^t | \mathbf{f}_k^t) &= \gamma_k^t \\ P(\phi_1^t | \mathbf{f}_k^t) &= 1 - \gamma_k^t. \end{aligned} \quad \forall k = 1, \dots, K, t = 1, 2 \quad (5.9)$$

According to the considered set of rules, the prior probabilities can be estimated as:

$$\begin{aligned} P(\phi_0^2) &= \frac{|k : \gamma_k^2 \geq T_\gamma|}{K} \\ P(\phi_1^2) &= \frac{|k : \gamma_k^2 < T_\gamma|}{K}, \end{aligned} \quad (5.10)$$

where T_γ is a threshold on the likelihood.

5.2.3 Iterative Compound Tree Detection Algorithm

In this step we estimate the elements of the following 2×2 matrix of probabilities of transition:

$$M = \begin{bmatrix} P(\phi_0^2|\phi_0^1) & P(\phi_1^2|\phi_0^1) \\ P(\phi_0^2|\phi_1^1) & P(\phi_1^2|\phi_1^1) \end{bmatrix}, \quad (5.11)$$

where the matrix element m_{ij} represents the probability that a pixel belongs to the class ϕ_i^1 at time t_1 and to the class ϕ_j^2 at time t_2 . Note that $P(\phi_0^2|\phi_0^1)$ models the probability that a tree detected in CHM^1 is still a tree in CHM^2 , $P(\phi_0^2|\phi_1^1)$ models the appearance of new trees, $P(\phi_1^2|\phi_0^1)$ represents the probability that a tree is no more present in CHM^2 (e.g., forest cut) and $P(\phi_1^2|\phi_1^1)$ models the probability of a candidate tree-top of being a false alarm at time t_2 given that it is a false alarms also at time t_1 . To estimate the probabilities of transition from the bitemporal LiDAR dataset under analysis, we considered the following iterative procedure:

Initialization: The posterior probabilities $P(\phi_i^1|\mathbf{f}_k^1)$ and $P(\phi_j^2|\mathbf{f}_k^2)$ and the prior probability $P(\phi_j^2)$ are estimated according to the approach described in 5.2.2. For the initialization we assume the independence between the classes ϕ_j^2 , ($j \in \{0, 1\}$) at time t_2 and ϕ_i^1 ($i \in \{0, 1\}$) at time t_1 . Accordingly, the probabilities of transition is initialized as follows:

$$M^0 = \begin{bmatrix} P(\phi_0^2) & P(\phi_1^2) \\ P(\phi_0^2) & P(\phi_1^2) \end{bmatrix}, \quad (5.12)$$

where the apex 0 indicates the initial iteration. By considering the above initialization, the compound classification results in the assignment of the label $\in \{\phi_0^t, \phi_1^t\}$, ($t \in \{1, 2\}$) that maximizes Equation (5.7) for each \mathbf{s}_k^t , ($t \in \{1, 2\}$).

nth Iteration The result obtained at iteration $n-1$, can be used to compute the estimate of the probabilities of transition at iteration n , according to the following equation:

$$m_{ij}^n = \frac{|k : \mathbf{s}_k^1 \text{ assigned to } \phi_i^1 \wedge \mathbf{s}_k^2 \text{ assigned to } \phi_j^2|}{|k : \mathbf{s}_k^1 \text{ assigned to } \phi_i^1|}, \quad (5.13)$$

where \wedge is the *and* operator. Note that the estimates of $P(\phi_i^1|\mathbf{f}_k^1)$, $P(\phi_j^2|\mathbf{f}_k^2)$ and $P(\phi_j^2)$ do not change with the iterations. This is because their values are based on the feature vectors (as shown in 5.2.2) that do not vary with the iterations.

Stop Criterion The iterative compound tree detection algorithm stops when the largest difference among the estimates of all probabilities of transition between two consecutive iterations is lower than a certain threshold ϵ :

$$\max_{i \in \{0,1\}, j \in \{0,1\}} \{m_{ij}^n - m_{ij}^{n-1}\} < \epsilon. \quad (5.14)$$

At the end of the procedure, the compound detection assigns a class to each candidate tree-top in \mathcal{S}^1 and \mathcal{S}^2 thus obtaining the new sets \mathcal{S}_C^1 and \mathcal{S}_C^2 of classified candidate tree-tops. It is worth noting that the considered formulation allows us to detect: i) the presence of the tree-tops in the bitemporal CHMs separately, and ii) the forest changes at individual tree level.

5.2.4 Experimental Results

Experimental Setup

To evaluate the effectiveness of the proposed tree-top detection compound method, we considered a bitemporal airborne LiDAR dataset² acquired in a coniferous forest located at Parco Naturale Paneveggio - Pale di San Martino, Trento, Southern Italian Alps. The coordinates of the central point of the area are $46^\circ 17' 47,60''$ N, $11^\circ 45' 29,98''$ E. The area extends for 368 ha and the altitude ranges between 1536 m and 2065 m. The dominant species are Norway Spruce and Silver Fir. The first LiDAR survey was done specifically for forest analysis on September 4th, 2007 with the Optech ALTM3100EA instrument with a mean pulse density of 5 pulses/m². For each laser pulse four returns were recorded. A Digital Terrain Model (DTM) of the investigated area, with a spatial resolution of 1 m, was extracted from the LiDAR data and used to obtain the normalized point clouds. The second LiDAR survey was conducted over the whole province of Trento between October 2007 and December 2008 with an Optech ALTM 3100C. The pulse density was about 0.48 pulses/m². For each emitted pulse, both first and last returns were recorded.

The experimental analysis was conducted on 16 circular forest plots (20 m radius) randomly spread over the area, where ground data are available. These data have been extracted from field plots that have been acquired during forest inventory operations [228]. The center position of each circular plot was recorded using a Trimble Geo-CE XT GPS considering the average of more than 200 GPS acquisitions. Moreover, a differential correlation was applied to reach a residual uncertainty in the horizontal coordinates of the central point of 1.7 m. The relative position, with respect to the center of the corresponding sample plot, of all the trees with a DBH greater than 3 cm within the radius of the plot was recorded. In addition to the position, also the tree-top height and the tree species were recorded for each surveyed tree. Note that in this analysis we are considering only the position of the trees. The residual position uncertainty was then corrected by manually aligning the positions of the plot center and surveyed tree with the LiDAR point cloud of the corresponding circular plot. The data were coregistered using the Iterative Closest Point (ICP) algorithm shown in Chapter 3. Both the LiDAR acquisitions were

²The authors would like to thank the “Dipartimento Risorse Forestali e Montane” of the Autonomous Province of Trento for providing LiDAR data used in this paper in the framework of the FORLIDAR project.

rasterized at 0.5 m resolution. The threshold values T_β and T_γ were set equal to 0.75 and 0.3, respectively, while ϵ was set equal to 0.001. Cut of trees and forest regrowth phenomena were simulated to test the robustness of the proposed approach in detecting forest changes. To this end, trees were manually delineated and removed at time t_1 and at time t_2 . Note that few non-simulated changes were already present. The numerical results are presented in terms of Omission Errors (OE), Commission Errors (CE) and Overall Accuracy (OA) considering all the trees of the 16 plots.

Results

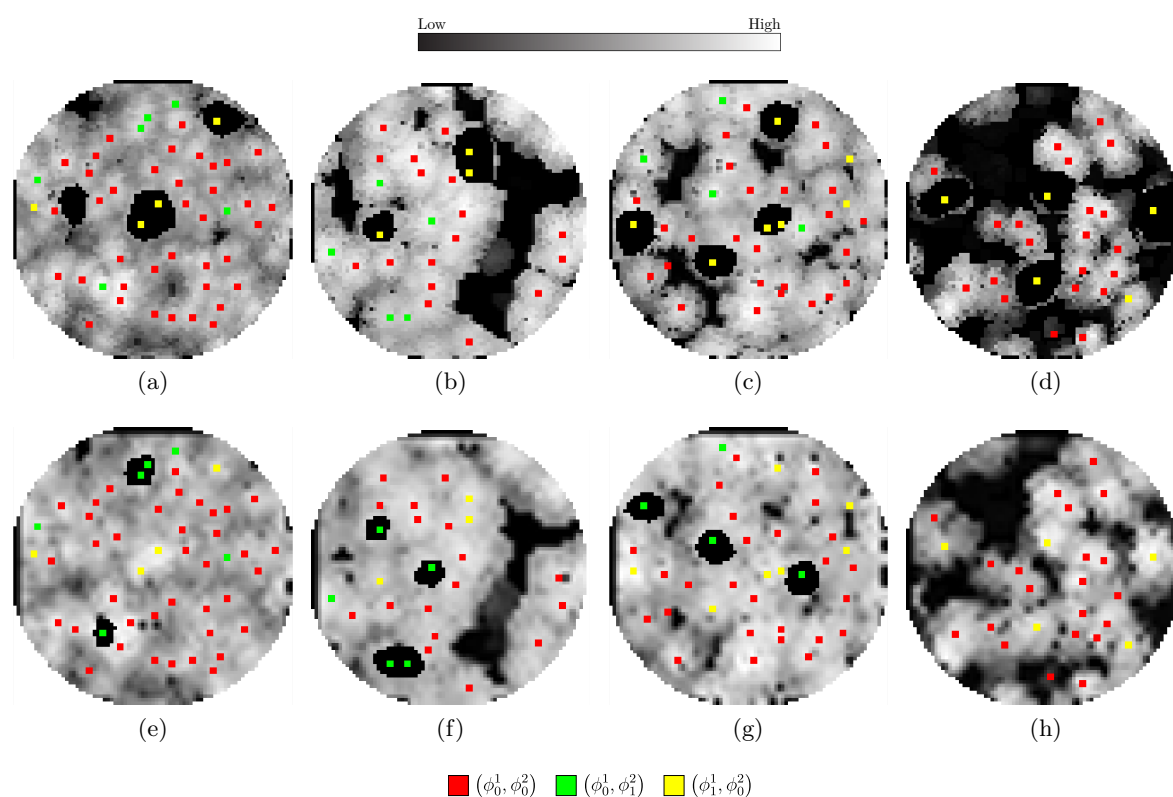


Figure 5.3: Example of compound tree detection maps in 4 plots: (a-d) t_1 CHMs; (e-h) t_2 CHMs. The colored dots represent the tree-top positions with the color representing the type of transition.

The results obtained with the proposed method were compared with: i) the tree-top detection performed independently at each single-date and ii) the merging of the tree-tops separately detected at both dates. Tables 5.1a and 5.1b show the numerical results in terms of CE, OE and OA obtained at times t_1 and t_2 , respectively. As expected, the OE value at time t_1 is quite similar for the single-date case and the proposed compound approach due to relatively high pulse density of the t_1 LiDAR acquisition. However, even though most of the omitted trees cannot be easily identified in the CHM (e.g., they are partially covered by other higher trees), the proposed method reduces the OE without increasing the CE. In contrast, the merging technique shows a significant increase of

Commission Errors due to the fact that the merging is not able to detect changes and thus all the trees not present at t_1 but present at t_2 are counted as tree-tops also at t_1 . The OA shows that the proposed method has better results compared both to the single-date and merge cases

Table 5.1: Omission Errors (OE), Commission Errors (CE) and Overall Accuracy (OA) obtained: (a) at time t_1 ; (b) at time t_2 . The proposed compound method (Compound) is compared with the tree-top detection obtained on the singular acquisitions (Single-date) and the simple integration of the tree-tops detected in both dates (Merge).

(a)							
Approach	Trees		OE		CE		OA
	#	#	%	#	%	%	
Single-date	487	79	16.2	5	1	82.9	
Merge	487	66	13.6	74	15.2	75	
Compound	487	68	14	5	1	85.2	

(b)							
Approach	Trees		OE		CE		OA
	#	#	%	#	%	%	
Single-date	484	111	22.9	30	6.2	72.6	
Merge	484	65	13.4	79	16.3	74.4	
Compound	484	79	16.3	15	3.1	81.2	

Table 5.2: Error matrix related to class transitions obtained by the proposed compound approach.

		Reference			
		(ϕ_0^1, ϕ_0^2)	(ϕ_0^1, ϕ_1^2)	(ϕ_1^1, ϕ_0^2)	(ϕ_1^1, ϕ_1^2)
Proposed	(ϕ_0^1, ϕ_0^2)	334	1	0	11
	(ϕ_0^1, ϕ_1^2)	22	55	0	2
	(ϕ_1^1, ϕ_0^2)	0	0	60	14
	(ϕ_1^1, ϕ_1^2)	0	0	0	0

Considering time t_2 (Table 5.1b), the OA produced by the proposed method is sharply higher than that of the single-date case, thus proving the importance of the bitemporal information. Indeed, due to the low density of the t_2 acquisition, there is a high number of missed tree-tops by the LiDAR sensor which leads to a high number of OE when only the information of the single-date is considered. By using the bitemporal information, the proposed approach exploits the information of the higher density data of date t_1 to reduce the OE but also the CE. The merging is capable of recovering more missed trees with respect to the proposed method. However, this comes at the cost of a strong increase

of the number of CE, which at the end leads to a decrease of the OA.

Figure 5.3 shows the maps of detected trees for 4 plots. The sets of fused tree-tops are overlapped on the CHMs of times t_1 and t_2 and represented with different colors, according to the type of bitemporal transition. The qualitative analysis confirms the results obtained from the quantitative view point. The method accurately identifies all the changes (i.e., tree cuts (ϕ_0^1, ϕ_1^2) and planting of trees (ϕ_1^1, ϕ_0^2)). Moreover, almost all the trees that are present at both dates are correctly identified as unchanged.

Table 5.2 shows the error matrix related to the transitions obtained by the proposed compound method. The proposed approach identifies almost all the changed trees. The tree-tops wrongly identified as changed (i.e., the 22 pixels identified as (ϕ_0^1, ϕ_1^2)) are trees clearly visible at one date but not well represented by the CHM at the other date. Therefore, the compound approach identifies this variation of the posterior probability as a change. Note that candidate tree-tops that are CE at both dates are identified as trees at both dates or as changed trees (i.e., 11 pixels identified as (ϕ_0^1, ϕ_0^2) , 2 pixels identified as (ϕ_0^1, ϕ_1^2) and 14 pixels identified as (ϕ_1^1, ϕ_0^2)). This is due to two main reasons: i) at least at one date they have a high $P(\phi_0^t | \mathbf{f}_k^t)$ (due to a local maximum present in the CHM caused typically by rasterization errors or isolated branches); ii) the LSM detects few CE and therefore $P(\phi_1^2 | \phi_1^1)$ has very low values (or is equal to 0).

5.3 Proposed Method for the Estimation of Crown Parameters on Low Density Data

In this second part we present a method for the fusion of the bitemporal information for tree-crown parameters estimation on low density data. Figure 5.4 shows the block scheme of the proposed method that takes as input a low and a medium/high density point clouds acquired at times t_1 and t_2 , respectively. From now on we will refer to the medium/high density data as high density. The method is based on three main steps: i) pre-processing, ii) crown parameters estimation on high density data, and iii) crown parameters estimation on low density data.

The point clouds are first coregistered using the ICP algorithm (Chapter 3) and then normalized by subtracting the DTM, thus generating the normalized point clouds \mathcal{P}^H (high density) and \mathcal{P}^L (low density). Then, \mathcal{P}^H is regularized and interpolated to obtain the Canopy Height Model. After the pre-processing, the method focuses on \mathcal{P}^H to char-

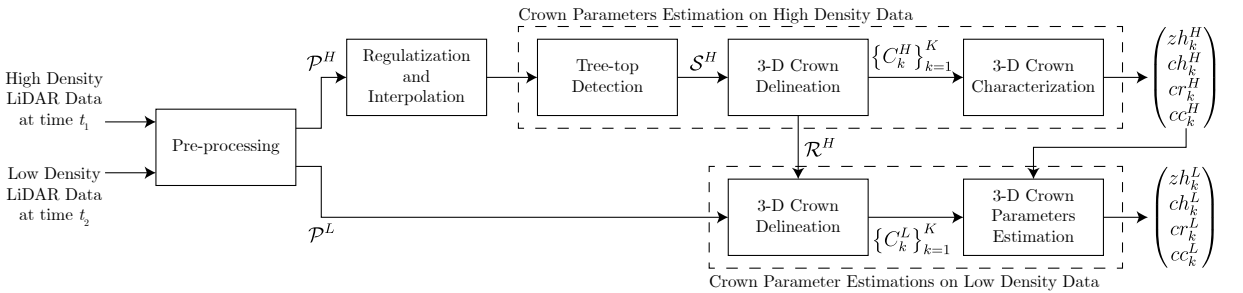


Figure 5.4: Block scheme of the proposed fusion method for crown parameters estimation.

acterize the individual tree-crown shapes. Then, the information derived from \mathcal{P}^H is used to drive the parameters estimation of \mathcal{P}^L by taking into account changes that may have occurred in the tree structure between the two acquisitions. The method assumes that large changes such as cut trees have been already identified (Chapter 3). Here we assume that \mathcal{P}^H was acquired at time t_2 and \mathcal{P}^L at time t_1 . The method can be easily adapted to work for the opposite case. It is worth noting that here we refer to the two point clouds as \mathcal{P}^L (acquired at time t_1) and \mathcal{P}^H (acquired at time t_2) whereas in 5.2 and Chapter 3 we use the notation \mathcal{P}^1 (time t_1) and \mathcal{P}^2 (time t_2). This is done to point the difference between high (\mathcal{P}^H) and low (\mathcal{P}^L) pulse density.

5.3.1 Crown Parameters Estimation on High Density Data

The first step of the proposed method aims to accurately characterize the shape of the individual tree-crowns present in the scene by using only the high density dataset \mathcal{P}^H . The tree-top locations are detected in the CHM^H using a LSM [178] that generates a set of tree-tops \mathcal{S}^H . Set \mathcal{S}^H is then exploited in the individual tree-crown segmentation (which is also carried out in the CHM^H). First, a rough segmentation aims at defining a bounding box to delineate the crown boundaries later refined by a directional analysis (Chapter 3). The obtained set $\mathcal{R}^H = \{R_k^H\}_{k=1}^K$ of 2-D regions (R_k^H is the segmentation region of the k th tree) are then transferred into the 3-D point cloud space of \mathcal{P}^H to obtain a segmented point cloud for each tree-crown. Let $\{C_k^H\}_{k=1}^K$ be the set of segmented high density point clouds where C_k^H is the k th identified tree.

To characterize the individual crowns, we reconstruct the shape of the trees using a parametric 3-D model. Since we assume to work only on conifers, we use a 3-D ellipsoid model which is the same used in Chapter 3. Here we recall the main characteristics of the 3-D model. The model is controlled by four parameters: i) tree top height zh located in (xh, yh) ; ii) canopy height ch ; iii) crown radius cr ; iv) crown curvature cc . It is defined as follows:

$$\frac{(z + ch - zh)^{cc}}{ch^{cc}} + \frac{[(x - xh)^2 + (y - yh)^2]^{cc/2}}{cr^{cc}} = 1, \quad zh - ch \leq z \leq zh. \quad (5.15)$$

Let us focus on the generic point clouds C_k^H of the k th tree. To model the shape of the tree, all the parameters of the 3-D model have to be estimated. The estimation of the parameters is carried out following two approaches. Since we are dealing with high density data, some of the parameters can be estimated by analyzing directly the point cloud. This is the case of the tree top height zh_k^H , base height bh_k^H and canopy height ch_k^H . The top height can be reliably approximated as the height of the highest point in C_k^H with the corresponding (xh_k, yh_k) . The base height is approximated as the lowest point C_k^H without considering ground points. It is worth noting that such approximation is reliable only with a high density point cloud and with a good penetration rate of the laser in order to have an accurate representation of the lower portion of the canopy. The canopy height is computed as $ch_k^H = zh_k^H - bh_k^H$. For the remaining parameters we use an optimization approach using a Differential Evolution (DE) algorithm that uses as cost function the sum of the residual distances between each point of the segmented LiDAR

data and the 3-D ellipsoid. Given zh_k^H and ch_k^H , the algorithm searches in the space of the solutions for the optimal set of parameters (cr_k^H, cc_k^H) . The residual distance between a generic point (x_i, y_i, z_i) and the surface of the 3-D model with parameters (cr_k^H, cc_k^H) is defined as:

$$r_i(cr_k^H, cc_k^H) = -1 + \frac{(z_i + ch_k^H - zh_k^H)^{cc_k^H}}{(ch_k^H)^{cc_k^H}} + \frac{\left[(x_i - xh_k^H)^2 + (y_i - yh_k^H)^2 \right]^{cc_k^H/2}}{(cr_k^H)^{cc_k^H}}. \quad (5.16)$$

The DE algorithm searches for the (cr_k^H, cc_k^H) such that:

$$(cr_k^H, cc_k^H) = \underset{(cr_k^H, cc_k^H)}{\operatorname{argmin}} r(cr_k^H, cc_k^H), \quad (5.17)$$

where the cost function r is:

$$r(cr_k^H, cc_k^H) = \sum_{i=1}^{\#C_k^H} r_i(cr_k^H, cc_k^H)^2, \quad (5.18)$$

where $\#C_k^H$ is the number of points in C_k^H . The search space (i.e., possible values of (cr_k^H, cc_k^H)) of the optimization algorithm is limited by setting these boundary conditions $cr_k^H \in [1, 10]$ and $cc_k^H \in [1.5, 1.9]$, considering the expected shape of a conifer. At the end of the process we obtain both accurate estimates of the parameters of each tree at the date associated with the high density LiDAR data and a model of its shape to be used for driving the estimates at the date where only low density data are available.

5.3.2 Crown Parameters Estimation on Low Density Data

Low density LiDAR data prevent the use of single-tree level approaches because the number of points is not sufficient to detect and delineate the individual trees. To address this issue, the proposed method aims to take advantage from the tree model derived from the high density dataset. Since we aim to study the multitemporal dynamics of the forest, the individual tree parameters cannot be directly inherited from the high density data. Indeed, while it is reasonable to assume that the location of the tree is not changed, the others parameters can be significantly different. For this reasons, when using the information of the high density point cloud, we have to take into account the temporal shift. This is done by using the information of the high density data to improve the crown parameters estimation on the low density while preserving the information content of the latter.

As for the high density case, first the trees have to be identified and delineated. Due to the low density of the data, applying the LSM used in 5.3.3 would lead to a high number of missed alarms caused by the tree-tops missed by the laser and also false alarms caused by the interpolation of the point cloud to generate the CHM. To avoid this, we use the assumption that large changes have been identified and removed to inherit the tree-top positions from the high density data (i.e., we use set \mathcal{S}^H). Similarly, the segmentation results of \mathcal{P}^H are used in \mathcal{P}^L (i.e., we use set \mathcal{R}^H). To take into account the temporal

shift, the segmentation regions are reduced in size (80% of the original size) to generate a set of conservative segmented point clouds for the low density dataset. This it to take into account the horizontal expansion of the crown which may lead to select points (in the low density data) outside the true crown boundary. Therefore, the reduction in size is used to select only the portion of the crown close to the tree-top reducing segmentation errors.

Let $\{C_k^L\}_{k=1}^K$ be the set of segmented low density point clouds, where C_k^L is the k th tree. Similarly to the high density case, the shape of each tree C_k^L is reconstructed using the 3-D parametric model. However, note that this step aims at using the 3-D model and the information of \mathcal{P}^H to improve the crown parameters estimation. To drive the model fitting on a generic point cloud C_k^L , we use the crown characterization learned from C_k^H (i.e., crown parameters $(zh_k^H, ch_k^H, cr_k^H, cc_k^H)$). In order to preserve the information of C_k^L and thus the possibility of analyzing the tree dynamics over time, the possible changes of the tree structure have to be taken into account. To this end, we we make the following assumptions based on the natural dynamics of trees:

1. The tree-top height and crown radius increase with time or remain constant.
2. The crown curvature and base height does not change significantly in time.

The first assumption is based on the natural dynamics of trees. While it might not hold for all the trees in analysis due to multiple factors such as crown damage, it is a reasonable assumption for most of the cases. Regarding the crown curvature, this is a species-dependent parameter which does not show any significant variation in time. The base height changes slowly in time since it is due to the death of the lowest branches of the crown (see Chapter 3). Considering these two assumptions, we set the following boundary conditions:

- $zh_k^L \in [\max_z(C_k^L), zh_k^H];$
- $cr_k^L \in [\sqrt{\Xi_k^L/\pi}, cr_k^H];$
- $bh_k^L = bh_k^H;$
- $ch_k^L = zh_k^L - bh_k^L;$
- $cc_k^L = cc_k^H;$

where Ξ_k^L is the area of the 2-D convhull of the (x, y) points in C_k^L without considering ground points. Thanks to these boundary conditions defined considering the information extracted from C_k^H , the DE algorithm has to explore only the solution space of zh_k^L and cr_k^L since the cc_k^L is fixed and ch_k^L depend on zh_k^L . The DE is used considering a different cost function with respect to the one showed in Equation (5.18). In particular, in order to better drive the parameters estimation, a regularization term κ that model the similarity between zh_k^L and zh_k^H , cr_k^L and cr_k^H is used. This regularization term is based on the assumption that even though the top height and crown radius change over time, the

change is typically small due to the natural properties of tree. The new cost function is defined as:

$$r\kappa(zh_k^L, cr_k^L, zh_k^H, cr_k^H) = r(zh_k^L, cr_k^L) + \zeta\kappa(zh_k^L, cr_k^L, zh_k^H, cr_k^H), \quad (5.19)$$

where κ :

$$\kappa(zh_k^L, cr_k^L, zh_k^H, cr_k^H) = \frac{|zh_k^L - zh_k^H|}{zh_k^L + zh_k^H} + \frac{|cr_k^L - cr_k^H|}{cr_k^L + cr_k^H}, \quad (5.20)$$

and ζ is a weight that defines how much the regularization term influences the cost function. The two parameters are estimated according to:

$$(zh_k^L, cr_k^L) = \underset{(zh_k^L, cr_k^L)}{\operatorname{argmin}} r\kappa(zh_k^L, cr_k^L, zh_k^H, cr_k^H), \quad (5.21)$$

By using the boundary conditions and the regularization term we perform the estimation of the parameters of the tree preserving the information of the low density point cloud. Note that, as pointed out previously, the two assumptions may not hold for all the analyzed trees. This may cause errors in the parameters estimation for these crowns. However, since the two assumptions are based on the properties of the crowns, the number of trees that do not satisfy them is likely small. Accordingly, these assumptions can be used to obtain a gain in parameters estimation accuracy for most of the trees whereas for the crowns that do not satisfy the two conditions, errors may be introduced. However, since the number of these trees is small, the impact on the overall accuracy is also likely to be small.

5.3.3 Experimental Results

Experimental Setup

The method has been tested on a bitemporal airborne LiDAR dataset acquired in the southern Italian Alps in the Trento province. The study area is characterized by a complex morphology with an altitude ranging from 900 m to 2800m. The trees in the study area mainly belong to the species *Larix decidua* (European Larch) and *Picea abies* (Norway Spruce). The data were acquired in 2012 and 2015 with a maximum pulse density of 50 and 15 pulses/m², respectively. A 80 m×80 m and a 70 m×70 plots were selected. Note that in this case the high density data were acquired at time t_1 . Since no ground truth is available we exploited the very high density data of time t_1 to validate the method. Figure 5.5 shows the experimental setup. We used the data of time t_1 to extract the crown parameters to be used as validation (i.e, $(zh_k^V, ch_k^V, cr_k^V, cc_k^V)$). In particular 82 individual tree-crowns were manually identified and delineated (as in Chapter 3) and the crown parameters were estimated for each tree using the approach described in 5.3.1. The extracted crown parameters were validated manually for each tree. To simulate the case where the t_1 acquisition is the low density one \mathcal{P}^L , a random thinning was applied to the 2012 data simulating 4 different low densities: 5, 2, 0.5 and 0.25 pulses/m². To take into account the random nature of the thinning process, 10 thinning simulations were performed and the results were computed as average of the 10 simulations. To prove the effectiveness of the

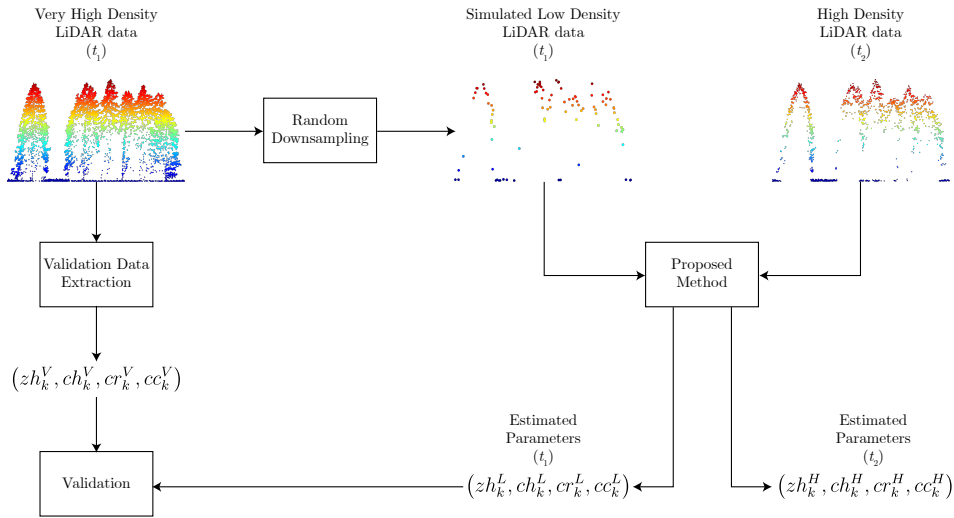


Figure 5.5: Block scheme of the experimental setup showing how the very high density data are used to validate the method.

method, we compared the Root Mean Square Error (RMSE) of the parameters estimation obtained when using only the low density point cloud (i.e., single-date estimation) and when the information of the higher density data is used. As pointed out in 5.3.2, tree detection and delineation applied to low density data leads to poor results. Therefore, to have a fair comparison, we used the segmentation regions computed on \mathcal{P}^H also in the tests in which we used only the information of \mathcal{P}^L (i.e., single-date estimation). Moreover, in the single-date crown parameters estimation, boundary conditions were used to limit the search space only to reasonable values. The only parameter ζ of the method was set as $\zeta = 0.4$.

Results

Table 5.3 shows the numerical results of the proposed method compared to the single-date estimation. As expected, the proposed method achieved better results in almost all the cases with respect to the single-date estimation. In particular, the zh estimation shows an improvement ranging from 0.05 m for the 5 pulses/m² case to 0.7 m for the 5 pulses/m². There is only one case in which the single-date estimation achieved a slightly better results (-0.02 m). The canopy height ch estimation is strongly influenced by the penetration capability of the laser in the lower portion of the canopy. This is clearly visible in Table 5.3 since the RMSE of the single-date estimation increases significantly as the pulse density decreases. In contrast, the proposed method uses the assumption that the base height does not change to mitigate effects of the low density showing a decrease of RMSE up to more than 3 m. The results regarding crown radius cr show that the method improves the estimation accuracy for all the simulated densities in both stands. Moreover, the results show that the accuracy of the proposed method in estimating the cr is not significantly dependent on the pulse density. One of the factors that allows this is the use of the segmentation regions of \mathcal{P}^H in \mathcal{P}^L . This allows us to have a reliable delineation

Table 5.3: RMSE results on the 10 trials obtained by the single-date estimation (SD) and the proposed the method (PM) for (a) stand 1 and (b) stand 2.

(a)

Density [pulses/m ²]	Estimation Approach	Top Height zh [m]	Canopy Height ch [m]	Crown Radius cr [m]
5	SD	1.07	6.08	1.60
	PM	1.02	2.63	1.13
2	SD	1.32	6.24	1.54
	PM	1.22	2.81	1.08
0.5	SD	2.19	6.81	1.46
	PM	1.88	3.30	1.01
0.25	SD	3.22	7.43	1.42
	PM	2.54	3.84	0.98

(b)

Density [pulses/m ²]	Estimation Approach	Top Height zh [m]	Canopy Height ch [m]	Crown Radius cr [m]
5	SD	0.84	5.71	1.22
	PM	0.86	3.23	0.73
2	SD	1.20	5.96	1.22
	PM	1.10	3.42	0.71
0.5	SD	2.33	6.62	1.24
	PM	1.66	3.87	0.74
0.25	SD	3.41	7.39	1.37
	PM	2.71	4.59	0.78

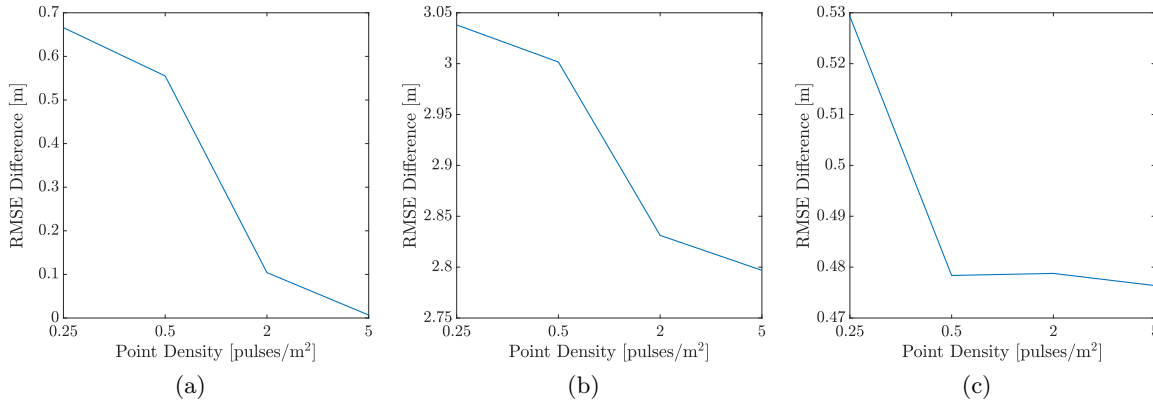


Figure 5.6: Difference between the average RMSE (considering all the 82 tree) obtained by the single-date approach and by the proposed method for: (a) top height zh , (b) canopy height ch and (c) crown radius cr .

of the crown boundary independently from the pulse density and as a consequence an accurate estimation of the crown radius.

The numerical results are summarized by Figure 5.6 that shows the average difference between the RMSE of the single-date and proposed method for all the 82 trees for the zh , ch and cr . Note how the difference increases as the density decreases thus showing that the proposed method effectively mitigates the effect of the low density on the crown parameters estimation.

5.4 Conclusion

In this Chapter two methods for the fusion of bitemporal LiDAR data were presented. The methods confirmed the importance of exploiting the increasing availability of multi-temporal LiDAR acquisitions over the same area to improve individual tree analysis both at each single-date and in the multitemporal domain. Indeed, to take full advantage of bitemporal LiDAR data the information of the two point clouds have to be fused. However, this has to be done taking into account the temporal shift to preserve the bitemporal information.

The two proposed contributions exploit the temporal correlation between the two dates to improve the analysis of the individual trees. In particular, the first method focuses on the detection of the trees while the second one addresses the estimation of crown parameters. The first presented contribution is a novel automatic method that model the temporal dependence of the trees at the two dates by means of a compound approach to improve the tree-top detection. This modeling can be used not only to improve the tree-top detection but also to detect changes at the individual tree level (tree cuts and forest regrowth). The experimental results showed that the use of the proposed compound approach improves the tree-top detection compared to what we obtain using only the single-date information. This is clearly visible on the lower density data since in that case the exploitation of the richer information content of the higher density data through the

compound model is effectively used to recover a significant number of trees. The results showed that the gain in terms of OA achieved on the low density data compared to the single-date detection is of 8.6%. The analysis also pointed out that the simple merging of the two sets of tree-tops is not sufficient to achieve satisfactory results since the merging is not able to detect the changes. This leads to a significant increase of the commission errors. In contrast, the proposed method solves this problem by automatically handling the detection of forest changes at single-tree level.

The second method fuses the bitemporal LiDAR data to use the rich information content of high density point clouds to improve the crown parameters estimation on low density data. This is done using a parametric 3-D model which allows us to drive the parameters estimation on the low density data using the model defined for the high density one. The numerical results show a significant decrease of the RMSE on all the considered parameters with respect to the estimates computed without considering the bitemporal information. The average RMSE improvement for the lowest simulated density is of 0.65 m for the top height, 3.04 m for the canopy height and 0.5 m for the crown radius. This numerical results point out that it is possible to improve the parameters estimation on a low density data using information derived from an high density point cloud by considering the dynamics of the tree-crown.

As future developments, in the first contribution we plan to investigate new geometric features for characterizing the individual tree-tops. Moreover, in both contributions we plan to consider also the time passed between the two acquisitions to model accordingly the temporal dependence between the two data. In particular, regarding the second contribution we aim to define ζ as a function of the time passed between the two acquisitions. Finally, both methods should be tested on multiple bitemporal LiDAR datasets acquired with at different time intervals.

Conclusion

This Chapter draws the conclusions of the thesis with a general discussion about the fulfillment of the objectives of the proposed research. A summary of the main contributions is then provided along with a critical analysis of their strengths and weaknesses. In the second part possible future developments are illustrated.

Discussion

In this thesis we addressed the multitemporal analysis of RS data. We focused on the analysis of bitemporal LiDAR point clouds and HS images, which are data that allow for an accurate characterization of the 3-D structure and spectral properties of the analyzed scene, respectively. The part of the thesis dedicated to LiDAR addressed the challenges related to the detection, delineation and characterization of individual tree crowns in bitemporal point clouds to improve the crown parameters estimation and detect 3-D changes at the individual tree level. This was done to address the literature gaps regarding CD for forestry applications in LiDAR data at the individual tree level. The part of the thesis focused on HSCD analyzed the concept of change in bitemporal HS data and studied how change information can be represented to perform multiple CD. It is important to underline that the work in this thesis has been carried out taking into account the limited availability of reference data and the wide extension of the areas that have to be analyzed in operational scenarios. Therefore, all the developed methods are automatic and unsupervised.

According to the objectives identified in the Introduction, three main contributions have been provided:

- The design of a method for CD at the individual tree level in LiDAR point clouds to detect both large changes (e.g., tree cut) and small changes (e.g., tree growth). In this context, we proposed a method for 3-D change detection in the forest canopy. The extracted change information can be effectively employed in precision forestry applications to provide an added value in the management of forest stands in terms of both identification of harvested or planted trees and, most importantly, of vertical and horizontal growth rate across the forest area of interest.
- The definition of an efficient representation of the change information in each spectral channel of HS images and a technique using this novel representation to perform multiple CD. We analyzed the change information contained in each band of the HS change vectors defining a representation that aims at preserving only the informative

content relevant to the CD problem. Therefore, the resulting binary HCVs can be used to perform multiple CD focusing only on the change information. The hierarchical clustering allows for the definition of a tree structure that can be used to produce different multiple CD maps depending on the level of detail required. The multiple CD maps obtained on agricultural areas confirmed how HS data allow for the detection of spectrally small changes. In particular, multiple changes have been detected inside single fields showing that the proposed binary change vectors preserve and highlight the information related not only to abrupt land-cover transitions but also spectrally subtle changes.

- The design of methods that fuse the information of bitemporal point clouds to improve tree-crown characterization at the single-date. The two proposed solutions exploit multitemporal data to improve the detection of trees and the estimation of forest crown parameters. Note that such fusion can be used not only at single-date level but also for the detection of changes. Most importantly, the proposed solutions aim at fusing data with different densities. This aspect can be exploited in operational scenarios since it allows for the use of low density data, acquired in the past, with the more recent high density point clouds. Indeed, if only data with similar densities are considered, the number of areas where multitemporal point clouds are available is still quite limited. In contrast, by using data with different densities the area coverage of multitemporal LiDAR data is significantly increased.

According to these considerations, it is possible to conclude that the proposed methods provide a valuable contribution to the multitemporal analysis of LiDAR point clouds and HS images and address open challenges and gaps in the literature.

In the following, the novel contribution of the thesis are reviewed considering the addressed challenges and the strengths and weaknesses of the methods pointing out the open issues that have still to be addressed. The first contribution (Chapter 3) addresses the first objective which is the problem of the detection of 3-D changes in individual tree crowns. The main steps include the proposed ICP procedure that exploits not only the canopy structure but also the shape of the terrain to co-register the two LiDAR point clouds with an accuracy high enough to guarantee that the CD results are not influenced by the registration errors. Moreover, in the individual tree analysis, the developed object-based CD is designed to be robust to the residual registration errors as each tree is matched with the corresponding tree at the other date. One of the most relevant problem is the comparison of the two point clouds that is strongly affected by the highly irregular nature of LiDAR data and tree-crowns. To this end, the shape of each tree crown is reconstructed using a 3-D parametric model to reduce the effects related to the irregular sampling of the laser. This model is used to compare different parameters among which the most relevant ones are the top height and crown volume. The proposed solution showed good performances with a good fitting of the 3-D model on most of the analyzed tree. However, note that both the proposed crown segmentation and this specific parametric model are suitable only for conifers. Therefore, in the case of a mixed forest where also broad-leaved trees are present, segmentation errors are likely to increase and the 3-D ellipsoid will not provide an accurate modeling of broad-leaved crowns. Moreover, fitting of the 3-D model is sensitive to strong asymmetries in the canopy structure, which negatively affect the

accuracy of the crown parameters estimation. However, this problem occurred only for a limited number of trees which in most of the cases were covered by dominant trees. The experimental results confirm that the CHMs difference can be used to detect large changes. The individual tree analysis shows estimates of growth that are consistent with the age and characteristics of the analyzed forest areas (i.e., 1 m of vertical growth for young trees and 0.4 m for older trees).

The second contribution, presented in Chapter 4, is a method for unsupervised multiple CD in HS images based on a novel efficient representation of the change information. The novel representation takes advantage of the fact that different bands contain significantly different change information. Indeed, given two or more changes, they can be separable in one spectral channel and indistinguishable in another one. This factor is taken into account by adaptively quantizing the radiometric values of each band to extract only the relevant change information. Indeed, the quantization highlights only the changes or groups of changes that are distinguishable at the considered band. In such a way, the resulting representation is significantly simpler with respect to the original one. Moreover, the binary codewords obtained by a coding process can be compressed to reduce redundant information. The quantization is carried out by analyzing the PDF of the radiometric values which is estimated using a KDE approach. Even though this method provided accurate quantization levels, an ad-hoc parametric model should also be considered. We generate a dendrogram via an hierarchical binary clustering modeling the CD problem. This dendrogram allows for the tuning of the sensitivity of the CD method to different levels of change thus giving the possibility of generating different CD maps depending on the application and user requirements. Both qualitative and quantitative results show that the novel binary representation is effectively used in the multiple CD obtaining a \mathcal{K}_c coefficient of 0.91 on a real dataset where a supervised method achieved a \mathcal{K}_c of 0.95. Moreover, the different CD maps prove that different level of detail can be obtained by tuning the sensitivity of the method. The selection of the level of sensitivity is the only input required by the method. Even though this is a limited interaction, this required user input may limit the application of the proposed method at a large scale.

The two methods for the fusions of bitemporal LiDAR are presented in Chapter 5. Their aim is to exploit the information content of the two point clouds to improve the characterization of the individual tree crown at the single-date. In the first method a compound approach is used to improve the tree-top detection at both dates and to detect large changes in coniferous forests. While the geometrical features used separately at the two dates describe the shape of the candidate tree-top to model its probability of being an actual tree-top, the matrix of probabilities of transition models the temporal correlation between the two dates. The features have been defined taking into account the shape of conifers which are characterized by one maximum. Therefore, the method can not be applied on other types of trees. All the statistical terms used in this method are estimated without the need of any reference data. In particular, the transition matrix is effectively estimated in an iterative approach using as initialization only the prior probabilities of the two classes. It is worth noting that the transition matrix depends on the characteristics of the analyzed forest and the changes occurred between the two dates. As a consequence, a transition matrix estimated for a given area can not be reliably

applied to other forests. However, since the estimation of the matrix elements does not require training data, the matrix can be easily re-estimated with the only drawback being the additional computation load. The combined use of the single-date probabilities and the transition matrix in a Bayes framework allows us not only to detect large changes but most importantly to identify false alarms and recover missed alarms. The improvement of the detection is more visible on the data with lower density since the method recovers missed trees without increasing significantly the number of false alarms. The OA obtained by the proposed method on the lower density shows an increase of 8.6% and 6.8% with respect to the single-date approach and the merge approach, respectively.

The second method of the last contribution exploits the fusion of high and low density data to improve the estimation of crown parameters on the latter. The use of the crown position and boundaries estimated in the high density data to delineate the crown in the low density avoids the use of an automatic segmentation on a low density point cloud which would perform poorly. The 3-D parametric model simplifies the inferring of the information of the high density data into the low density one since only the parameters of the model have to be used. The method takes advantage of the two assumptions made considering the dynamics of the trees not only to limit the possible range of values of the estimated parameters, but also to model the slow growth of the tree canopy by means of regularization term. Note that the estimation of the parameters of the low density point cloud is done not only considering the two multitemporal assumptions but also by fitting the 3-D model on the segmented low density data. This is very important since it allows us to preserve the unique information of the low density data. The average RMSE improvement on the data with the lowest density is of 0.65 m for the top height, 3.04 m for the canopy height and 0.5 m for the crown radius. Due to the limited availability of multitemporal data, the method has been tested only on a pair of acquisitions thus considering a single temporal interval. Therefore, it was not possible to study the effects on the correlation between different acquisitions varying the length of the time interval.

Future Developments

In this thesis new methods for the CD in LiDAR and HS data and for the fusion of LiDAR point clouds have been proposed giving an important contribution to the capability of detecting changes in forest areas, detecting and discriminating changes using HS data and modeling the individual tree crown. However, there are still multiple directions of research that should be properly analyzed to further exploit the rich information content of multitemporal LiDAR, HS and other RS data. Accordingly, in the following we describe some future developments that aim not only at extending the presented work but also at addressing other RS problems using the novel approaches defined in this thesis.

First of all, we aim to extend the experiments of all the methods in order to evaluate them in different settings. In particular, we plan to use:

- LiDAR data acquired on forests with different structure and age to study how different forests change over time.
- Multiple HS datasets with ground reference acquired over different type of areas.

- Different bitemporal LiDAR datasets with different time intervals between the two acquisitions to better study how the bitemporal information is preserved by the proposed fusion methods when the time interval increases.

The methods presented in this thesis for LiDAR data analysis have been developed for coniferous forest. Conifers are characterized by a well defined shape with generally only one maximum. This is not the case of broadleaved trees that are characterized by an umbrella shaped crown with multiple local maxima. Therefore, efforts should be devoted to the adaptation of the proposed methods to the case of deciduous forest. First of all, ad-hoc methods for the detection and delineation of the broadleaved tree crowns should be developed taking into account the specific properties of these trees. Moreover, other approaches to reconstruct the shape of the tree crown should be investigated. Such approaches should be robust to irregularities in the crown shape allowing for asymmetries.

In this dissertation, bitemporal LiDAR and HS data have been used separately for CD applications. However, their combined use would allow us to relate 3-D changes in forests with spectral changes such as variations in health status of the vegetations (e.g., vegetation stress). As an example, this information could be used to study the effects of the variation of chlorophyll content (or others biophysical variables) or of insect attacks on the estimates of growth of the trees. Moreover, the spectral information of HS data could be used to automatically identify the species of each tree in order to perform an ad-hoc CD depending on the species. Indeed, one may use a specific 3-D model for each tree species to reconstruct the shape of the crown.

The novel representation of the change information has been developed for the spectral domain to obtain a simplified binary version of the HCVs. However, future analysis should be devoted to its application to other domains such as the temporal domain. Indeed, with the new Sentinel constellation, long and very long image time series are becoming more and more available. Focusing on the spectral multitemporal profile of each pixel, the binary representation could be used to represent the temporal evolution of the considered area and thus the changes occurred in a given pixel in the time interval of the series.

The UAVs and small HS sensors will increase the number of HS images in the future. The main difference with respect to aircraft and satellites is the capability of UAVs of flying at a very low altitude with respect to the ground. Such low altitude allows for acquisitions at Extremely High spatial Resolution (EHR). Considering this aspect, we plan to work on HS multitemporal datasets acquired by UAVs to better understand the CD problem in such data. This requires to address the issue of the registration of EHR images that is challenging since the definition of ground control points, both in supervised and unsupervised ways, could be difficult. The EHR permits to detect very subtle changes such as variation of the foliage characteristics at the level of individual branches or even leaves. Therefore, a redefinition of the concept of change depending on the considered application is required to avoid the detection of a large number of false alarms.

List of Publications

INTERNATIONAL JOURNALS

- [J1] **D. Marinelli**, C. Paris, L. Bruzzone, "A Novel Approach to 3-D Change Detection in Multitemporal LiDAR Data Acquired in Forest Areas," in *IEEE Transactions on Geoscience and Remote Sensing*, vol. 56, no. 6, pp. 3030-3046, June 2018.
- [J2] **D. Marinelli**, F. Bovolo, L. Bruzzone, "A Novel Change Detection Method for Multitemporal Hyperspectral Images Based on Binary Hyperspectral Change Vectors," in *IEEE Transactions on Geoscience and Remote Sensing*, vol. 57, no. 7, pp. 4913-4928, July 2019.
- [J3] S. Liu, **D. Marinelli**, F. Bovolo, L. Bruzzone, "A Review on Change Detection in Multitemporal Hyperspectral Images," in *IEEE Geoscience and Remote Sensing Magazine*, vol. 7, no. 2, pp. 140-158, June 2019.
- [J4] **D. Marinelli**, C. Paris, L. Bruzzone, "A Novel Data Fusion Approach to Compound Tree Detection in Multitemporal LiDAR Data," in *IEEE Geoscience and Remote Sensing Letters*, in press.

INTERNATIONAL CONFERENCES

- [C1] **D. Marinelli**, C. Paris, L. Bruzzone, "Fusion of High and Very High Density LiDAR Data for 3D Forest Change Detection," *2016 IEEE International Geoscience and Remote Sensing Symposium (IGARSS)*, Beijing, China, 2016, pp. 3595-3598.
- [C2] **D. Marinelli**, F. Bovolo and L. Bruzzone, "A Novel Method for Unsupervised Multiple Change Detection in Hyperspectral Images based on Binary Spectral Change Vectors," *2017 9th International Workshop on the Analysis of Multitemporal Remote Sensing Images (MultiTemp)*, Brugge, Belgium, 2017, pp. 1-4.
- [C3] **D. Marinelli**, F. Bovolo, L. Bruzzone, "A Novel Change Detection Method for Multitemporal Hyperspectral Images based on a Discrete Representation of the Change Information," *2017 IEEE International Geoscience and Remote Sensing Symposium (IGARSS)*, Fort Worth, USA, 2017, pp. 161-164.
- [C4] **D. Marinelli**, N. C. Coops, D. K. Bolton, L. Bruzzone, "An Unsupervised Change Detection Method for Lidar Data in Forest Areas Based on Change Vector Analysis in the Polar Domain," *2018 IEEE International Geoscience and Remote Sensing Symposium (IGARSS)*, Valencia, Spain, 2018, pp. 1922-1925.

- [C5] **D. Marinelli**, C. Paris and L. Bruzzone, "Fusion of Multitemporal LiDAR Data for Individual Tree Crown Parameter Estimation on Low Density Point Clouds," *2018 IEEE International Geoscience and Remote Sensing Symposium (IGARSS)*, Valencia, Spain, 2018, pp. 3999-4002. **Second Place in the IGARSS 2018 Student Paper Competition.**
- [C6] **D. Marinelli**, C. Paris and L. Bruzzone, "An Automatic Technique for Deciduous Trees Detection in High Density LiDAR Data based on Delaunay Triangulation," *2019 IEEE International Geoscience and Remote Sensing Symposium (IGARSS)*, Yokohama, Japan, 2019, in press.
- [C7] M. Zanetti, **D. Marinelli**, M. Bertoluzza, S. Saha, F. Bovolo, L. Bruzzone, M. L. Magliozzi, M. Zavagli, M. Costantini, "A high resolution burned area detector for Sentinel-2 and Landsat-8," *2019 10th International Workshop on the Analysis of Multitemporal Remote Sensing Images (MultiTemp)*, Shangai, China, 2019, in press.

Bibliography

- [1] UNFCCC, “Kyoto protocol reference manual on accounting of emissions and assigned amount,” 2009.
- [2] L. Bruzzone and F. Bovolo, “A novel framework for the design of change-detection systems for very-high-resolution remote sensing images,” *Proceedings of the IEEE*, vol. 101, no. 3, pp. 609–630, March 2013.
- [3] J. Holmgren, “Prediction of tree height, basal area and stem volume in forest stands using airborne laser scanning,” *Scandinavian Journal of Forest Research*, vol. 19, no. 6, pp. 543–553, 2004.
- [4] T. Gobakken and E. Næsset, “Assessing effects of laser point density, ground sampling intensity, and field sample plot size on biophysical stand properties derived from airborne laser scanner data,” *Canadian Journal of Forest Research*, vol. 38, no. 5, pp. 1095–1109, 2008.
- [5] E. Næsset, “Accuracy of forest inventory using airborne laser scanning: evaluating the first nordic full-scale operational project,” *Scandinavian Journal of Forest Research*, vol. 19, no. 6, pp. 554–557, 2004.
- [6] E. Næsset, T. Gobakken, J. Holmgren, H. Hyypä, J. Hyypä, M. Maltamo, M. Nilsson, H. Olsson, Åsa Persson, and U. Söderman, “Laser scanning of forest resources: the nordic experience,” *Scandinavian Journal of Forest Research*, vol. 19, no. 6, pp. 482–499, 2004.
- [7] M. Maltamo, E. Næsset, and J. Vauhkonen, *Forestry applications of airborne laser scanning*. Springer, 2014.
- [8] T. G. Gregoire, E. Næsset, R. E. McRoberts, G. Ståhl, H.-E. Andersen, T. Gobakken, L. Ene, and R. Nelson, “Statistical rigor in lidar-assisted estimation of aboveground forest biomass,” *Remote Sensing of Environment*, vol. 173, pp. 98 – 108, 2016.
- [9] J. Hyypä, H. Hyypä, D. Leckie, F. Gougeon, X. Yu, and M. Maltamo, “Review of methods of small-footprint airborne laser scanning for extracting forest inventory data in boreal forests,” *International Journal of Remote Sensing*, vol. 29, no. 5, pp. 1339–1366, 2008.
- [10] B. Koch, U. Heyder, and H. Weinacker, “Detection of individual tree crowns in airborne lidar data,” *Photogrammetric Engineering & Remote Sensing*, vol. 72, no. 4, pp. 357–363, 2006.
- [11] C. Paris and L. Bruzzone, “A growth-model-driven technique for tree stem diameter estimation by using airborne lidar data,” *IEEE Transactions on Geoscience and Remote Sensing*, vol. 57, no. 1, pp. 76–92, Jan 2019.
- [12] L. Eysn, M. Hollaus, E. Lindberg, F. Berger, J.-M. Monnet, M. Dalponte, M. Kobal, M. Pellegrini, E. Lingua, D. Mongus, and N. Pfeifer, “A benchmark of lidar-based single tree detection methods using heterogeneous forest data from the alpine space,” *Forests*, vol. 6, no. 5, pp. 1721–1747, 2015.
- [13] X. Yu, J. Hyypä, M. Holopainen, and M. Vastaranta, “Comparison of area-based and individual tree-based methods for predicting plot-level forest attributes,” *Remote Sensing*, vol. 2, no. 6, pp. 1481–1495, 2010.
- [14] M. Holopainen, M. Vastaranta, and J. Hyypä, “Outlook for the next generation’s precision forestry in finland,” *Forests*, vol. 5, no. 7, pp. 1682–1694, 2014.
- [15] V. Lafond, G. Lagarrigues, T. Cordonnier, and B. Courbaud, “Uneven-aged management options to promote forest resilience for climate change adaptation: effects of group selection and harvesting intensity,” *Annals of forest science*, vol. 71, no. 2, pp. 173–186, 2014.
- [16] E. Lindberg, J. Holmgren, K. Olofsson, J. Wallerman, and H. Olsson, “Estimation of tree lists from airborne laser scanning by combining single-tree and area-based methods,” *International Journal of Remote Sensing*, vol. 31, no. 5, pp. 1175–1192, 2010.

- [17] M. Vastaranta, V. Kankare, M. Holopainen, X. Yu, J. Hyypä, and H. Hyypä, "Combination of individual tree detection and area-based approach in imputation of forest variables using airborne laser data," *ISPRS Journal of Photogrammetry and Remote Sensing*, vol. 67, pp. 73 – 79, 2012.
- [18] Norwegian mapping and cadastre authority. (Date last accessed May 2019). [Online]. Available: <https://hoydedata.no/>
- [19] National land survey of Finland. (Date last accessed May 2019). [Online]. Available: <https://www.maanmittauslaitos.fi/en/maps-and-spatial-data/expert-users/product-descriptions/laser-scanning-data>
- [20] T. Nord-Larsen, T. Riis-Nielsen, and M. B. Ottosen, "Forest resource map of Denmark: Mapping of danish forest resource using als from 2014-2015," 2017.
- [21] F. Bovolo and L. Bruzzone, "The time variable in data fusion: A change detection perspective," *IEEE Geoscience and Remote Sensing Magazine*, vol. 3, no. 3, pp. 8–26, Sept 2015.
- [22] Earth science data archives of U.S. Geological Survey (USGS). (Date last accessed February 2018). [Online]. Available: <https://earthexplorer.usgs.gov>
- [23] Copernicus open access hub. (Date last accessed May 2019). [Online]. Available: <https://scihub.copernicus.eu/>
- [24] S. Liu, L. Bruzzone, F. Bovolo, and P. Du, "Hierarchical unsupervised change detection in multitemporal hyperspectral images," *IEEE Transactions on Geoscience and Remote Sensing*, vol. 53, no. 1, pp. 244–260, 2015.
- [25] W. G. Rees, "Principles of remote sensing, third edition," *Remote Sensing of Glaciers. London*, 2013.
- [26] J. C. Fernandez-Diaz, W. E. Carter, C. Glennie, R. L. Shrestha, Z. Pan, N. Ekhtari, A. Singhanian, D. Hauser, and M. Sartori, "Capability assessment and performance metrics for the titan multispectral mapping lidar," *Remote Sensing*, vol. 8, no. 11, 2016.
- [27] E. Baltsavias, "Airborne laser scanning: basic relations and formulas," *ISPRS Journal of Photogrammetry and Remote Sensing*, vol. 54, no. 2, pp. 199 – 214, 1999.
- [28] J. Reitberger, P. Krzystek, and U. Stilla, "Analysis of full waveform lidar data for the classification of deciduous and coniferous trees," *International Journal of Remote Sensing*, vol. 29, no. 5, pp. 1407–1431, 2008.
- [29] J. Reitberger, C. Schnörr, P. Krzystek, and U. Stilla, "3d segmentation of single trees exploiting full waveform lidar data," *ISPRS Journal of Photogrammetry and Remote Sensing*, vol. 64, no. 6, pp. 561 – 574, 2009.
- [30] D. Gatzliolis and H.-E. Andersen, "A guide to lidar data acquisition and processing for the forests of the pacific northwest." *Gen. Tech. Rep. PNW-GTR-768. Portland, OR: US Department of Agriculture, Forest Service, Pacific Northwest Research Station. 32 p*, vol. 768, 2008.
- [31] F. Rohrbach. (2015) Lidar footprint diameter. (Date last accessed January 2019). [Online]. Available: <http://felix.rohrba.ch/en/2015/lidar-footprint-diameter/>
- [32] J. Holmgren, M. Nilsson, and H. Olsson, "Simulating the effects of lidar scanning angle for estimation of mean tree height and canopy closure," *Canadian Journal of Remote Sensing*, vol. 29, no. 5, pp. 623–632, 2003.
- [33] J. Liu, A. K. Skidmore, S. Jones, T. Wang, M. Heurich, X. Zhu, and Y. Shi, "Large off-nadir scan angle of airborne lidar can severely affect the estimates of forest structure metrics," *ISPRS Journal of Photogrammetry and Remote Sensing*, vol. 136, pp. 13 – 25, 2018.
- [34] E. Næsset, "Predicting forest stand characteristics with airborne scanning laser using a practical two-stage procedure and field data," *Remote Sensing of Environment*, vol. 80, no. 1, pp. 88 – 99, 2002.
- [35] N. C. Coops, T. Hilker, M. A. Wulder, B. St-Onge, G. Newnham, A. Siggins, and J. A. T. Trofymow, "Estimating canopy structure of douglas-fir forest stands from discrete-return lidar," *Trees*, vol. 21, no. 3, p. 295, Jan 2007.
- [36] L. T. Ene, E. Næsset, T. Gobakken, E. W. Mauya, O. M. Bollandsås, T. G. Gregoire, G. Ståhl, and E. Zahabu, "Large-scale estimation of aboveground biomass in miombo woodlands using airborne laser scanning and national forest inventory data," *Remote Sensing of Environment*, vol. 186, pp. 626 – 636,

- 2016.
- [37] D.-A. Kwak, W.-K. Lee, J.-H. Lee, G. S. Biging, and P. Gong, "Detection of individual trees and estimation of tree height using lidar data," *Journal of Forest Research*, vol. 12, no. 6, pp. 425–434, 2007.
- [38] M. Dalponte, H. O. Ørka, L. T. Ene, T. Gobakken, and E. Næsset, "Tree crown delineation and tree species classification in boreal forests using hyperspectral and als data," *Remote Sensing of Environment*, vol. 140, pp. 306 – 317, 2014.
- [39] G. Matasci, N. C. Coops, D. A. R. Williams, and N. Page, "Mapping tree canopies in urban environments using airborne laser scanning (als): a vancouver case study," *Forest Ecosystems*, vol. 5, no. 1, p. 31, Aug 2018.
- [40] T. Hinterhofer, M. Pfennigbauer, A. Ullrich, D. Rothbacher, S. Schraml, and M. Hofstätter, "Uav-based lidar and gamma probe with real-time data processing and downlink for survey of nuclear disaster locations," pp. 10 629 – 10 629 – 10, 2018.
- [41] L. Wallace, A. Lucieer, and C. S. Watson, "Evaluating tree detection and segmentation routines on very high resolution uav lidar data," *IEEE Transactions on Geoscience and Remote Sensing*, vol. 52, no. 12, pp. 7619–7628, Dec 2014.
- [42] B. Brede, A. Lau, H. M. Bartholomeus, and L. Kooistra, "Comparing riegli ricopeter uav lidar derived canopy height and dbh with terrestrial lidar," *Sensors*, vol. 17, no. 10, 2017.
- [43] W. Abdalati, H. J. Zwally, R. Bindshadler, B. Csatho, S. L. Farrell, H. A. Fricker, D. Harding, R. Kwok, M. Lefsky, T. Markus, A. Marshak, T. Neumann, S. Palm, B. Schutz, B. Smith, J. Spinhirne, and C. Webb, "The icesat-2 laser altimetry mission," *Proceedings of the IEEE*, vol. 98, no. 5, pp. 735–751, May 2010.
- [44] J. E. Kay, L. Bourdages, N. B. Miller, A. Morrison, V. Yettella, H. Chepfer, and B. Eaton, "Evaluating and improving cloud phase in the community atmosphere model version 5 using spaceborne lidar observations," *Journal of Geophysical Research: Atmospheres*, vol. 121, no. 8, pp. 4162–4176, 2016.
- [45] J. Boudreau, R. F. Nelson, H. A. Margolis, A. Beaudoin, L. Guindon, and D. S. Kimes, "Regional above-ground forest biomass using airborne and spaceborne lidar in québec," *Remote Sensing of Environment*, vol. 112, no. 10, pp. 3876 – 3890, 2008.
- [46] M. Simard, N. Pinto, J. B. Fisher, and A. Baccini, "Mapping forest canopy height globally with spaceborne lidar," *Journal of Geophysical Research: Biogeosciences*, vol. 116, no. G4, 2011.
- [47] P. J. Besl and H. D. McKay, "A method for registration of 3-d shapes," *IEEE Transactions on Pattern Analysis and Machine Intelligence*, vol. 14, no. 2, pp. 239–256, Feb 1992.
- [48] D. F. Huber and M. Hebert, "3d modeling using a statistical sensor model and stochastic search," in *2003 IEEE Computer Society Conference on Computer Vision and Pattern Recognition, 2003. Proceedings.*, vol. 1, June 2003, pp. I–858–I–865 vol.1.
- [49] A. Myronenko and X. Song, "Point set registration: Coherent point drift," *IEEE Transactions on Pattern Analysis and Machine Intelligence*, vol. 32, no. 12, pp. 2262–2275, Dec 2010.
- [50] B. Douillard, A. Quadros, P. Morton, J. P. Underwood, M. D. Deuge, S. Hugosson, M. Hallström, and T. Bailey, "Scan segments matching for pairwise 3d alignment," in *2012 IEEE International Conference on Robotics and Automation*, May 2012, pp. 3033–3040.
- [51] G. C. Sharp, S. W. Lee, and D. K. Wehe, "Icp registration using invariant features," *IEEE Transactions on Pattern Analysis and Machine Intelligence*, vol. 24, no. 1, pp. 90–102, Jan 2002.
- [52] J. Ho, A. Peter, A. Rangarajan, and M. H. Yang, "An algebraic approach to affine registration of point sets," in *2009 IEEE 12th International Conference on Computer Vision*, Sept 2009, pp. 1335–1340.
- [53] A. Persson, J. Holmgren, and U. Söderman, "Detecting and measuring individual trees using an airborne laser scanner," *Photogrammetric Engineering and Remote Sensing*, vol. 68, no. 9, pp. 925–932, 2002.
- [54] L. Duncanson, B. Cook, G. Hurtt, and R. Dubayah, "An efficient, multi-layered crown delineation algorithm for mapping individual tree structure across multiple ecosystems," *Remote Sensing of Environment*, vol. 154, pp. 378 – 386, 2014.
- [55] A. Ferraz, F. Bretar, S. Jacquemoud, G. Gonçalves, L. Pereira, M. Tomé, and P. Soares, "3-d mapping of a multi-layered mediterranean forest using {ALS} data," *Remote Sensing of Environment*, vol. 121, pp. 210

- 223, 2012.
- [56] C. Paris, D. Valduga, and L. Bruzzone, “A hierarchical approach to three-dimensional segmentation of lidar data at single-tree level in a multilayered forest,” *IEEE Transactions on Geoscience and Remote Sensing*, vol. 54, no. 7, pp. 4190–4203, July 2016.
- [57] V. Meyer, S. S. Saatchi, J. Chave, J. W. Dalling, S. Bohlman, G. A. Fricker, C. Robinson, M. Neumann, and S. Hubbell, “Detecting tropical forest biomass dynamics from repeated airborne lidar measurements,” *Biogeosciences*, vol. 10, no. 8, pp. 5421–5438, 2013.
- [58] O. M. Bollandsås, T. G. Gregoire, E. Næsset, and B.-H. Øyen, “Detection of biomass change in a Norwegian mountain forest area using small footprint airborne laser scanner data,” *Statistical Methods & Applications*, vol. 22, no. 1, pp. 113–129, Mar 2013.
- [59] E. Næsset, O. M. Bollandsås, T. Gobakken, T. G. Gregoire, and G. Ståhl, “Model-assisted estimation of change in forest biomass over an 11 year period in a sample survey supported by airborne lidar: A case study with post-stratification to provide “activity data,”” *Remote Sensing of Environment*, vol. 128, pp. 299 – 314, 2013.
- [60] R. Økseter, O. M. Bollandsås, T. Gobakken, and E. Næsset, “Modeling and predicting aboveground biomass change in young forest using multi-temporal airborne laser scanner data,” *Scandinavian Journal of Forest Research*, vol. 30, no. 5, pp. 458–469, 2015.
- [61] H.-E. Andersen, S. E. Reutebuch, R. J. McGaughey, M. V. d’Oliveira, and M. Keller, “Monitoring selective logging in western amazonia with repeat lidar flights,” *Remote Sensing of Environment*, vol. 151, pp. 157–165, 2014.
- [62] M. Réjou-Méchain, B. Tymen, L. Blanc, S. Fauset, T. R. Feldpausch, A. Monteagudo, O. L. Phillips, H. Richard, and J. Chave, “Using repeated small-footprint lidar acquisitions to infer spatial and temporal variations of a high-biomass neotropical forest,” *Remote Sensing of Environment*, vol. 169, pp. 93–101, 2015.
- [63] W. Huang, G. Sun, R. Dubayah, B. Cook, P. Montesano, W. Ni, and Z. Zhang, “Mapping biomass change after forest disturbance: Applying lidar footprint-derived models at key map scales,” *Remote Sensing of Environment*, vol. 134, pp. 319 – 332, 2013.
- [64] R. E. McRoberts, E. Næsset, T. Gobakken, and O. M. Bollandsås, “Indirect and direct estimation of forest biomass change using forest inventory and airborne laser scanning data,” *Remote Sensing of Environment*, vol. 164, pp. 36 – 42, 2015.
- [65] O. M. Bollandsås, L. T. Ene, T. Gobakken, and E. Næsset, “Estimation of biomass change in montane forests in Norway along a 1200 km latitudinal gradient using airborne laser scanning: a comparison of direct and indirect prediction of change under a model-based inferential approach,” *Scandinavian Journal of Forest Research*, vol. 33, no. 2, pp. 155–165, 2018.
- [66] S. Solberg, E. Næsset, K. H. Hanssen, and E. Christiansen, “Mapping defoliation during a severe insect attack on scots pine using airborne laser scanning,” *Remote Sensing of Environment*, vol. 102, no. 3–4, pp. 364 – 376, 2006.
- [67] E. Næsset and T. Gobakken, “Estimating forest growth using canopy metrics derived from airborne laser scanner data,” *Remote Sensing of Environment*, vol. 96, no. 3, pp. 453 – 465, 2005.
- [68] C. Hopkinson, L. Chasmer, and R. Hall, “The uncertainty in conifer plantation growth prediction from multi-temporal lidar datasets,” *Remote Sensing of Environment*, vol. 112, no. 3, pp. 1168 – 1180, 2008.
- [69] J. Socha, M. Pierzchalski, R. Bałazy, and M. Ciesielski, “Modelling top height growth and site index using repeated laser scanning data,” *Forest Ecology and Management*, vol. 406, pp. 307 – 317, 2017.
- [70] L. Noordermeer, O. M. Bollandsås, T. Gobakken, and E. Næsset, “Direct and indirect site index determination for Norway spruce and Scots pine using bitemporal airborne laser scanner data,” *Forest Ecology and Management*, vol. 428, pp. 104 – 114, 2018.
- [71] B. St-Onge and U. Vepakomma, “Assessing forest gap dynamics and growth using multi-temporal laser-scanner data,” *Power*, vol. 140, p. 200uJ, 2004.
- [72] U. Vepakomma, B. St-Onge, and D. Kneeshaw, “Spatially explicit characterization of boreal forest gap dynamics using multi-temporal lidar data,” *Remote Sensing of Environment*, vol. 112, no. 5, pp. 2326–2340, 2008.

- [73] U. Vepakomma, D. Kneeshaw, and B. St-Onge, "Interactions of multiple disturbances in shaping boreal forest dynamics: a spatially explicit analysis using multi-temporal lidar data and high-resolution imagery," *Journal of Ecology*, vol. 98, no. 3, pp. 526–539, 2010.
- [74] X. Yu, J. Hyypä, H. Kaartinen, and M. Maltamo, "Automatic detection of harvested trees and determination of forest growth using airborne laser scanning," *Remote Sensing of Environment*, vol. 90, no. 4, pp. 451–462, 2004.
- [75] M. Vastaranta, I. Korpela, A. Uotila, A. Hovi, and M. Holopainen, "Mapping of snow-damaged trees based on bitemporal airborne lidar data," *European Journal of Forest Research*, vol. 131, no. 4, pp. 1217–1228, 2012.
- [76] X. Yu, J. Hyypä, H. Kaartinen, H. Hyypä, M. Maltamo, and P. Rönholm, "Measuring the growth of individual trees using multi-temporal airborne laser scanning point clouds," in *Proceedings of ISPRS Workshop Laser Scanning*, vol. 2005. Citeseer, 2005, pp. 204–208.
- [77] X. Yu, J. Hyypä, A. Kukko, M. Maltamo, and H. Kaartinen, "Change detection techniques for canopy height growth measurements using airborne laser scanner data," *Photogrammetric Engineering & Remote Sensing*, vol. 72, no. 12, pp. 1339–1348, 2006.
- [78] U. Vepakomma, B. St-Onge, and D. Kneeshaw, "Response of a boreal forest to canopy opening: assessing vertical and lateral tree growth with multi-temporal lidar data," *Ecological Applications*, vol. 21, no. 1, pp. 99–121, 2011.
- [79] S. Srinivasan, S. C. Popescu, M. Eriksson, R. D. Sheridan, and N.-W. Ku, "Multi-temporal terrestrial laser scanning for modeling tree biomass change," *Forest Ecology and Management*, vol. 318, pp. 304–317, 2014.
- [80] W. Xiao, S. Xu, S. O. Elberink, and G. Vosselman, "Individual tree crown modeling and change detection from airborne lidar data," *IEEE Journal of Selected Topics in Applied Earth Observations and Remote Sensing*, vol. 9, no. 8, pp. 3467–3477, Aug 2016.
- [81] J. P. Skovsgaard and J. K. Vanclay, "Forest site productivity: a review of the evolution of dendrometric concepts for even-aged stands," *Forestry: An International Journal of Forest Research*, vol. 81, no. 1, pp. 13–31, 10 2007.
- [82] J.-D. Bontemps and O. Bouriaud, "Predictive approaches to forest site productivity: recent trends, challenges and future perspectives," *Forestry: An International Journal of Forest Research*, vol. 87, no. 1, pp. 109–128, 11 2013.
- [83] L. T. Ene, E. Næsset, T. Gobakken, O. M. Bollandsås, E. W. Mauya, and E. Zahabu, "Large-scale estimation of change in aboveground biomass in miombo woodlands using airborne laser scanning and national forest inventory data," *Remote Sensing of Environment*, vol. 188, pp. 106–117, 2017.
- [84] R. A. Schowengerdt, *Remote sensing: models and methods for image processing*. Elsevier, 2006.
- [85] G. Camps-Valls and L. Bruzzone, "Kernel-based methods for hyperspectral image classification," *IEEE Transactions on Geoscience and Remote Sensing*, vol. 43, no. 6, pp. 1351–1362, June 2005.
- [86] M. Dalponte, L. Bruzzone, and D. Gianelle, "Fusion of hyperspectral and lidar remote sensing data for classification of complex forest areas," *IEEE Transactions on Geoscience and Remote Sensing*, vol. 46, no. 5, pp. 1416–1427, May 2008.
- [87] M. Fauvel, J. A. Benediktsson, J. Chanussot, and J. R. Sveinsson, "Spectral and spatial classification of hyperspectral data using svms and morphological profiles," *IEEE Transactions on Geoscience and Remote Sensing*, vol. 46, no. 11, pp. 3804–3814, Nov 2008.
- [88] Y. Chen, X. Zhao, and X. Jia, "Spectral–spatial classification of hyperspectral data based on deep belief network," *IEEE Journal of Selected Topics in Applied Earth Observations and Remote Sensing*, vol. 8, no. 6, pp. 2381–2392, June 2015.
- [89] Y. Chen, H. Jiang, C. Li, X. Jia, and P. Ghamisi, "Deep feature extraction and classification of hyperspectral images based on convolutional neural networks," *IEEE Transactions on Geoscience and Remote Sensing*, vol. 54, no. 10, pp. 6232–6251, Oct 2016.
- [90] J. Yue, W. Zhao, S. Mao, and H. Liu, "Spectral–spatial classification of hyperspectral images using deep convolutional neural networks," *Remote Sensing Letters*, vol. 6, no. 6, pp. 468–477, 2015.

- [91] T. Cocks, R. Jenssen, A. Stewart, I. Wilson, and T. Shields, "The hymaptm airborne hyperspectral sensor: The system, calibration and performance," in *Proceedings of the 1st EARSeL workshop on Imaging Spectroscopy*. EARSeL, 1998, pp. 37–42.
- [92] R. O. Green, M. L. Eastwood, C. M. Sarture, T. G. Chrien, M. Aronsson, B. J. Chippendale, J. A. Faust, B. E. Pavri, C. J. Chovit, M. Solis, M. R. Olah, and O. Williams, "Imaging spectroscopy and the airborne visible/infrared imaging spectrometer (aviris)," *Remote Sensing of Environment*, vol. 65, no. 3, pp. 227 – 248, 1998.
- [93] M. A. Cutter, D. R. Lobb, and R. A. Cockshott, "Compact high resolution imaging spectrometer (chris)," *Acta Astronautica*, vol. 46, no. 2, pp. 263 – 268, 2000, 2nd IAA International Symposium on Small Satellites for Earth Observation.
- [94] X. Gu and X. Tong, "Overview of china earth observation satellite programs [space agencies]," *IEEE Geoscience and Remote Sensing Magazine*, vol. 3, no. 3, pp. 113–129, Sept 2015.
- [95] A. Kumar, A. Saha, and V. K. Dadhwal, "Some issues related with sub-pixel classification using hysi data from ims-1 satellite," *Journal of the Indian Society of Remote Sensing*, vol. 38, no. 2, pp. 203–210, Jun 2010.
- [96] L. Candela, R. Formaro, R. Guarini, R. Loizzo, F. Longo, and G. Varacalli, "The prisma mission," in *2016 IEEE International Geoscience and Remote Sensing Symposium (IGARSS)*, July 2016, pp. 253–256.
- [97] T. Matsunaga, A. Iwasaki, S. Tsuchida, K. Iwao, J. Tanii, O. Kashimura, R. Nakamura, H. Yamamoto, S. Kato, K. Obata, K. Mouri, and T. Tachikawa, "Current status of hyperspectral imager suite (hisui) onboard international space station (iss)," in *2017 IEEE International Geoscience and Remote Sensing Symposium (IGARSS)*, July 2017, pp. 443–446.
- [98] L. Guanter, H. Kaufmann, K. Segl, S. Foerster, C. Rogass, S. Chabrillat, T. Kuester, A. Hollstein, G. Rossner, C. Chlebek, C. Straif, S. Fischer, S. Schrader, T. Storch, U. Heiden, A. Mueller, M. Bachmann, H. Mühle, R. Müller, M. Habermeyer, A. Ohndorf, J. Hill, H. Buddenbaum, P. Hostert, S. van der Linden, P. J. Leitão, A. Rabe, R. Doerffer, H. Krasemann, H. Xi, W. Mauser, T. Hank, M. Locherer, a. Rast, K. Staenz, and B. Sang, "The enmap spaceborne imaging spectroscopy mission for earth observation," *Remote Sensing*, vol. 7, no. 7, pp. 8830–8857, 2015.
- [99] C. M. Lee, M. L. Cable, S. J. Hook, R. O. Green, S. L. Ustin, D. J. Mandl, and E. M. Middleton, "An introduction to the nasa hyperspectral infrared imager (hypispi) mission and preparatory activities," *Remote Sensing of Environment*, vol. 167, pp. 6 – 19, 2015, special Issue on the Hyperspectral Infrared Imager (HyspIRI).
- [100] T. Feingersh and E. B. Dor, "Shalom a commercial hyperspectral space mission," in *Optical Payloads for Space Missions*. John Wiley & Sons, Ltd, 2015, ch. 11, pp. 247–263.
- [101] J. Transon, R. d'Andrimont, A. Maignard, and P. Defourny, "Survey of hyperspectral earth observation applications from space in the sentinel-2 context," *Remote Sensing*, vol. 10, no. 2, 2018.
- [102] Y. Zhong, X. Wang, Y. Xu, S. Wang, T. Jia, X. Hu, J. Zhao, L. Wei, and L. Zhang, "Mini-uav-borne hyperspectral remote sensing: From observation and processing to applications," *IEEE Geoscience and Remote Sensing Magazine*, vol. 6, no. 4, pp. 46–62, Dec 2018.
- [103] P. Zarco-Tejada, V. González-Dugo, and J. Berni, "Fluorescence, temperature and narrow-band indices acquired from a uav platform for water stress detection using a micro-hyperspectral imager and a thermal camera," *Remote Sensing of Environment*, vol. 117, pp. 322 – 337, 2012, remote Sensing of Urban Environments.
- [104] P. Zarco-Tejada, M. Guillén-Climent, R. Hernández-Clemente, A. Catalina, M. González, and P. Martín, "Estimating leaf carotenoid content in vineyards using high resolution hyperspectral imagery acquired from an unmanned aerial vehicle (uav)," *Agricultural and Forest Meteorology*, vol. 171–172, pp. 281 – 294, 2013.
- [105] E. Honkavaara, H. Saari, J. Kaivosoja, I. Pölonen, T. Hakala, P. Litkey, J. Mäkyne, and L. Pesonen, "Processing and assessment of spectrometric, stereoscopic imagery collected using a lightweight uav spectral camera for precision agriculture," *Remote Sensing*, vol. 5, no. 10, pp. 5006–5039, 2013.
- [106] I. Kalisperakis, C. Stentoumis, L. Grammatikopoulos, and K. Karantzalos, "Leaf area index estimation in vineyards from uav hyperspectral data, 2d image mosaics and 3d canopy surface models," *The International Archives of Photogrammetry, Remote Sensing and Spatial Information Sciences*, vol. 40, no. 1, p. 299, 2015.

- [107] R. Näsi, E. Honkavaara, P. Lyytikäinen-Saarenmaa, M. Blomqvist, P. Litkey, T. Hakala, N. Viljanen, T. Kantola, T. Tanhuanpää, and M. Holopainen, “Using uav-based photogrammetry and hyperspectral imaging for mapping bark beetle damage at tree-level,” *Remote Sensing*, vol. 7, no. 11, pp. 15 467–15 493, 2015.
- [108] O. Nevalainen, E. Honkavaara, S. Tuominen, N. Viljanen, T. Hakala, X. Yu, J. Hyypä, H. Saari, I. Pölönen, N. N. Imai, and A. M. G. Tommaselli, “Individual tree detection and classification with uav-based photogrammetric point clouds and hyperspectral imaging,” *Remote Sensing*, vol. 9, no. 3, 2017.
- [109] T. Sankey, J. Donager, J. McVay, and J. B. Sankey, “Uav lidar and hyperspectral fusion for forest monitoring in the southwestern usa,” *Remote Sensing of Environment*, vol. 195, pp. 30 – 43, 2017.
- [110] M. M. Marques, V. Lobo, R. Batista, J. Almeida, M. d. F. Nunes, R. Ribeiro, and A. Bernardino, “Oil spills detection: Challenges addressed in the scope of the seagull project,” in *OCEANS 2016 MTS/IEEE Monterey*, Sep. 2016, pp. 1–6.
- [111] S. Freitas, H. Silva, J. Almeida, and E. Silva, “Hyperspectral imaging for real-time unmanned aerial vehicle maritime target detection,” *Journal of Intelligent & Robotic Systems*, vol. 90, no. 3, pp. 551–570, Jun 2018.
- [112] A. Singh, “Review article digital change detection techniques using remotely-sensed data,” *International Journal of Remote Sensing*, vol. 10, no. 6, pp. 989–1003, 1989.
- [113] F. Bovolo, S. Marchesi, and L. Bruzzone, “A framework for automatic and unsupervised detection of multiple changes in multitemporal images,” *IEEE Transactions on Geoscience and Remote Sensing*, vol. 50, no. 6, pp. 2196–2212, June 2012.
- [114] D. Lu, P. Mausel, E. Brondizio, and E. Moran, “Change detection techniques,” *International Journal of Remote Sensing*, vol. 25, no. 12, pp. 2365–2401, 2004.
- [115] P. Du, S. Liu, P. Gamba, and K. Tan, “Fusion of difference images for change detection over urban areas,” *IEEE Journal of Selected Topics in Applied Earth Observations and Remote Sensing*, vol. 5, no. 4, pp. 1076–1086, Aug 2012.
- [116] P. Ghamisi, N. Yokoya, J. Li, W. Liao, S. Liu, J. Plaza, B. Rasti, and A. Plaza, “Advances in hyperspectral image and signal processing: A comprehensive overview of the state of the art,” *IEEE Geoscience and Remote Sensing Magazine*, vol. 5, no. 4, pp. 37–78, Dec 2017.
- [117] L. Bruzzone, S. Liu, F. Bovolo, and P. Du, *Change Detection in Multitemporal Hyperspectral Images*. Cham: Springer International Publishing, 2016, pp. 63–88.
- [118] S. Liu, Q. Du, X. Tong, A. Samat, H. Pan, and X. Ma, “Band selection-based dimensionality reduction for change detection in multi-temporal hyperspectral images,” *Remote Sensing*, vol. 9, no. 10, 2017.
- [119] K. Beyer, J. Goldstein, R. Ramakrishnan, and U. Shaft, “When is “nearest neighbor” meaningful?” in *International conference on database theory*. Springer, 1999, pp. 217–235.
- [120] G. Hughes, “On the mean accuracy of statistical pattern recognizers,” *IEEE Transactions on Information Theory*, vol. 14, no. 1, pp. 55–63, January 1968.
- [121] B.-C. Gao and A. F. H. Goetz, “Column atmospheric water vapor and vegetation liquid water retrievals from airborne imaging spectrometer data,” *Journal of Geophysical Research: Atmospheres*, vol. 95, no. D4, pp. 3549–3564, 1990.
- [122] S. M. Adler-Golden, M. W. Matthew, L. S. Bernstein, R. Y. Levine, A. Berk, S. C. Richtsmeier, P. K. Acharya, G. P. Anderson, J. W. Felde, J. Gardner *et al.*, “Atmospheric correction for shortwave spectral imagery based on modtran4,” pp. 3753 – 3753 – 9, 1999.
- [123] M. Dalponte, L. Bruzzone, L. Vescovo, and D. Gianelle, “The role of spectral resolution and classifier complexity in the analysis of hyperspectral images of forest areas,” *Remote Sensing of Environment*, vol. 113, no. 11, pp. 2345 – 2355, 2009.
- [124] P. Coppin, I. Jonckheere, K. Nackaerts, B. Muys, and E. Lambin, “Digital change detection methods in ecosystem monitoring: a review,” *International Journal of Remote Sensing*, vol. 25, no. 9, pp. 1565–1596, 2004.
- [125] D. Lu, G. Li, and E. Moran, “Current situation and needs of change detection techniques,” *International Journal of Image and Data Fusion*, vol. 5, no. 1, pp. 13–38, 2014.

- [126] Y. Ban and O. Yousif, *Change Detection Techniques: A Review*. Cham: Springer International Publishing, 2016, pp. 19–43.
- [127] M. Hasanlou and S. T. Seydi, “Hyperspectral change detection: an experimental comparative study,” *International Journal of Remote Sensing*, no. 1, pp. 1–55, 2018.
- [128] A. P. Schaum and A. Stocker, “Hyperspectral change detection and supervised matched filtering based on covariance equalization,” *Proceedings of SPIE - The International Society for Optical Engineering*, vol. 5425, pp. 77–90, 2004.
- [129] M. Shimoni, R. Heremans, and C. Perneel, “Detection of small changes in complex urban and industrial scenes using imaging spectroscopy,” in *2010 IEEE International Geoscience and Remote Sensing Symposium*, July 2010, pp. 4757–4760.
- [130] J. Theiler, C. Scovel, B. Wohlberg, and B. R. Foy, “Elliptically contoured distributions for anomalous change detection in hyperspectral imagery,” *IEEE Geoscience and Remote Sensing Letters*, vol. 7, no. 2, pp. 271–275, April 2010.
- [131] C. Wu, L. Zhang, and B. Du, “Hyperspectral anomaly change detection with slow feature analysis,” *Neurocomputing*, vol. 151, pp. 175–187, 2015.
- [132] J. Zhou, C. Kwan, B. Ayhan, and M. T. Eismann, “A novel cluster kernel rx algorithm for anomaly and change detection using hyperspectral images,” *IEEE Transactions on Geoscience and Remote Sensing*, vol. 54, no. 11, pp. 6497–6504, 2016.
- [133] J. Meola, M. T. Eismann, R. L. Moses, and J. N. Ash, “Application of model-based change detection to airborne vnir/swir hyperspectral imagery,” *IEEE Transactions on Geoscience and Remote Sensing*, vol. 50, no. 10, pp. 3693–3706, 2012.
- [134] C. Wu, B. Du, and L. Zhang, “A subspace-based change detection method for hyperspectral images,” *IEEE Journal of Selected Topics in Applied Earth Observations and Remote Sensing*, vol. 6, no. 2, pp. 815–830, 2013.
- [135] N. Acito, M. Diani, G. Corsini, and S. Resta, “Introductory view of anomalous change detection in hyperspectral images within a theoretical gaussian framework,” *IEEE Aerospace and Electronic Systems Magazine*, vol. 32, no. 7, pp. 2–27, 2017.
- [136] K. Vongsy, M. J. Mendenhall, M. T. Eismann, and G. L. Peterson, “Removing parallax-induced changes in hyperspectral change detection,” in *2012 IEEE International Geoscience and Remote Sensing Symposium*, 2012, pp. 2012–2015.
- [137] J. Meola and M. T. Eismann, “Image misregistration effects on hyperspectral change detection,” in *Algorithms and Technologies for Multispectral, Hyperspectral, and Ultraspectral Imagery XIV*, vol. 6966. International Society for Optics and Photonics, 2008, p. 69660Y.
- [138] J. Theiler and B. Wohlberg, “Local coregistration adjustment for anomalous change detection,” *IEEE Transactions on Geoscience and Remote Sensing*, vol. 50, no. 8, pp. 3107–3116, 2012.
- [139] J. Meola, M. T. Eismann, K. J. Barnard, and R. C. Hardie, “Analysis of hyperspectral change detection as affected by vegetation and illumination variations,” in *Defense and Security Symposium*. International Society for Optics and Photonics, 2007, pp. 65 651S–65 651S.
- [140] M. T. Eismann, J. Meola, and R. C. Hardie, “Hyperspectral change detection in the presence of diurnal and seasonal variations,” *IEEE Transactions on Geoscience and Remote Sensing*, vol. 46, no. 1, pp. 237–249, 2008.
- [141] M. Frank and M. Canty, “Unsupervised change detection for hyperspectral images,” in *Proc. AVIRIS workshop*, 2003.
- [142] A. A. Nielsen, “The regularized iteratively reweighted mad method for change detection in multi- and hyperspectral data,” *IEEE Transactions on Image Processing*, vol. 16, no. 2, pp. 463–478, 2007.
- [143] V. Ortiz-Rivera, M. Vélez-Reyes, and B. Roysam, “Change detection in hyperspectral imagery using temporal principal components,” in *SPIE: Algorithms and Technologies for Multispectral, Hyperspectral, and Ultraspectral Imagery Xii*, 2006.
- [144] A. A. Nielsen, “Kernel maximum autocorrelation factor and minimum noise fraction transformations,”

- IEEE Transactions on Image Processing*, vol. 20, no. 3, pp. 612–624, 2011.
- [145] S. Liu, L. Bruzzone, F. Bovolo, and P. Du, “Unsupervised hierarchical spectral analysis for change detection in hyperspectral images,” in *Hyperspectral Image and Signal Processing (WHISPERS), 2012 4th Workshop on*, 2012, pp. 1–4.
- [146] Y. Yuan, H. Lv, and X. Lu, “Semi-supervised change detection method for multi-temporal hyperspectral images,” *Neurocomputing*, vol. 148, pp. 363–375, 2015.
- [147] Q. Du, N. Younan, and R. King, “Change analysis for hyperspectral imagery,” in *Analysis of Multi-temporal Remote Sensing Images, 2007. MultiTemp 2007. International Workshop on the*, 2007, pp. 1–4.
- [148] Z. Chen and B. Wang, “Spectrally-spatially regularized low-rank and sparse decomposition: A novel method for change detection in multitemporal hyperspectral images,” *Remote Sensing*, vol. 9, no. 10, 2017.
- [149] Q. Du, L. Wasson, and R. King, “Unsupervised linear unmixing for change detection in multitemporal airborne hyperspectral imagery,” in *2005 International Workshop on the Analysis of Multi-Temporal Remote Sensing Images*, 2005, pp. 136–140.
- [150] A. Ertürk and A. Plaza, “Informative change detection by unmixing for hyperspectral images,” *IEEE Geoscience and Remote Sensing Letters*, vol. 12, no. 6, pp. 1252–1256, 2015.
- [151] A. Ertürk, M. D. Iordache, and A. Plaza, “Sparse unmixing-based change detection for multitemporal hyperspectral images,” *IEEE Journal of Selected Topics in Applied Earth Observations and Remote Sensing*, vol. 9, no. 2, pp. 708–719, 2015.
- [152] —, “Sparse unmixing with dictionary pruning for hyperspectral change detection,” *IEEE Journal of Selected Topics in Applied Earth Observations and Remote Sensing*, vol. 10, no. 1, pp. 321–330, Jan 2017.
- [153] H. Lyu, H. Lu, and L. Mou, “Learning a transferable change rule from a recurrent neural network for land cover change detection,” *Remote Sensing*, vol. 8, no. 6, 2016.
- [154] Q. Wang, Z. Yuan, Q. Du, and X. Li, “Getnet: A general end-to-end 2-d cnn framework for hyperspectral image change detection,” *IEEE Transactions on Geoscience and Remote Sensing*, vol. 57, no. 1, pp. 3–13, 2019.
- [155] S. Liu, L. Bruzzone, F. Bovolo, and M. Zanetti, “Sequential spectral change vector analysis for iteratively discovering and detecting multiple changes in hyperspectral images,” *IEEE Transactions on Geoscience and Remote Sensing*, vol. 53, no. 8, pp. 4363–4378, 2015.
- [156] S. Liu, X. Tong, L. Bruzzone, and P. Du, “A novel semisupervised framework for multiple change detection in hyperspectral images,” in *2017 IEEE International Geoscience and Remote Sensing Symposium (IGARSS)*, July 2017, pp. 173–176.
- [157] S. Liu, L. Bruzzone, F. Bovolo, and P. Du, “Unsupervised multitemporal spectral unmixing for detecting multiple changes in hyperspectral images,” *IEEE Transactions on Geoscience and Remote Sensing*, vol. 54, no. 5, pp. 2733–2748, May 2016.
- [158] S. Hemissi, I. R. Farah, K. S. Ettabaa, and B. Solaiman, “Multi-spectro-temporal analysis of hyperspectral imagery based on 3-d spectral modeling and multilinear algebra,” *IEEE Transactions on Geoscience and Remote Sensing*, vol. 51, no. 1, pp. 199–216, 2013.
- [159] J. Yang and W. Sun, “Automatic analysis of the slight change image for unsupervised change detection,” *Journal of Applied Remote Sensing*, vol. 9, no. 1, p. 095995, 2015.
- [160] S. Henrot, J. Chanussot, and C. Jutten, “Dynamical spectral unmixing of multitemporal hyperspectral images,” *IEEE Transactions on Image Processing*, vol. 25, no. 9, pp. 4443–4443, 2016.
- [161] M. A. Veganzones, J. E. Cohen, R. C. Farias, J. Chanussot, and P. Comon, “Nonnegative tensor cp decomposition of hyperspectral data,” *IEEE Transactions on Geoscience and Remote Sensing*, vol. 54, no. 5, pp. 2577–2588, 2016.
- [162] M. T. Eismann and J. Meola, “Hyperspectral change detection: Methodology and challenges,” in *IGARSS 2008 - 2008 IEEE International Geoscience and Remote Sensing Symposium*, 2008, pp. II–605–II–608.
- [163] A. Schaum and A. Stocker, “Long-interval chronochrome target detection,” in *Proc. 1997 International Symposium on Spectral Sensing Research*, 1998, pp. 1760–1770.
- [164] K. Vongsy and M. J. Mendenhall, “A comparative study of spectral detectors,” in *2011 3rd Workshop on*

- Hyperspectral Image and Signal Processing: Evolution in Remote Sensing (WHISPERS)*, June 2011, pp. 1–4.
- [165] Y. Du, C. Chang, H. Ren, C. C. Chang, and F. M. D’Amico, “New hyperspectral discrimination measure for spectral characterization,” *Optical Engineering*, vol. 43, no. 8, pp. 1777–1786, 2004.
- [166] L. Bruzzone and D. F. Prieto, “Automatic analysis of the difference image for unsupervised change detection,” *IEEE Transactions on Geoscience and Remote Sensing*, vol. 38, no. 3, pp. 1171–1182, 2000.
- [167] M. Zanetti, F. Bovolo, and L. Bruzzone, “Rayleigh-rice mixture parameter estimation via em algorithm for change detection in multispectral images,” *IEEE Transactions on Image Processing*, vol. 24, no. 12, pp. 5004–16, 2015.
- [168] A. A. Nielsen, K. Conradsen, and J. J. Simpson, “Multivariate alteration detection (mad) and maf post-processing in multispectral, bitemporal image data: New approaches to change detection studies,” *Remote Sensing of Environment*, vol. 64, no. 1, pp. 1–19, 1998.
- [169] S. Hemissi, I. R. Farah, K. S. Ettabaa, and B. Solaiman, “A new spatio-temporal ica for multi-temporal endmembers extraction and change trajectory analysis,” *Piers Marrakesh Progress in Electromagnetics Research Symposium*, pp. 1289–1293, 2011.
- [170] X. X. Zhu, D. Tuia, L. Mou, G. Xia, L. Zhang, F. Xu, and F. Fraundorfer, “Deep learning in remote sensing: A comprehensive review and list of resources,” *IEEE Geoscience and Remote Sensing Magazine*, vol. 5, no. 4, pp. 8–36, Dec 2017.
- [171] B. Jeon and D. A. Landgrebe, “Classification with spatio-temporal interpixel class dependency contexts,” *IEEE Transactions on Geoscience and Remote Sensing*, vol. 30, no. 4, pp. 663–672, Jul 1992.
- [172] X. L. Dal and S. Khorram, “Remotely sensed change detection based on artificial neural networks,” *Photogrammetric Engineering and Remote Sensing*, vol. 65, no. 10, pp. 1187–1194, 1999.
- [173] P. Du, S. Liu, P. Liu, K. Tan, and L. Cheng, “Sub-pixel change detection for urban land-cover analysis via multi-temporal remote sensing images,” *Geospatial Information Science*, vol. 17, no. 1, pp. 26–38, 2014.
- [174] M. Hauglin, J. Dibdiakova, T. Gobakken, and E. Næsset, “Estimating single-tree branch biomass of Norway spruce by airborne laser scanning,” *{ISPRS} Journal of Photogrammetry and Remote Sensing*, vol. 79, pp. 147 – 156, 2013.
- [175] A. Ferraz, S. Saatchi, C. Mallet, and V. Meyer, “Lidar detection of individual tree size in tropical forests,” *Remote Sensing of Environment*, vol. 183, pp. 318 – 333, 2016.
- [176] D. Riaño, E. Chuvieco, S. Condés, J. González-Matesanz, and S. L. Ustin, “Generation of crown bulk density for pinus sylvestris l. from lidar,” *Remote Sensing of Environment*, vol. 92, no. 3, pp. 345 – 352, 2004, forest Fire Prevention and Assessment.
- [177] M. A. Finney, *FARSITE: Fire area simulator: model development and evaluation*. US Department of Agriculture, Forest Service, Rocky Mountain Research Station Ogden, UT, 2004.
- [178] A. Kato, L. M. Moskal, P. Schiess, M. E. Swanson, D. Calhoun, and W. Stuetzle, “Capturing tree crown formation through implicit surface reconstruction using airborne lidar data,” *Remote Sensing of Environment*, vol. 113, no. 6, pp. 1148–1162, 2009.
- [179] C. Stolojescu-Crişan and A. Isar, “Images compressive sensing reconstruction by inpainting,” in *2015 International Symposium on Signals, Circuits and Systems (ISSCS)*, July 2015, pp. 1–4.
- [180] J. Hyypä, O. Kelle, M. Lehikoinen, and M. Inkinen, “A segmentation-based method to retrieve stem volume estimates from 3-d tree height models produced by laser scanners,” *IEEE Transactions on Geoscience and Remote Sensing*, vol. 39, no. 5, pp. 969–975, May 2001.
- [181] F. Morsdorf, E. Meier, B. Kötz, K. I. Itten, M. Dobbertin, and B. Allgöwer, “Lidar-based geometric reconstruction of boreal type forest stands at single tree level for forest and wildland fire management,” *Remote Sensing of Environment*, vol. 92, no. 3, pp. 353–362, 2004.
- [182] Y. Sheng, P. Gong, and G. Biging, “Model-based conifer-crown surface reconstruction from high-resolution aerial images,” *Photogrammetric engineering and remote sensing*, vol. 67, no. 8, pp. 957–966, 2001.
- [183] C. Paris and L. Bruzzone, “A three-dimensional model-based approach to the estimation of the tree top height by fusing low-density lidar data and very high resolution optical images,” *Geoscience and Remote*

- Sensing, IEEE Transactions on*, vol. 53, no. 1, pp. 467–480, Jan 2015.
- [184] H. T. Valentine, R. L. Amateis, J. H. Gove, and A. Mäkelä, “Crown-rise and crown-length dynamics: application to loblolly pine,” *Forestry: An International Journal of Forest Research*, vol. 86, no. 3, p. 371, 2013.
- [185] L. Bruzzone and S. Serpico, “Detection of changes in remotely-sensed images by the selective use of multi-spectral information,” *International Journal of Remote Sensing*, vol. 18, no. 18, pp. 3883–3888, 1997.
- [186] L. Bruzzone and D. F. Prieto, “A minimum-cost thresholding technique for unsupervised change detection,” *International Journal of Remote Sensing*, vol. 21, no. 18, pp. 3539–3544, 2000.
- [187] T. Celik, “Change detection in satellite images using a genetic algorithm approach,” *IEEE Geoscience and Remote Sensing Letters*, vol. 7, no. 2, pp. 386–390, April 2010.
- [188] A. Ghosh, N. S. Mishra, and S. Ghosh, “Fuzzy clustering algorithms for unsupervised change detection in remote sensing images,” *Information Sciences*, vol. 181, no. 4, pp. 699 – 715, 2011.
- [189] P. Du, S. Liu, J. Xia, and Y. Zhao, “Information fusion techniques for change detection from multi-temporal remote sensing images,” *Information Fusion*, vol. 14, no. 1, pp. 19 – 27, 2013.
- [190] S. Ghosh, L. Bruzzone, S. Patra, F. Bovolo, and A. Ghosh, “A context-sensitive technique for unsupervised change detection based on hopfield-type neural networks,” *IEEE Transactions on Geoscience and Remote Sensing*, vol. 45, no. 3, pp. 778–789, March 2007.
- [191] S. Ghosh, S. Patra, and A. Ghosh, “An unsupervised context-sensitive change detection technique based on modified self-organizing feature map neural network,” *International Journal of Approximate Reasoning*, vol. 50, no. 1, pp. 37 – 50, 2009, special Section on Recent advances in soft computing in image processing and Special Section on Selected papers from NAFIPS 2006.
- [192] A. Ghosh, B. N. Subudhi, and L. Bruzzone, “Integration of gibbs markov random field and hopfield-type neural networks for unsupervised change detection in remotely sensed multitemporal images,” *IEEE Transactions on Image Processing*, vol. 22, no. 8, pp. 3087–3096, Aug 2013.
- [193] H. Liu and Q. Zhou, “Accuracy analysis of remote sensing change detection by rule-based rationality evaluation with post-classification comparison,” *International Journal of Remote Sensing*, vol. 25, no. 5, pp. 1037–1050, 2004.
- [194] F. Pacifici, F. D. Frate, C. Solimini, and W. J. Emery, “An innovative neural-net method to detect temporal changes in high-resolution optical satellite imagery,” *IEEE Transactions on Geoscience and Remote Sensing*, vol. 45, no. 9, pp. 2940–2952, Sept 2007.
- [195] H. Alphan, H. Doygun, and Y. I. Unlukaplan, “Post-classification comparison of land cover using multi-temporal landsat and aster imagery: the case of kahramanmaraş, turkey,” *Environmental Monitoring and Assessment*, vol. 151, no. 1, pp. 327–336, Apr 2009.
- [196] M. Volpi, D. Tuia, F. Bovolo, M. Kanevski, and L. Bruzzone, “Supervised change detection in vhr images using contextual information and support vector machines,” *International Journal of Applied Earth Observation and Geoinformation*, vol. 20, pp. 77 – 85, 2013, earth Observation and Geoinformation for Environmental Monitoring.
- [197] L. Bruzzone and S. B. Serpico, “An iterative technique for the detection of land-cover transitions in multitemporal remote-sensing images,” *IEEE Transactions on Geoscience and Remote Sensing*, vol. 35, no. 4, pp. 858–867, Jul 1997.
- [198] L. Bruzzone, D. F. Prieto, and S. B. Serpico, “A neural-statistical approach to multitemporal and multi-source remote-sensing image classification,” *IEEE Transactions on Geoscience and remote Sensing*, vol. 37, no. 3, pp. 1350–1359, 1999.
- [199] B. Demir, F. Bovolo, and L. Bruzzone, “Detection of land-cover transitions in multitemporal remote sensing images with active-learning-based compound classification,” *IEEE Transactions on Geoscience and Remote Sensing*, vol. 50, no. 5, pp. 1930–1941, 2012.
- [200] J. Zhong and R. Wang, “Multi-temporal remote sensing change detection based on independent component analysis,” *International Journal of Remote Sensing*, vol. 27, no. 10, pp. 2055–2061, 2006.
- [201] Z. I. Botev, J. F. Grotowski, and D. P. Kroese, “Kernel density estimation via diffusion,” *Ann. Statist.*,

- vol. 38, no. 5, pp. 2916–2957, 10 2010.
- [202] F. Bovolo and L. Bruzzone, “A theoretical framework for unsupervised change detection based on change vector analysis in the polar domain,” *IEEE Transactions on Geoscience and Remote Sensing*, vol. 45, no. 1, pp. 218–236, Jan 2007.
- [203] —, “An adaptive thresholding approach to multiple-change detection in multispectral images,” in *2011 IEEE International Geoscience and Remote Sensing Symposium*, July 2011, pp. 233–236.
- [204] Z. Bar-Joseph, D. K. Gifford, and T. S. Jaakkola, “Fast optimal leaf ordering for hierarchical clustering,” *Bioinformatics*, vol. 17, no. suppl 1, pp. S22–S29, 2001.
- [205] C.-I. Chang, Q. Du, T.-L. Sun, and M. L. G. Althouse, “A joint band prioritization and band-decorrelation approach to band selection for hyperspectral image classification,” *IEEE Transactions on Geoscience and Remote Sensing*, vol. 37, no. 6, pp. 2631–2641, Nov 1999.
- [206] A. Martínez-Usó, F. Pla, J. M. Sotoca, and P. García-Sevilla, “Clustering-based hyperspectral band selection using information measures,” *IEEE Transactions on Geoscience and Remote Sensing*, vol. 45, no. 12, pp. 4158–4171, Dec 2007.
- [207] Q. Wang, J. Lin, and Y. Yuan, “Salient band selection for hyperspectral image classification via manifold ranking,” *IEEE Transactions on Neural Networks and Learning Systems*, vol. 27, no. 6, pp. 1279–1289, June 2016.
- [208] Q. Wang, F. Zhang, and X. Li, “Optimal clustering framework for hyperspectral band selection,” *IEEE Transactions on Geoscience and Remote Sensing*, vol. 56, no. 10, pp. 5910–5922, Oct 2018.
- [209] A. Chakrabarti and T. Zickler, “Statistics of Real-World Hyperspectral Images,” in *Proc. IEEE Conf. on Computer Vision and Pattern Recognition (CVPR)*, 2011, pp. 193–200.
- [210] G. W. Felde, G. P. Anderson, T. W. Cooley, M. W. Matthew, S. M. adler Golden, A. Berk, and J. Lee, “Analysis of hyperion data with the flaash atmospheric correction algorithm,” in *IGARSS 2003. 2003 IEEE International Geoscience and Remote Sensing Symposium. Proceedings*, vol. 1, July 2003, pp. 90–92 vol.1.
- [211] R. Beck, “Eo-1 user guide v. 2.3,” 2003.
- [212] B. Datt, T. R. McVicar, T. G. V. Niel, D. L. B. Jupp, and J. S. Pearlman, “Preprocessing eo-1 hyperion hyperspectral data to support the application of agricultural indexes,” *IEEE Transactions on Geoscience and Remote Sensing*, vol. 41, no. 6, pp. 1246–1259, June 2003.
- [213] T. Brandtberg, T. A. Warner, R. E. Landenberger, and J. B. McGraw, “Detection and analysis of individual leaf-off tree crowns in small footprint, high sampling density lidar data from the eastern deciduous forest in north america,” *Remote Sensing of Environment*, vol. 85, no. 3, pp. 290 – 303, 2003.
- [214] M. J. Falkowski, A. M. Smith, A. T. Hudak, P. E. Gessler, L. A. Vierling, and N. L. Crookston, “Automated estimation of individual conifer tree height and crown diameter via two-dimensional spatial wavelet analysis of lidar data,” *Canadian Journal of Remote Sensing*, vol. 32, no. 2, pp. 153–161, 2006.
- [215] J. Secord and A. Zakhor, “Tree detection in urban regions using aerial lidar and image data,” *IEEE Geoscience and Remote Sensing Letters*, vol. 4, no. 2, pp. 196–200, April 2007.
- [216] J. Reitberger, M. Heurich, P. Krzystek, and U. Stilla, “Single tree detection in forest areas with high-density lidar data,” *International Archives of Photogrammetry, Remote Sensing and Spatial Information Sciences*, vol. 36, no. 3, pp. 139–144, 2007.
- [217] S. Gupta, H. Weinacker, and B. Koch, “Comparative analysis of clustering-based approaches for 3-d single tree detection using airborne fullwave lidar data,” *Remote Sensing*, vol. 2, no. 4, pp. 968–989, 2010.
- [218] J. C. Suárez, C. Ontiveros, S. Smith, and S. Snape, “Use of airborne lidar and aerial photography in the estimation of individual tree heights in forestry,” *Computers & Geosciences*, vol. 31, no. 2, pp. 253 – 262, 2005.
- [219] S. C. Popescu and K. Zhao, “A voxel-based lidar method for estimating crown base height for deciduous and pine trees,” *Remote Sensing of Environment*, vol. 112, no. 3, pp. 767 – 781, 2008.
- [220] P. Gong, Y. Sheng, and G. Biging, “3d model-based tree measurement from high-resolution aerial imagery,” *Photogrammetric Engineering and Remote Sensing*, vol. 68, no. 11, pp. 1203–1212, 2002.
- [221] H. Weinacker, B. Koch, U. Heyder, and R. Weinacker, “Development of filtering, segmentation and mod-

- elling modules for lidar and multispectral data as a fundament of an automatic forest inventory system,” in *Int. Archives of Photogrammetry and Remote Sensing*, 2004, pp. 1682–1750.
- [222] J.-F. Côté, J.-L. Widlowski, R. A. Fournier, and M. M. Verstraete, “The structural and radiative consistency of three-dimensional tree reconstructions from terrestrial lidar,” *Remote Sensing of Environment*, vol. 113, no. 5, pp. 1067 – 1081, 2009.
- [223] J. Vauhkonen, “Estimating crown base height for scots pine by means of the 3d geometry of airborne laser scanning data,” *International Journal of Remote Sensing*, vol. 31, no. 5, pp. 1213–1226, 2010.
- [224] J. Vauhkonen, I. Korpela, M. Maltamo, and T. Tokola, “Imputation of single-tree attributes using airborne laser scanning-based height, intensity, and alpha shape metrics,” *Remote Sensing of Environment*, vol. 114, no. 6, pp. 1263 – 1276, 2010.
- [225] M. Rutzinger, A. K. Pratihast, S. Oude Elberink, and G. Vosselman, “Detection and modelling of 3d trees from mobile laser scanning data,” *Int. Arch. Photogramm. Remote Sens. Spat. Inf. Sci.*, vol. 38, pp. 520–525, 2010.
- [226] L. Cao, N. C. Coops, J. L. Innes, S. R. Sheppard, L. Fu, H. Ruan, and G. She, “Estimation of forest biomass dynamics in subtropical forests using multi-temporal airborne lidar data,” *Remote Sensing of Environment*, vol. 178, pp. 158 – 171, 2016.
- [227] K. Zhao, J. C. Suarez, M. Garcia, T. Hu, C. Wang, and A. Londo, “Utility of multitemporal lidar for forest and carbon monitoring: Tree growth, biomass dynamics, and carbon flux,” *Remote Sensing of Environment*, vol. 204, pp. 883 – 897, 2018.
- [228] M. Dalponte, L. Bruzzone, and D. Gianelle, “Tree species classification in the southern alps based on the fusion of very high geometrical resolution multispectral/hyperspectral images and lidar data,” *Remote Sensing of Environment*, vol. 123, pp. 258 – 270, 2012.